



HAL
open science

Flow-acoustic interaction with innovative materials

Massimo Emiliano d'Elia

► **To cite this version:**

Massimo Emiliano d'Elia. Flow-acoustic interaction with innovative materials. Acoustics [physics.class-ph]. Le Mans Université, 2021. English. NNT: 2021LEMA1040 . tel-03588310

HAL Id: tel-03588310

<https://theses.hal.science/tel-03588310>

Submitted on 24 Feb 2022

HAL is a multi-disciplinary open access archive for the deposit and dissemination of scientific research documents, whether they are published or not. The documents may come from teaching and research institutions in France or abroad, or from public or private research centers.

L'archive ouverte pluridisciplinaire **HAL**, est destinée au dépôt et à la diffusion de documents scientifiques de niveau recherche, publiés ou non, émanant des établissements d'enseignement et de recherche français ou étrangers, des laboratoires publics ou privés.

THESE DE DOCTORAT

LE MANS UNIVERSITE

COMUE UNIVERSITE BRETAGNE LOIRE

ECOLE DOCTORALE N° 602

Sciences pour l'Ingénieur

Discipline : 60

Spécialité : Aéroacoustique

Massimo Emiliano D'ELIA

Flow-Acoustic Interaction with Innovative Materials

Thèse présentée et soutenue au Mans le 16 Décembre 2021

Unité de recherche : Laboratoire d'Acoustique de l'Université du Mans (LAUM, UMR CNRS 6613)

Thèse n° : 2021LEMA1040

Président :	Gwénaél GABARD	Professeur des Universités (LAUM) - Le Mans
Rapporteurs :	Estelle PIOT	Maître de Recherche (ONERA) - Toulouse
	Jean-Christophe VALIÈRE	Professeur des Universités (Institut PPRIME) - Poitiers
Examineurs :	Thomas HUMBERT	Ingénieur de Recherche (LAUM) - Le Mans
	Christophe SCHRAM	Professeur des Universités (von Karman Institute) - Bruxelles
Dir. de thèse :	Yves AURÉGAN	Directeur de Recherche (CNRS) - Le Mans

Titre : Interaction Aéro-Acoustique avec des Matériaux Innovants

Mots-clés : Aéroacoustique des Conduits, Plaque Corrugée, Poutres Vibrants, Métamatériaux, Sifflement

Résumé : Ces travaux de thèse portent sur le comportement aéroacoustique de nouveaux métamatériaux subjugués à un écoulement cisailé pour comprendre son effet sur la réponse acoustique. Trois matériaux ont été considérés dans cette thèse : d'abord, l'investigation d'une plaque corruguée en présence/absence d'écoulement cisailé est présentée. Dans la littérature, corrugations similaires ont montrés intéressants effets d'amplification/affaiblissement à des précis nombres de Strouhal liés à la largeur de la cavité (et la nature de son bord), à la vitesse de l'écoulement et la fréquence acoustique. Un système de mesure acoustique et optique a été mis en place pour investiguer le régime linéaire de ces perturbations. Finalement, les quatre composantes qui produisent la puissance acoustique et leur importance relative ont été caractérisés ainsi comme le mécanisme de production/absorption. La deuxième partie de cette travail est axée sur un autre aspect d'effet d'écoulement. Puisque nouveaux métamatériaux sont investigués, très souvent on prend en compte une couche qui pourrait bloquer les interactions avec l'écoulement mais qui pourrait laisser passer les ondes acoustiques. Autant souvent, cette couche est pensée fabriquée en Kevlar, en vue de son utilisation dans les souffleries aéroacoustiques. L'interêt de cette partie était donc de montrer comme la présence d'une couche de Kevlar peut éliminer les interactions mais, en même temps, elle limite aussi effets de résonance intéressants et donc ne peut pas être considérée 'transparente'. Ensuite, dans la troisième partie de cette thèse, l'investigation d'une nouvelle conception de liner basé sur une poutre en porte-à-faux est présentée. Cette poutre est composée par des plaques articulées et des fentes, qui permettent d'améliorer leurs prestations à baisse fréquences, surtout si comparées avec celles d'autre métamatériaux 'vibrantes' (par exemple membranes). Le liner a été caractérisé en présence/absence d'écoulement cisailé et aussi avec un tube à impédance. Finalement, un modèle nouveau est présenté qui est bien d'accord avec ces mesures.

Title: Flow-Acoustic Interaction with Innovative Materials

Key-words: Duct Aeroacoustics, Corrugated Plate, Vibrating Beams, Metamaterials, Whistling

Abstract: This thesis focuses on the aeroacoustic behavior of novel metamaterials in a grazing flow configuration with the scope to understand how the effect of flow plays a role in their acoustic response. Three different materials have been considered and whose analysis compose the corpus of this work. First, the investigation around a corrugated plate in presence/absence of a grazing flow is shown. In recent literature, acoustic investigations on similar surfaces have shown interesting acoustic amplification/attenuation effects at characteristic Strouhal numbers linked to the width (and edge quality) of the corrugations, flow velocity and acoustic frequency. An acoustic and optical experimental setup was used to investigate the linear regime of these disturbances. In the end, the four components that compose the acoustic power have been characterized and their relative importance identified as well as the difference behind gain and loss mechanisms explained. The second part of the thesis is focused on another aspect of flow grazing above metamaterials. As new metamaterials are investigated, often a "magic layer" which would allow acoustics to pass but suppress the sound-flow interactions is theorized. For its realization, a Kevlar fabric layer is equally often indicated, because of its utilization in aeroacoustic wind tunnels. Thus, we show that, while the presence of Kevlar can eliminate flow-sound interactions leading to acoustic amplification and whistling phenomena, this also adds large acoustic losses, which limit interesting resonance effects in metamaterials applications and making it non 'transparent'. Finally, in the third part of this manuscript, a liner concept based on a cantilever beam was investigated. The beam is composed of articulated plates and resistance slits, in order to improve its performance at lower frequencies, especially when compared with other moving surfaces metamaterials (e.g. membranes). The beam was characterized for grazing acoustic incidence in absence/presence of flow as well as in an impedance tube at normal incidence. Finally, a new and simple model is proposed to predict the attenuation of this type of acoustic treatment which agrees with the acoustic measurements.

TABLE OF CONTENTS

	Page
CHAPTER	
1 Introduction	1
CHAPTER	
2 Experimental Setup and Techniques	11
2.1 Introduction	11
2.2 Test Rig	12
2.2.1 Microphones Setup	13
2.2.2 LDV System	14
2.3 Experimental Techniques	15
2.3.1 Scattering Matrix Method	15
2.3.2 LDV Technique	19
2.4 Conclusions	26
CHAPTER	
3 Linear investigation of sound-flow interaction along a corrugated plate	28
3.1 Introduction	28
3.2 Experimental Setup	31
3.2.1 Test Rig	31
3.2.2 Corrugated Walls	31
3.2.3 Mean Flow in the Setup	32
3.2.4 Acoustic velocity Modeling	34
3.3 Results	37
3.3.1 Acoustic measurements	37
3.3.2 LDV Results	40

3.4	Acoustic Power	49
3.4.1	Acoustic Power $\rho_0(\omega'V_0)u_a$ contribution	51
3.4.2	Acoustic Power $\rho_0(\Omega_0v')u_a$ contribution	51
3.4.3	Acoustic Power $-\rho_0(\Omega_0u')v_a$ contribution	53
3.4.4	Acoustic Power $-\rho_0(\omega'U_0)v_a$ contribution	54
3.4.5	Acoustic Power contributions: Summary	56
3.4.6	Effect of Sound Propagation Direction	57
3.4.7	Leading Edge Shape Effect	57
3.5	Conclusions	59

CHAPTER

4	Investigation about Helmholtz resonators and a Transparent Layer	61
4.1	Introduction	61
4.2	Experimental investigation	62
4.2.1	Test rig and measurement procedure	62
4.2.2	Results without Kevlar	65
4.2.3	Results with Kevlar	67
4.3	Numerical approach	68
4.4	Conclusion	71

CHAPTER

5	Vibrating Beams Investigation	73
5.1	Introduction	73
5.2	Vibrating Beams	74
5.3	Cantilever Beam Modeling	76
5.4	Analytical results	80
5.4.1	Influence of the parameters	82
5.4.2	Influence of other modes of the plate	84
5.5	Experimental validation	86
5.5.1	Normal incidence measurements	87
5.5.2	Grazing incidence measurements	93
5.5.3	Effect of flow	96
5.6	Vibrometer Results	97

CHAPTER

6 Conclusions 101

CHAPTER

APPENDIX

A Technical Demonstrator 105

Chapter One

Introduction

Environmental change is one of today's most challenging issue to be takled and therefore requires a strong effort in order to achieve tangible results. The European Community (EC) joined its efforts in its flagship Horizon 2020 (H2020) program which aims at improving synergy between scientific research and industry application by removing barriers to innovation, so to simplify the exchange of knowledge. Among the several fields of interest, Horizon 2020 seeks to make the transportation system cleaner and quieter. For the aviation industry, this is a particularly demanding challenge as these two objectives, with today's technology, push for opposite requirements and fail at providing the substantial reductions which the program pursuits. In this sense, the objective of the H2020 program is to investigate radically new concepts for aeroacoustic attenuation and control in order to overturn these paradigms.

If we look at today's aviation noise mitigation industry, the main technology is represented by the single or multi degree of freedom perforated liners (SDOF and MDOF, respectively). These are constituted by a perforated plate which covers a backing up cavity array (usually in an honeycomb structure). In the SDOF solution, a single layer of cavities is used, while in a MDOF more layers are used, so to introduce multiple resonance frequencies in the liner. Finally, it is a common solution to introduce a resistive layer (mesh wires or similar) which increases the overall damping of the system. The SDOF liner is depicted in figure 1.1 for illustrative purpose.

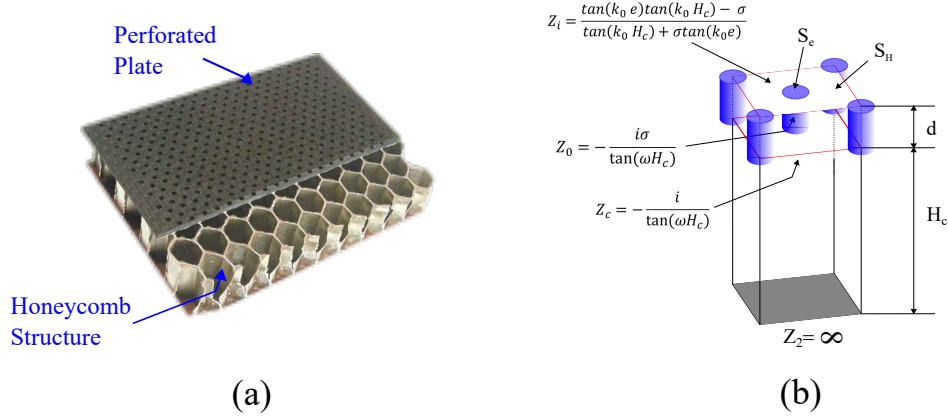


Figure 1.1 – *Illustrative figure of a Single Degree of Freedom acoustic liner (a) and schematic of a single cell (b)*

These kind of liners are built upon the scheme of the classic Helmholtz resonator, which is, in the most general definition, that of a cavity volume connected by a neck to the external ambient. This system can be thought as a mass-spring-damper system and represents an efficient subwavelength system. The spring dynamic is due to the compression of air in the cavity and the mass and the damping by the passage of air through the holes. The way these terms interact with each other (see [1] for a thorough analysis of these terms) gives the system reaction to the acoustic propagation, which is usually characterized by an impedance. The general definition of acoustic impedance is

$$Z = \frac{p'}{\mathbf{v}' \cdot \mathbf{n}} \quad (1.1)$$

where p' and \mathbf{v}' represent the acoustic pressure and velocity, respectively, at the material surface, and \mathbf{n} is the surface normal vector. If we look at a classic Helmholtz resonator, these impedances terms act in series and therefore the total impedance is the sum of these terms. Similarly, it would be the same if we retrieve the impedance of a SDOF (neglecting viscous and other nonlinear effects). Starting from the impedance transport equation for a 1D propagation inside a waveguide:

$$Z_1 = \frac{Z_2 + \rho_0 c_0 j \tan(k_0 L_c)}{\rho_0 c_0 + j Z_2 \tan(k_0 L_c)} \quad (1.2)$$

where Z_1 and Z_2 are the impedances at two points distant a length L_c , and k_0 is the wavenumber inside the waveguide. If we apply this formula at our case, as shown in figure 1.1-b, we retrieve the impedance expression for a cell of this SDOF system as

$$Z_L/\rho_0c_0 = \frac{i \tan k_0d \tan k_0H_c - \sigma}{\sigma \tan k_0H_c + \sigma \tan k_0d} \quad (1.3)$$

where d , H_c and σ are the thickness of the perforated plate, the height of the cavity and the Percentage of Open Area, POA(i.e. ratio between the perforated hole area and the underlying cavity) $\sigma = S_e/S_H$ (again, see figure 1.1-b); ρ_0 and c_0 are the density and the speed of sound inside the waveguide, respectively. Then, if the thickness and cavity depth are much smaller than the propagating acoustic wavelength, equation 1.3 can be approximated as

$$Z_L/\rho_0c_0 \approx \frac{i}{\sigma} \left(k_0d - \frac{\sigma}{k_0H_c} \right) \quad (1.4)$$

and the resonance frequency of such a system is obtained when the imaginary part of this impedance is equal to zero, i.e.

$$\omega_r = c_0 \sqrt{\frac{\sigma}{dH_c}} \quad (1.5)$$

which is the resonance frequency of an Helmholtz resonator whose neck has a thickness d and a volume depth H . In figure 1.2, the resonance frequency obtained through eq. 1.3 is traced as a function of the POA (for reference values $d = 1\text{mm}$ and $H = 25\text{mm}$). We can see how at low POA the curve becomes very close to the one of an Helmholtz resonator while, at very large POA grows asymptotically towards the resonance frequency of a quarter wavelength resonator, $f_r = c_0/4(H + d)$.

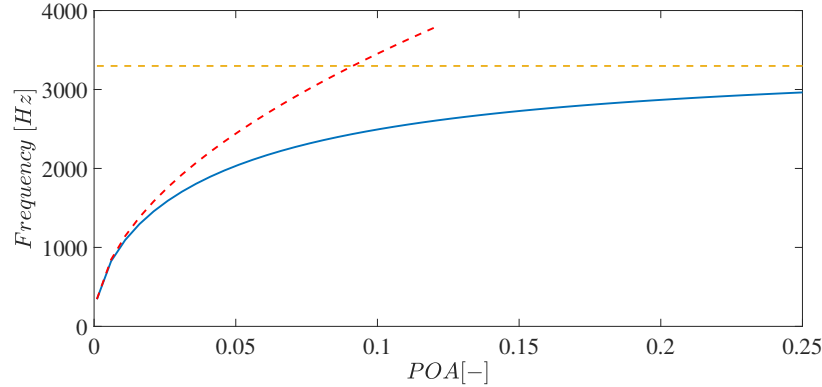


Figure 1.2 – Resonance frequency as a function of the POA value for a SDOF liner (blue), an Helmholtz resonator (red dash line) and of an equivalent quarter wavelength resonator (yellow dash line)

Therefore, even if it is possible to tune such a system towards low resonance frequencies, this is not practically possible due to space constraint as, at all POA, its dependency on the cavity height is unfavourable. Even more so, as the future request for aero-engines will be to increase the nacelle sections (for improved air intake and thus fuel consumption efficiency) and the available space for acoustic treatments will be reduced.

Therefore, several novel approaches have been investigated, in order to improve the efficiency of such a system (or even change the underlining paradigm). For example, it could be possible to back up the perforated plates by a porous material element, laying on a rigid backing, in order to increase the frequency spectrum response. However, in such a configuration, the main possibility to shift the frequency response to lower frequencies is by increasing the porous layer thickness. Another approach is then proposed by [2] and [3], where the micro-perforate is supported by cavities into which tubes extend. In [2] the analytical background for the perforated panel with extended tubes (PPET) is provided, together as well with an optimization procedure for achieving the average best absorption over a given frequency spectrum. In [3], a similar configuration of a perforated plate with extended plastic tube is presented and modeled both by a transfer matrix method and with a Linearized Euler Equations (LEE) approach. Also, it is interesting that an experimental

example was used to validate these models in a grazing flow configuration. In both works, the resulting effect of the tubes is to add further inertial and resistance terms to the ones from cavity and perforated holes. These added terms depend on the relative length of the tubes w.r.t. the cavity depth other than the cross-section area ratio (see figure 1.3 for the schematics of the systems).

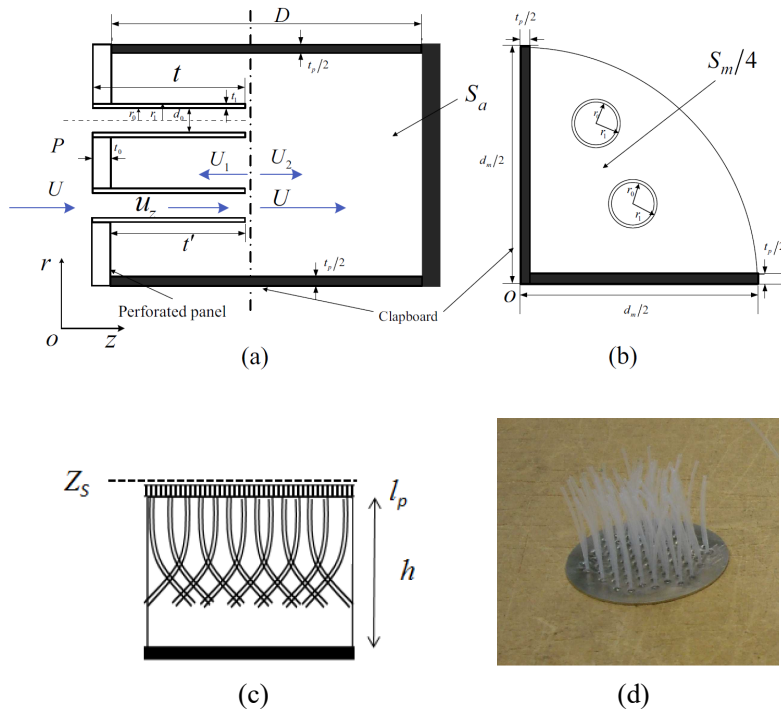


Figure 1.3 – Schematics of one unit of the four parallel-arranged PPETs from [2]: (a) Side elevation and (b) front elevation. The perforated plate investigated in [3] is shown by its (c) schematics and (d) realization of the perforated plate investigated in [3]

Another approach which was able to push even further the subwavelength efficiency of the acoustic metamaterials (i.e. the ratio between its characteristic resonance wavelength and thickness) was the one based on the "slow sound" concept. In this case, the idea is to decrease the sound speed in the material in order to obtain attenuation at a frequency lower than the natural frequency of the impedance. In such a sense, the acoustic liner is

working in the same way as before, but a shift in the resonance frequency is introduced as large as the sound speed reduction therefore enhancing subwavelength attenuation. This is straightforward to show, as for a quarter-wavelength resonator the resonance wavelength is

$$H = \lambda_r/4 = \frac{c_e}{4f_r} \rightarrow f_r = \frac{c_e}{4H} \quad (1.6)$$

where the quantities are the same as indicated above. Then, it is clear that the same liner can reduce its resonance frequency by simply reducing the sound speed (inside its volume). In [4], side branches are laterally included in a slit structure to create a locally reacting impedance (see figure 1.4). The conceived structure is proved, both from a modeling and experimental point of view, to slow the sound speed and therefore deliver optimal absorption at a critical wavelengths much larger than four times the typical length of the impedance.

Finally, another approach regarded with large interest in literature is the use of membranes and vibrating materials. This approach has been investigated both from a passive and active point of view, the difference being that in the latter case energy is given to the system from an external source (e.g. a loudspeaker). Vibrating membranes have been first investigated by [5] and used for a first application in [6]. Recent works have investigated hybrid resonances obtained through a backed up cavity sealed off and filled with a low adiabatic index (i.e. low heat capacity ratio) gas [7].

Regarding the active solution, a largely investigated idea is to drive an electro-mechano-acoustical system (i.e. a loudspeaker membrane) to adapt its impedance toward the optimal value of the system. This is achieved through electroacoustic absorption (see [8]), which can be obtained through many strategies (for further details see [9] and [10]). Even if these solutions offer a very interesting and efficient answer to the noise mitigation challenge, the situation can change when we consider the presence of an external flow grazing over the metamaterials surfaces.

In fact, several studies have investigated how such interactions were responsible for unexpected and surprising phenomena and therefore to be taken into account. In [11], the

performance of a classic perforated liner was analysed with and without a grazing mean flow. The experimental analysis was conducted with two sets of microphones before and after the lined section, from which the scattering matrix can be obtained. In absence of flow, the transmission coefficient shows an attenuation peak near the quarter-wavelength resonance frequency of its locally reacting resonators. On the other hand, when a grazing flow is turned on, an actual amplification (i.e. transmission coefficient > 1) of the acoustic wave appears around the same resonance frequency. Other works [12] show how the performances for which metamaterials are designed in no flow condition, very often deteriorate greatly when a grazing flow is present: in this case, a thin subwavelength coiled solution has been analysed and results show that the presence of flow reduces the transmission loss of the metamaterial by a factor 100 (see figure 1.4).

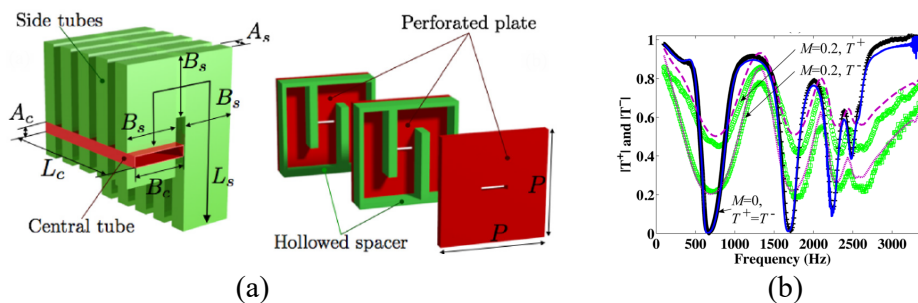


Figure 1.4 – Outline of the material investigated in [12] (a) and its Transmission coefficient (b): blue/black marks are obtained without an external flow, while the green lines are with a $M=0.2$ flow. A 100 factor increase in the Transmission curve can be seen around the first resonance frequency. Figure from [12]

Together with newly available experimental investigations, also new theoretical considerations have been an important push towards research in this field. In [13] the well-posedness of the Ingard-Myers boundary condition for liners in grazing flows has been investigated. It is a very common way of modeling the interaction at the liner interface through its impedance. However, as Brambley shows, this is proven to be ill-posed and therefore produce unstable analysis, especially in time domain. Therefore, new research was needed in order to prop-

erly model the aero-acoustic interaction for those applications where a mean flow is present such as aviation, ventilation or turbomachinery. To obtain new detailed informations of this interaction in the vicinity of liners, optical techniques have proven to be very helpful: in [14] the numerical investigation of the effects of flow and high amplitude acoustics has been carried out for SDOF liners. Here, the thesis focused on different aspects of acoustic propagation (mainly for a single perforated resonator) in a normal and grazing configuration, for different sound levels and in presence of flow. The comparison with LDV data shows good agreement in defining the mechanisms of dissipation, especially at large amplitude (e.g. vortex shedding), as shown for example in figure 1.5

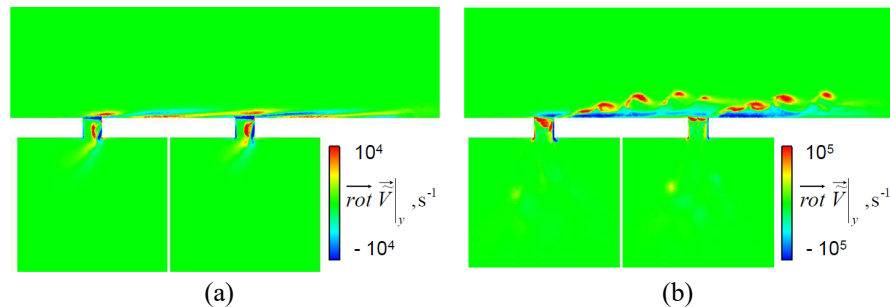


Figure 1.5 – *Vorticity field for a grazing flow ($M = 0.1$) configuration for (a) 114 and (b) 140.5 dB sound level, at $f=1592$ Hz (figure from [14])*

The importance of including the aeroacoustic interactions is shown also in different kinds of applications, like acoustic directivity, cloaking and other innovative application. Most investigations about cloaking are either theoretical or numerical and they offer require extreme parameters which also offer frequency-dispersive metamaterials. Therefore they can work in a limited frequency range. If the scatterer is put on a flat reflective ground, cloaking is easier to achieve [15], but these metamaterials cloak capability is disrupted when subjected to an external flow. However, when considering the presence of an external flow, its influence inside the metamaterial is neglected. If flow is present, then the governing equations are not anymore formally invariant and therefore cloaking is not achieved [16]. Therefore,

in these cases the fluid is considered quiescent. There has been various extensions to these approaches by including a convective component to the Taylor transformation [15] or topological approaches. However, in these cases, the metamaterial is needed to be permeable to the incoming acoustic waves which means that, at the same time, it would be exposed to the aero-acoustic interaction due to an external flow that could alter its performance. Then, in order to concile these two needs, it is assumed that the metamaterial is shielded in some way from the convective component (i.e. the external flow) but not the acoustic one. Therefore, these results are interesting but they can't indicate a practical way for their realization or, alternatively, require the strong assumption that only the acoustics are able to enter the metamaterial, while the flow is not. Furthermore, sometimes it has been indicated that such layer can be fabricated with a Kevlar layer. Therefore, a part of this thesis is devoted to the investigation of an array of Helmholtz resonators in presence of an external flow, with and without a covering Kevlar layer. As the resonators alone produce dramatic effects with flow (i.e. whistling), it is shown that a Kevlar layer is able to suppress them, but at the same time suppressing the effects of the metamaterial by introducing a very important acoustic dissipation and that, contrary to what is often stated, it is not the magic layer advertised.

Finally, moving aside from the realm of metamaterials but in line with flow effects on materials, interesting effects can be observed on corrugated walls when an external mean flow is present. In these, self-induced oscillations which could result in fatigue-related failures or noisy disturbances have been noticed and their nature linked to the corrugated surface of attached piping inner layer [17]. Therefore, the investigation of the arising of these phenomena is interesting both from a research and industrial point of view: in this thesis, the behaviour of these interactions in the linear domain have been studied.

In the present thesis different problems have been tackled, mainly from an experimental point of view. Therefore, in Chapter 2, the experimental setup built has first of all been shown in detail.

In Chapter 3, an experimental investigation by means of acoustic and optical measurements

of the aero-acoustic interaction along a corrugated plate has been carried out.

In Chapter 4 the influence of a kevlar resistive layer around a metamaterial (an in series Helmholtz configuration) has been investigated. Furthermore, in Chapter 5 an investigation of a vibrating cantilever beam array in normal and grazing configuration has been carried out.

Finally, in Chapter 6 Conclusions are drawn.

Chapter Two

Experimental Setup and Techniques

2.1 Introduction

In this section, the ensemble of the test rig and the experimental techniques have been presented. While in the next Section the detailed dimensions of this test rig are presented, the justifications of the design can be outlined here. As the investigations carried out in this thesis are mainly focused around the linear regime, it was important to exclude any higher order modal content (i.e. having only planar waves) from the measurements while still operating up to mid range frequencies. In fact, the cut-on frequency for a square section duct can be written as:

$$f_{cut} = \frac{c_0}{2H} \quad (2.1)$$

where $H = 40$ mm is the height of the channel. For standard conditions, $f_{cut} \approx 4300$ Hz. From this, it is clear that the upper frequency limit where only one mode is present is inversely proportional to the test section dimensions. Furthermore, it is important to notice that both ends of the duct were equipped with anechoic terminations. This allows precise Transmission-Reflection measurements and suppresses any feedback signal which could lead to whistling phenomena in the investigated problems.

2.2 Test Rig

The test rig is a uniform rectangular duct whose section is $B = 50 \text{ mm} \times H = 40 \text{ mm}$, see figure 2.1. In this duct, a mean flow is produced by a centrifugal fan whose flow rate can be continuously adjusted up to a mean velocity of 85 m/s. The flow velocity is measured by a Pitot tube (diameter 2.1 mm) in the center of the rectangular duct and by Laser Doppler Velocimetry (LDV). The duct has upstream and downstream anechoic terminations which ensure low reflection coefficients on both side of the studied corrugated plate. The upstream anechoic termination is sealed to prevent any leakage of the mean flow From this upstream termination up to the studied element, a 1.90 m long rigid pipe segment is installed to allow a complete development of the flow. The investigated element is located in a test section of length $L = 200 \text{ mm}$. To allow access for optical measurements, a side wall and the top wall are made of glass, the floor being the position of the tested acoustic treatments that can be easily changed. Downstream of the test section, a second rigid duct segment connects to the downstream anechoic termination. The sound field is produced by a compression driver (Beyma CP850Nd) which can provide an acoustic level up to 150 dB SPL in the test section over a frequency range from 500 to 4000 Hz. The acoustic source can be placed either upstream or downstream of the studied element in order to obtain two different states of the system.

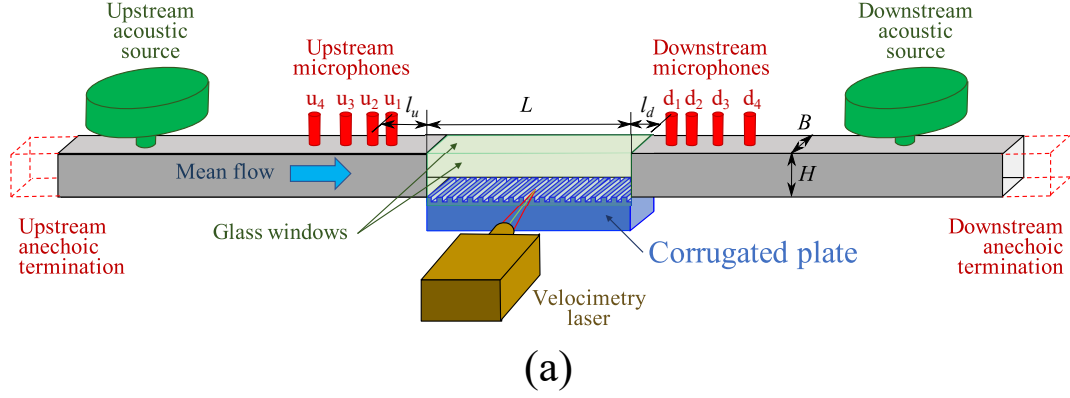


Figure 2.1 – Schematic view (a) and photo (b) of the experimental setup

2.2.1 Microphones Setup

The test rig has been conceived so that both acoustic and optical measurements could be carried out exactly on the same test section. In order to determine the transmission and reflection coefficients, T^\pm and R^\pm , of the tested element, the upstream and downstream rigid ducts are equipped with 4 microphones each. The superscripts $+/-$ indicate whether the quantities are calculated in the case of an acoustic propagation along or against the mean flow. Those eight quarter-inch microphones are mounted flushed to the duct without grids (B&K 4136 with Nexus 2690 amplifier). The distances between the first microphone and the test object are $l_u = 0.112$ m, $l_d = 0.114$ m. The distances between the microphones are $x_{u2-u1} = x_{d2-d1} = 0.030$ m, $x_{u3-u1} = x_{d3-d1} = 0.175$ m and $x_{u4-u1} = x_{d4-d1} = 0.462$

m. As the investigated frequencies are well below the cut-on frequency of the rigid straight duct (i.e. 4287.5 Hz), only plane waves propagate to the test section. Thus, the pressure at any point in the duct (sufficiently far from the source position and from any change in the duct) can be described by $p(x) = p(x)^+ e^{-jk^+x} + p(x)^- e^{jk^-x}$ where k^\pm is the wavenumber accounting for the flow and the visco-thermal losses in the acoustic propagation. The four microphones at both side of the test section allow an over-determination of the incoming and outgoing acoustic waves upstream and downstream of the tested element [11]. Using the two acoustic sources to obtain two different acoustic states of the system [18], the four elements of the scattering matrix for plane waves (transmission and reflection coefficients on both directions: T^\pm and R^\pm) can be evaluated.

2.2.2 LDV System

A 2D Laser Doppler Velocimetry (LDV) DANTEC 2D FlowExplorer system has been set up and used to measure the vertical (V along y) and horizontal (U along x) velocities inside the chosen cavity. Its lasers wavelengths are of 532 and 560 nm at a $f=300$ mm focus length. The system has a measurement volume of 0.7 mm^3 and its support system is capable of displacing with a spatial resolution of 0.10 mm. Therefore, the resolution attainable inside the cavity is hardly beatable by other (optical and not) techniques. The LDV system comes together with a Burst Spectrum Analyzer (BSA) Dantec software which manages the laser position in space and the acquisition procedure and allows measurements on a 2D points grid in space. Regarding the acquisition procedure, main attention has to be given to the synchronization between the laser and the acoustic source, in order to have measurements throughout the whole reference signal period. This could be done by a phase-locked approach but, in order to reduce errors (e.g. data folding over one period), and as we are working at a single fixed frequency, a simpler approach was used. A source signal, produced by a frequency generator, feeds both the loudspeaker through an amplifier and the LDV trigger

entrance. This feeding signal is again split to the loudspeakers and reacquired into the LDV acquisition system (so to always know the reference electronic signal fed to the system). In this way, we can radiate a single frequency signal in the duct while having a reference trigger for the acquisition system always identically synchronized at the same time reference. This appears to be even more important when we have to correlate two sub-volumes data, which was needed for the corrugated plate, as explained later in Section 3.2.1.

Finally, scattering particles are needed to measure quantities inside the free flow. Here, incense particles have been used since they produce favorable diameters smoke particles d_c [19], [20],[21], which equals to a Stokes number of $Sk = (2\pi f/\nu)^1/2d_c \sim 0.006 - 0.008$ if we also consider the typical forcing frequency of $2kHz$ and a dynamic viscosity of air of $\nu = 1.81 * 10^{-5}[kg m^{-1}s^{-1}]$. This value is obtained by applying the formula from [22]

$$Sk = \left(\frac{\omega}{\nu}\right)^{\frac{1}{2}} d_p \tag{2.2}$$

where ω is the forcing frequency, ν the dynamic viscosity of air and d_p the particle diameter.

2.3 Experimental Techniques

As described in the previous section, two different experimental setups are available to carry out acoustic measurements. In this section a brief description about these procedures is given.

2.3.1 Scattering Matrix Method

The first and more classic way of measure acoustic quantities is by the means of microphones. In our case, the general idea is to retrieve the scattering matrix from the microphone mea-

surements picked up outside the test section

$$\begin{pmatrix} p_2^+ \\ p_1^+ \end{pmatrix} = [S] \begin{pmatrix} p_2^- \\ p_1^- \end{pmatrix} \quad (2.3)$$

where $[S]$ is the scattering matrix and the subscripts 1,2 indicates a fixed position before and after the test section, respectively. As outside the test section, we only consider plane waves propagation, it is possible to write:

$$\begin{aligned} p_1 &= p_1^+ e^{-jk^+ x_1} + p_1^- e^{jk^- x_1} = p_1^+ \left(e^{-jk^+ x_1} + R_1 e^{jk^- x_1} \right) \\ p_2 &= p_2^+ e^{-jk^+ x_2} + p_2^- e^{jk^- x_2} = p_2^+ \left(e^{-jk^+ x_2} + 1/R_2 e^{jk^- x_2} \right) \end{aligned} \quad (2.4)$$

where x_1, x_2 are the positions of microphones 1, 2 and $R_{1,2}$ are respectively

$$\begin{aligned} R_1 &= \frac{p_1^-}{p_1^+} \\ R_2 &= \frac{p_2^+}{p_2^-} \end{aligned} \quad (2.5)$$

Then, we are interested in retrieving the scattering matrix coefficients

$$[S] = \begin{bmatrix} T^+ & R^- \\ R^+ & T^- \end{bmatrix} \quad (2.6)$$

which are the transmission and reflection coefficients when the corresponding termination is anechoic. For example

$$\begin{aligned} T^+ &= \frac{p_2^+}{p_1^+}, \\ R^+ &= \frac{p_1^-}{p_1^+}, \end{aligned} \quad \text{when } p_2^- = 0 \quad (2.7)$$

and similarly for the other coefficients. Then, we can write the scattering matrix as the link between the downstream and upstream running pressures

$$\begin{pmatrix} p_2^+ \\ p_1^+ \end{pmatrix} = \begin{bmatrix} T^+ & R^- \\ R^+ & T^- \end{bmatrix} \begin{pmatrix} p_2^- \\ p_1^- \end{pmatrix} \quad (2.8)$$

which can be normalized by the p_1^+ pressure, giving

$$\begin{pmatrix} T_{12} \\ R_1 \end{pmatrix} = \begin{bmatrix} S \end{bmatrix} \begin{pmatrix} 1 \\ T_{12}/R_2 \end{pmatrix} \quad (2.9)$$

where $T_{12} = \frac{p_1^+}{p_2^+}$. If we want to retrieve the four scattering matrix coefficients, the above relation will require two different measurements obtained at two different system states. The most common way to achieve this is either changing the termination load of the system (i.e. changing the impedance of the termination) or by switching the position of the acoustic source. The latter method has been used mainly because of its malleability and because it allows us to work always with termination reflection factors as small as possible. Then, if it is possible to retrieve Eq. 2.8 w.r.t. two different states (a), (b), we obtain globally 4 unknowns in 4 equations

$$\begin{pmatrix} T_{12}^{(a)} \\ R_1^{(a)} \end{pmatrix} = \begin{bmatrix} T^+ & R^- \\ R^+ & T^- \end{bmatrix} \begin{pmatrix} 1 \\ T_{12}^{(a)}/R_2^{(a)} \end{pmatrix} \\ \begin{pmatrix} R_2^{(b)} \\ T_{21}^{(b)} \end{pmatrix} = \begin{bmatrix} T^+ & R^- \\ R^+ & T^- \end{bmatrix} \begin{pmatrix} T_{21}^{(b)}/R_1^{(b)} \\ 1 \end{pmatrix} \quad (2.10)$$

where in this case $T_{21} = \frac{p_2^-}{p_1^-}$. Then, combining these two equations we retrieve the expressions of the four scattering coefficients

$$\begin{aligned} T^+ &= T_{12}^{(a)} \left(1 - \frac{R_2^{(b)}}{R_2^{(a)}} \right) \left(1 - \frac{T_{12}^{(a)} T_{21}^{(b)}}{R_2^{(a)} R_1^{(b)}} \right)^{-1} \\ R^+ &= R_1^{(a)} \left(1 - \frac{T_{12}^{(a)} T_{21}^{(b)}}{R_1^{(a)} R_2^{(a)}} \right) \left(1 - \frac{T_{12}^{(a)} T_{21}^{(b)}}{R_2^{(a)} R_1^{(b)}} \right)^{-1} \\ T^- &= T_{21}^{(b)} \left(1 - \frac{R_1^{(a)}}{R_1^{(b)}} \right) \left(1 - \frac{T_{12}^{(a)} T_{21}^{(b)}}{R_2^{(a)} R_1^{(b)}} \right)^{-1} \\ R^- &= R_1^{(a)} \left(1 - \frac{T_{12}^{(b)} T_{21}^{(a)}}{R_1^{(b)} R_2^{(b)}} \right) \left(1 - \frac{T_{12}^{(a)} T_{21}^{(b)}}{R_2^{(a)} R_1^{(b)}} \right)^{-1} \end{aligned} \quad (2.11)$$

These expressions link the scattering coefficients to the transmission and reflection coefficients actually measured. Then, the last thing to be defined is how to retrieve these coefficients from the microphone measures.

Once the time signal has been acquired, a transfer function (which accounts for calibration factors) between two microphones at two distinct positions can be defined as

$$H_{ij}(f) = \frac{p_i(f)}{p_j(f)} \quad (2.12)$$

where $p_i(f)$ is the Fourier transform of the pressure time signal $p_i(t)$. Then, the aforementioned coefficients can be rewritten as a function of these transfer functions by noting that

$$\begin{aligned} p_j^+(x_j) &= p_1^+(x_1)e^{-jk_1^+(x_j)} \\ p_j^-(x_j) &= p_1^-(x_1)e^{jk_1^-(x_j)} \\ p_i^+(x_i) &= p_1^+(x_1)e^{-jk_1^+(x_i)} \\ p_i^-(x_i) &= p_1^-(x_1)e^{jk_1^-(x_i)} \end{aligned} \quad (2.13)$$

and so

$$H_{ij} = \frac{e^{-jk_1^+x_i} + R_1e^{jk_1^-x_i}}{e^{-jk_1^+x_j} + R_1e^{jk_1^-x_j}} \quad (2.14)$$

Finally, shuffling the terms to express directly the reflection coefficient, we obtain

$$R_1 = \frac{H_{ij}^1 e^{-jk_1^+x_j} - e^{-jk_1^+x_i}}{e^{jk_1^-x_i} - H_{ij}^1 e^{jk_1^-x_j}} \quad (2.15)$$

and similarly the other coefficients are retrieved.

Lastly, it must be noted that 2 microphones (on both sides) are sufficient to retrieve the four coefficients. However, an overdetermination is foreseeable in principle, as it will improve greatly the signal-to-noise ratio (over a larger frequency spectrum). In this case, we can write the problem through a matrix form as

$$\begin{pmatrix}
-H_{ij}^1 e^{jk_1^- x_{1j}} + e^{jk_1^- x_{1i}} & 0 & 0 \\
-H_{ik}^1 e^{jk_1^- x_{1k}} + e^{jk_1^- x_{1i}} & 0 & 0 \\
\vdots & \vdots & \vdots \\
-H_{in}^1 e^{jk_1^- x_{1n}} + e^{jk_1^- x_{1i}} & 0 & 0 \\
-H_{ii}^1 e^{jk_1^- x_{1i}} + e^{jk_1^- x_{1i}} & 0 & 0 \\
-H_{jj}^{21} e^{jk_1^- x_{1j}} & e^{jk_2^- x_{2j}} & e^{-jk_2^+ x_{2j}} \\
-H_{kk}^{21} e^{jk_1^- x_{1k}} & e^{jk_2^- x_{2k}} & e^{-jk_2^+ x_{2k}} \\
\vdots & \vdots & \vdots \\
-H_{nn}^{21} e^{jk_1^- x_{1n}} & e^{jk_2^- x_{2n}} & e^{-jk_2^+ x_{2n}}
\end{pmatrix} \times \begin{pmatrix} R_1 \\ T_{12}/R_2 \\ T_{12} \end{pmatrix} = \begin{pmatrix}
-e^{-jk_1^+ x_{1i}} + H_{ij}^1 e^{-jk_1^+ x_{1j}} \\
-e^{-jk_1^+ x_{1i}} + H_{ik}^1 e^{-jk_1^+ x_{1k}} \\
\vdots \\
-e^{-jk_1^+ x_{1i}} + H_{in}^1 e^{-jk_1^+ x_{1n}} \\
-H_{ii}^{21} e^{-jk_1^+ x_{1i}} \\
-H_{jj}^{21} e^{-jk_1^+ x_{1j}} \\
-H_{kk}^{21} e^{-jk_1^+ x_{1k}} \\
\vdots \\
-H_{nn}^{21} e^{-jk_1^+ x_{1n}}
\end{pmatrix} \quad (2.16)$$

and retrieve the solution through a least square approach.

2.3.2 LDV Technique

The Laser Doppler Velocimetry (LDV) is an optical technique used to measure the peculiar velocity of a given flow. The technique consists in measuring the frequency difference between the laser signal scattered by some reflective particles inside the fluid and a reference one. The system uses two laser beams which, interfering with each other, create fringe patterns: the refracting particle passing through these fringes will re-emit a light signal with a frequency shift linked to its velocity and the fringe spacing, due to the Doppler effect. In Figure 2.2, a schematic of the basic mechanism is shown. Two laser beams $\bar{\mathbf{u}}_1, \bar{\mathbf{u}}_2$ with an identical wavelength λ_0 are shed so to interfere themselves at a given measurement point. When a scattering particle with a velocity $\bar{\mathbf{v}}_0$ passes at this point, it will diffuse two waves which, when superimposed, modulate in amplitude the light intensity at a frequency

$$F_D = F_{u_2} - F_{u_1} = \frac{1}{\lambda_0} \bar{\mathbf{v}}_0 \cdot (\bar{\mathbf{u}}_1 - \bar{\mathbf{u}}_2) \quad (2.17)$$

or equivalently

$$F_D = \frac{v_x}{d} \quad (2.18)$$

where v_x is the velocity component normal to the two laser beams bysect. The distance d is linked to the laser beams interference process: as these are highly coherent, their crossing creates interference patterns. Particularly, fringes characterised by high and low light intensity appear inside a measurement volume (see Figure 2.2). The length d is the spacing between two fringes peaks (or valleys). In the hypothesis of gaussian cylindrical beam profiles, it can be related to the the angle between the two laser beams θ_0 and the laser wavelength λ_0 by

$$d = \frac{\lambda_0}{2 \sin(\theta_0/2)} \quad (2.19)$$

These fringes will occupy a measurement volume which depends on the characteristics of the laser beam profile. If this can be considered gaussian, we can define a focusing length d_f

$$d_f = \frac{4w_f \lambda_0}{\pi d_0} \quad (2.20)$$

where w_f is the focal distance and d_0 the beam diameter. Then, the length d_{x_0} indicated in Figure 2.2, can be calculated as $d_{x_0} = \frac{d_f}{\cos(\theta_0/2)}$. Finally, as mentioned in 2.2.2, in order to detect a light signal, a scattering particle is needed inside the flow but it should also point out that the measured velocity will be that of a single particle: therefore, a large number of acquisitions are required so to reconstruct in a statistical way the mean and variance of the bulk ve-

locity.

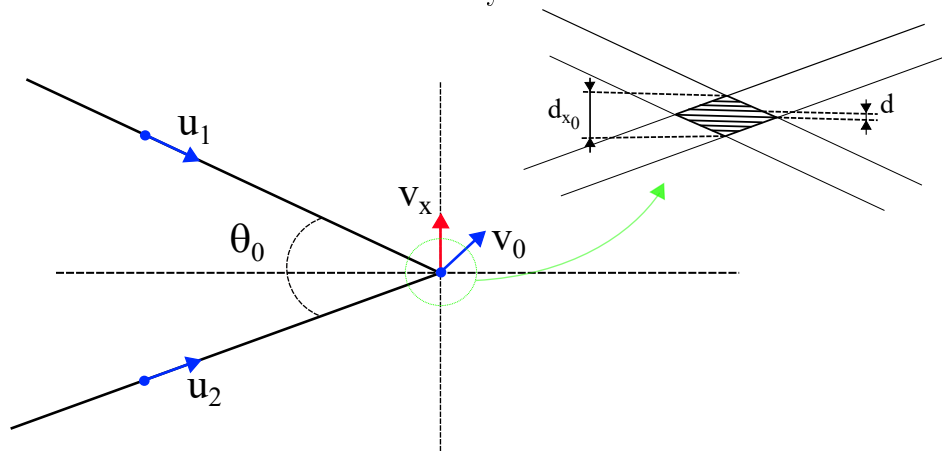


Figure 2.2 – *Schematics of an LDV measuring system*

The velocity retrieved in this way has three main contributions:

$$\mathbf{u} = \mathbf{U}_0 + \mathbf{u}' + \mathbf{u}_t \quad (2.21)$$

which are respectively the time-averaged, the phase-averaged coherent and the turbulent velocity vectors. The phase-averaged component is the time dependent velocity at the frequency of the acoustic source and therefore will be described as

$$\mathbf{u}' = a' \sin(2\pi f_s t + \phi), \quad (2.22)$$

where f_s is the acoustic source frequency. The turbulent component \mathbf{u}_t accounts for the remaining time dependent component inside the velocity signal.

In order to retrieve the periodic component of the velocity, measurements could be carried out through a phase locked approach, where different measurements at different positions along the fed signal cycle are needed. This implies that these data need to be folded inside the same cycle, introducing a truncation error. In our case, as the signal frequency is known and constant, we decided to directly investigate the presence of such a sinusoidal signal (whose amplitude and phase have to be retrieved) inside the whole temporal acquired data. The first step consists in checking that the signal frequency remains constant all over the acquisition window. In fact, if the time window width becomes large (mainly according to the seeding particle density at measurement point), this frequency could suffer a drift. Therefore, the fed sinusoidal signal is also reacquired and these acquisition points are folded into one cycle: if the drift exists, it will induce an uncertainty interval around the pure sine. Then, a frequency correction which minimizes such spread is introduced and a corrected frequency is obtained.

Figure 2.4-a shows the total, coherent and mean velocities for a single spatial position, while in Figure 2.4-b the corresponding histogram points out the gaussian nature of the velocity distribution. In Figure 2.4-a, the velocities have been folded over one period as a function

of the phase, in order to enhance readability. It can be noticed that the coherent velocity component is rather smaller than the turbulent one, suggesting that, in order to reduce the error in the coherent component, a large number of particle velocities is needed. This can also be appreciated from Figure 2.3, where the amplitude and phase of the coherent velocity have been traced as a function of the number of measured particles through the volume of measurement. The subscript N represents the velocity measured for a given number N of particles while the subscript s indicates the final ‘steady’ value. We can see a convergence towards the steady value as the number of retrieved particles increases.

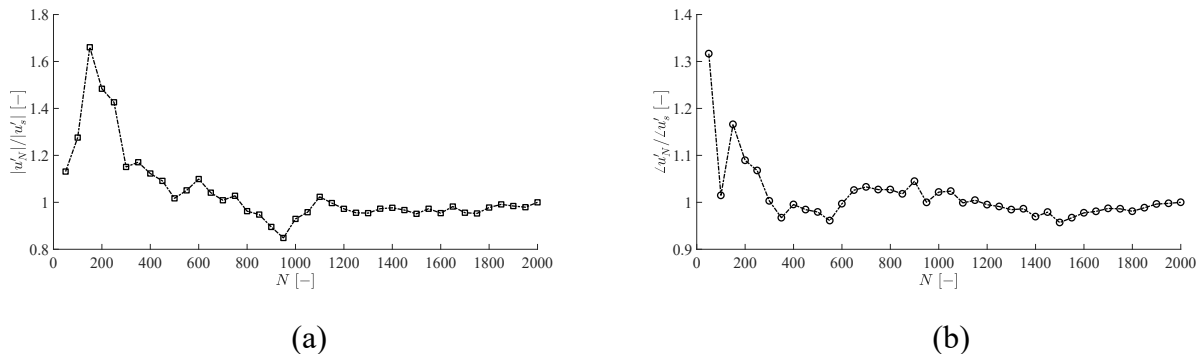


Figure 2.3 – Retrieved amplitude (a) and phase (b) of the vertical fluctuating velocity at a given position in space as a function of the number of measured particles.

At this point, we could retrieve the fluctuating velocity component at this corrected frequency with different methods. However, as it can be inferred from Figure 2.5, the main task is to retrieve the phase-averaged component from a non-uniformly sampled signal. This means that, in order to use any method based on Fourier transformed signals (FFT, Welch), some kind of interpolation has to be introduced to have a uniform sampling and corrections have to be adopted in order to deal with the related bias introduced. Another approach is to keep the non-uniform sampling and adopt methods based on the minimisation of a cost function. From literature [23, 24], it can be shown that a least-square based Maximum Likelihood (ML) method will asymptotically reach the theoretical lowest bound (i.e. the Cramer-Rao bound) in independent Gaussian white noise conditions. This means that in such conditions it will asymptotically achieve the minimum estimation error. Then, as the

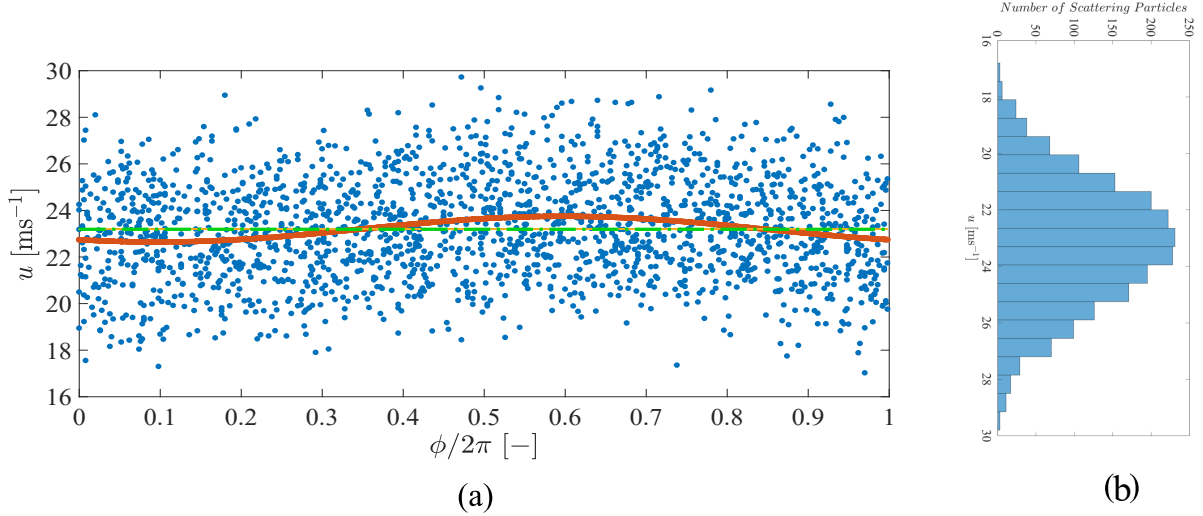


Figure 2.4 – *Example of retrieved fluctuating horizontal velocity at a given position in space (a) and relative histogram (b). The total acquired and the reconstructed coherent velocities are shown in dots and solid orange line, respectively, after being carried over a single (nondimensionalised) time period. Finally, the green dash-dotted line represents the time-averaged velocity.*

assumption of gaussian distribution of the turbulent velocity components is usually well put and therefore makes the method viable. Finally, the algorithm has been tested on a synthetic sinusoidal signal at sampling conditions close to measurements giving satisfactory results.

The ML model tries to minimize the squared difference between the measured signal and a pure synthetic sinusoidal signal, whose frequency is known and equivalent to our source signal.

This means that, if the velocities available data are $x[n]$ at discrete times t_n , for $n \in [0, N-1]$, the aim is to fit these data with the following model

$$\hat{x}[n] = \alpha_0 \sin(2\pi F_0 t_n + \phi_0) + C \equiv A s_n + B c_n + C, \quad (2.23)$$

with F_0 and t_n known, α_0 , ϕ_0 and C unknown. We also note $A = \alpha_0 \cos(\phi_0)$, $B = \alpha_0 \sin(\phi_0)$, $\phi_n = 2\pi F_0 t_n$, $s_n = \sin(\phi_n)$ and $c_n = \cos(\phi_n)$. Furthermore, we suppose that

$$x[n] = A s_n + B c_n + C + b[n], \quad (2.24)$$

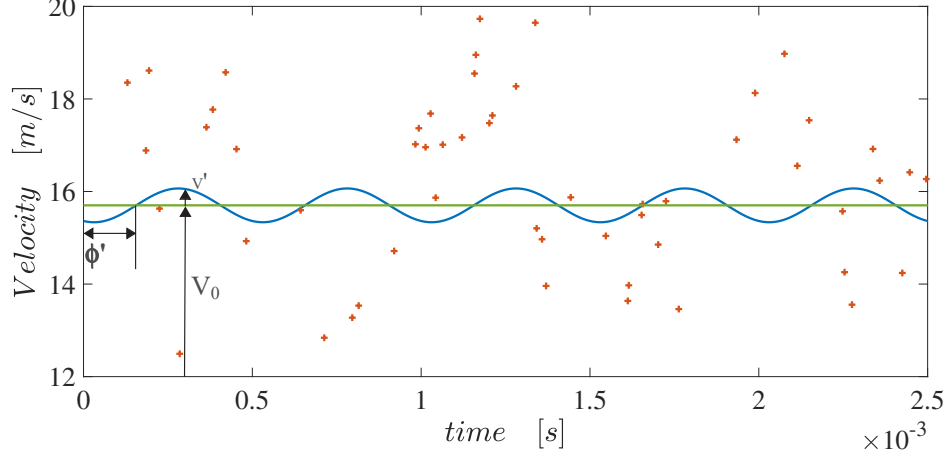


Figure 2.5 – *Example of horizontal retrieved fluctuating velocity over a small part of an acquisition window (total width is 0.08 s). The solid green (—) line represent the time-averaged velocity, the + symbol represents the total retrieved velocity, while the solid blue (—) line represents the fitting sine model*

with $b[n]$ a white gaussian noise with variance σ_b^2 .

Then, from the available data $x[n]$ and from the model $\hat{x}[n]$, we define the cost function

$$J = E[(x[n] - \hat{x}[n])^2] = E[(x[n] - As_n - Bc_n - C)^2] = \frac{1}{N} \sum_{n=0}^{N-1} ((x[n] - As_n - Bc_n - C)^2) \quad (2.25)$$

where $E[\cdot]$ represents the expectance operator which, under the classical assumption of ergodicity, may be replaced by the summation $\frac{1}{N} \sum_{n=0}^{N-1}$ as above.

Then, differentiating J according to the unknown vector $\theta = \{A, B, C\}$ leads to

$$\begin{cases} \frac{\partial J}{\partial A} = 0 = AE[s_n^2] - E[s_n x[n]] + BE[c_n s_n] + CE[s_n] \\ \frac{\partial J}{\partial B} = 0 = BE[c_n^2] - E[c_n x[n]] + AE[c_n s_n] + CE[c_n] \\ \frac{\partial J}{\partial C} = 0 = C - E[x[n]] + AE[s_n] + BE[c_n] \end{cases} \quad (2.26)$$

or, equivalently,

$$\begin{pmatrix} E[s_n^2] & E[c_n s_n] & E[s_n] \\ E[c_n s_n] & E[c_n^2] & E[c_n] \\ E[s_n] & E[c_n] & 1 \end{pmatrix} \cdot \begin{pmatrix} A \\ B \\ C \end{pmatrix} = \begin{pmatrix} E[s_n x[n]] \\ E[c_n x[n]] \\ E[x[n]] \end{pmatrix} \quad (2.27)$$

And then, finally

$$\begin{pmatrix} A \\ B \\ C \end{pmatrix} = \begin{pmatrix} E[s_n^2] & E[c_n s_n] & E[s_n] \\ E[c_n s_n] & E[c_n^2] & E[c_n] \\ E[s_n] & E[c_n] & 1 \end{pmatrix}^{-1} \cdot \begin{pmatrix} E[s_n x[n]] \\ E[c_n x[n]] \\ E[x[n]] \end{pmatrix} \quad (2.28)$$

where, under our hypothesis, the terms of the matrix can be written as

$$\frac{1}{N} \sum_{n=0}^{N-1} s_n^2, \frac{1}{N} \sum_{n=0}^{N-1} s_n c_n, \dots \quad (2.29)$$

It could be interesting to estimate the Cramer-Rao bound, i.e. the minimum variance of any unbiased estimator of the unknowns, we have to estimate the Fisher matrix.

Assuming that $x[n]$ are gaussian distributions, we can define the N-dimensional conditional probability density function as

$$p(\mathbf{x}_n, \theta) = \frac{1}{\sqrt{(2\pi\sigma_b^2)^N}} \exp(x[n] - (As_n + Bc_n + C)) \quad (2.30)$$

and then retrieve the Fisher matrix as

$$I(\theta) = \begin{pmatrix} -E \left[\frac{\partial^2 \log(p(\mathbf{x};\theta)}{\partial A^2} \right] & -E \left[\frac{\partial^2 \log(p(\mathbf{x};\theta)}{\partial A \partial B} \right] & -E \left[\frac{\partial^2 \log(p(\mathbf{x};\theta)}{\partial A \partial C} \right] \\ -E \left[\frac{\partial^2 \log(p(\mathbf{x};\theta)}{\partial B \partial A} \right] & -E \left[\frac{\partial^2 \log(p(\mathbf{x};\theta)}{\partial B^2} \right] & -E \left[\frac{\partial^2 \log(p(\mathbf{x};\theta)}{\partial B \partial C} \right] \\ -E \left[\frac{\partial^2 \log(p(\mathbf{x};\theta)}{\partial C \partial A} \right] & -E \left[\frac{\partial^2 \log(p(\mathbf{x};\theta)}{\partial C \partial B} \right] & -E \left[\frac{\partial^2 \log(p(\mathbf{x};\theta)}{\partial C^2} \right] \end{pmatrix} = \quad (2.31)$$

$$= \begin{pmatrix} \frac{1}{\sigma_b^2} \sum_{n=0}^{N-1} s_n^2 & \frac{1}{\sigma_b^2} \sum_{n=0}^{N-1} s_n c_n & \frac{1}{\sigma_b^2} \sum_{n=0}^{N-1} s_n \\ \frac{1}{\sigma_b^2} \sum_{n=0}^{N-1} s_n c_n & \frac{1}{\sigma_b^2} \sum_{n=0}^{N-1} c_n^2 & \frac{1}{\sigma_b^2} \sum_{n=0}^{N-1} c_n \\ \frac{1}{\sigma_b^2} \sum_{n=0}^{N-1} s_n & \frac{1}{\sigma_b^2} \sum_{n=0}^{N-1} c_n & \frac{N}{\sigma_b^2} \end{pmatrix}$$

which equals the first left hand side matrix calculated in Eq. 2.28 times the multiplicative factor $\frac{N}{\sigma_b^2}$. Taking as example the approximated case of zero extra-diagonal terms (i.e. ϕ_n

uniform in the cycle $[0, 2\pi]$), by noting that $\sin^2(x) = \frac{1-2\cos(x)}{2}$, $\cos^2(x) = \frac{1+2\cos(x)}{2}$, the inverse of the Fisher matrix assumes the form

$$I^{-1}(\theta) \approx \begin{pmatrix} \frac{2N}{\sigma_b^2} & 0 & 0 \\ 0 & \frac{2N}{\sigma_b^2} & 0 \\ 0 & 0 & \frac{N}{\sigma_b^2} \end{pmatrix} \quad (2.32)$$

which translates that the θ variance limits will be

$$\text{Var}(A) \geq \frac{2\sigma_b^2}{N}, \text{Var}(B) \geq \frac{2\sigma_b^2}{N}, \text{Var}(C) \geq \frac{\sigma_b^2}{N} \quad (2.33)$$

2.4 Conclusions

In this section, the test rig was presented, together with the experimental techniques adopted. A waveguide was conceived in order to conduct acoustic measurements in the linear regime up to 4300 Hz. Furthermore, the duct ends were equipped with anechoic terminations, in order to reduce end reflections and therefore eliminate any feedback loop behaviours and allow high precision measurements. Also, the test section was made with a glass lateral wall, in order to allow optical and acoustic measurements to be carried out at the same boundary conditions.

Regarding the measurement techniques, mainly Transmission-Reflection acoustic measurement and Laser Doppler Measurements were performed. The former are obtained by the means of two groups (of 4 microphones each) put before and after the test section. By knowing the relative positions of these microphones, their measurements can be used to determine the scattering matrix of the acoustic waves incoming and outgoing from the test section. To do this, two states of the system are needed, which were obtained by switching the acoustic source in an upstream and downstream position.

The optical measurement were taken out by means of a laser technique: scattering particles going through the fringe patterns created by these laser beams will generate a Doppler shift

which, when measured, will indicate their total velocity. As shown in the previous section, from this measured velocity, the coherent velocity was isolated with a least square approach with an error inversely proportional to the number of scattered velocity samples.

Chapter Three

Linear investigation of sound-flow interaction along a corrugated plate

3.1 Introduction

Corrugations are a technological solution used to meet the needs for strength and flexibility of pipes in industrial applications (e.g. gas extraction). However, intense whistling can occur in these pipes, which can lead to fatigue-related failures and noise disturbances [25, 26]. The first investigations on corrugated tubes focused on the whistling behaviour in order to identify the main parameters underneath. The driving mechanism inducing whistling is a feedback-loop between two systems, a fluid-dynamic and an acoustic one. The free shear layer past a cavity is unstable: an instability could create a feedback loop when it encounters the trailing edge of the cavity. In this case, it will self sustain and behave as a sound amplifier. When the natural frequency of this amplifier is close to one of the acoustic resonance frequencies of the corrugated tube, then an energy transfer is possible and a feedback loop is created (see for example [27, 28, 29] and Figure 3.1 for a schematic image where f_v is a general feedback frequency). Specifically, the acoustic system act as a filter, as the standing wave resonance frequencies are discrete, amplification can be obtained around these discrete points. It is possible to identify a linear and a nonlinear amplification regime.

The latter is characterised by large and discrete vortex structures that can produce whistling and the acoustic power grows linearly with the amplitude of the hydrodynamic perturbations. In the linear regime, on the other hand, vorticity is at a smaller scale, while the acoustic power grows quadratically with hydrodynamic perturbations amplitudes. Recent literature has focused mainly on whistling and the nonlinear regime, in order to characterise this striking effect, both from an experimental and numerical point of view. In [30], the amplification characteristic Strouhal numbers were identified, as well as the saturation mechanism of the perturbation velocity which separates linear and nonlinear behaviours. Several other works [31, 32, 33] investigated the details of corrugated walls and side cavity branches in their similarities and differences. In all these works, a detailed analysis of the literature focused on the nonlinear regime can be found. In the case of moderate to high amplitude perturbations the shear layer vorticity concentrates into discrete vortices shed at the upstream edge of the cavity. To model this behaviour a Discrete Vortex (DV) model has been developed [34, 35, 36]. One of the first application is shown in [37], where a single vortex is shed everytime the acoustic velocity changes its direction inward/outward the cavity. This vortex then moves at constant velocity along the cavity width. In this model, the vortex convective speed is an empirical parameter of the problem and therefore also the Strouhal number. In a different approach [38], vorticity can be thought as distributed along an infinitely small shear layer in a Continuous Vortex (CV) model: the distributed vorticity eliminates the vortex singularity at the upstream edge of the cavity. In [39], this model improves the estimations of the acoustic power when compared with the results from [36]. However, also in this case, the length of the vorticity strip is inherently an empirical parameter to be fitted.

Regarding the linear regime, on the other hands, literature lacks both experimental and theoretical results. Experimental data of the linear aeroacoustic field in the linear regime are scarce (e.g. [40]) and they give mainly a global analysis of the aeroacoustic interaction. Theoretical works based on the stability theory from [41] tried to assess the shear layer perturbation due to the acoustic forcing but failed in explaining fundamental effects. Others,

like in [42], used an infinitely small shear layer whose vertical displacement represents the driving mechanism for the cavity oscillations due to the Kelvin-Helmholtz instability. In all cases, the difference w.r.t. experimental data remains large.

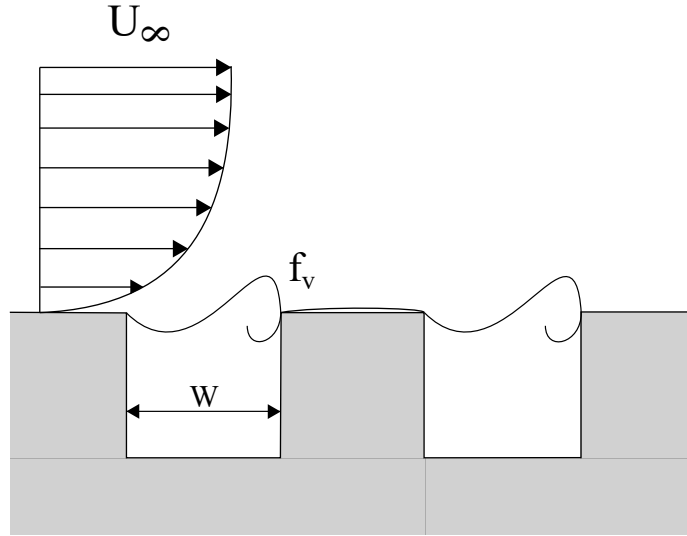


Figure 3.1 – *Schematic view of the impinging mechanism along a corrugated surface.*

Therefore, the main target of the present study is to retrieve, by means of Laser Doppler Velocimetry (LDV), the aeroacoustic field inside a single cavity of a corrugated plate operating in a linear regime and check whether the aforementioned models remain applicable. For this reason, a configuration with small cavities and small amplitude perturbations have been chosen in a non-whistling case. In sections 3.2.1 and 3.2.2, the experimental rig and the investigated corrugated plates are introduced. The acoustic and optical results, as well as the retrieved acoustic power, are presented in section 3.3.

All LDV and acoustic measurements can be found at [43].

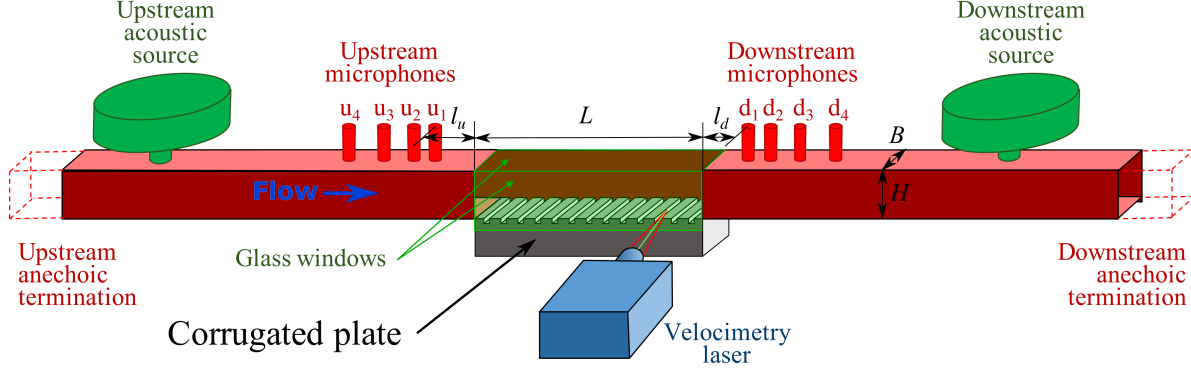


Figure 3.2 – Schematic view of the experimental setup.

3.2 Experimental Setup

3.2.1 Test Rig

The test rig is a uniform rectangular duct whose section is $B = 50 \text{ mm} \times H = 40 \text{ mm}$ and has been described in details in Section 2.2. Here, it has been quickly described and shown in Fig. 3.2. In this duct, the flow velocity is measured by a Pitot tube (diameter 2.1 mm) in the center of the rectangular duct and by Laser Doppler Velocimetry (LDV).

3.2.2 Corrugated Walls

The studied corrugated plate is shown in Figure 3.3-b. It is a 200 mm long anodized plate characterized by an array of 16 cavities: each cavity measures $4 \times 4 \times 50 \text{ mm}^3$ (covering the entire transverse span $B = 50 \text{ mm}$ of the duct), has square and sharp edges on both sides and is separated by a 12 mm pitch. The cavity investigated is the third from the end of the plate (w.r.t. the flow direction) because here the boundary layer is fully developed.

To have a phase reference, the horizontal periodic velocity u'_{ref} was measured away from the corrugations in the central part of the duct (reference box on Figure 3.4-a). Indeed, in the central part of the duct, it is possible to consider that the hydrodynamic disturbances are low and that the horizontal periodic velocity is only due to the acoustics. Thus, the value of

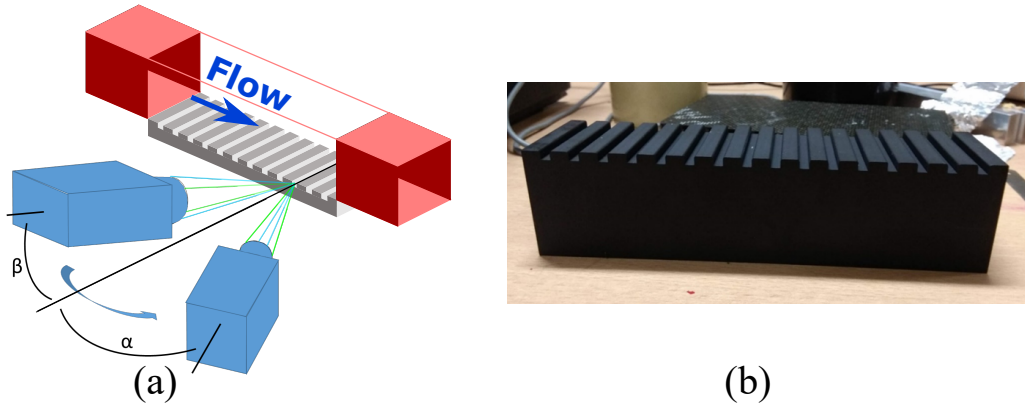


Figure 3.3 – (a) Schematic view (not at scale) of the optical experimental setup and (b) picture of the investigated corrugated plate.

the horizontal acoustic velocity (averaged over the reference box) was taken as a reference for the amplitude of the incident acoustic wave and, more importantly, as a phase reference that does not depend on the acoustic path between the source and the measurement position. Therefore, all phase values presented in the following are taken relative to this reference.

3.2.3 Mean Flow in the Setup

In this section, we look at the mean quantities associated to the flow. Figure 3.5-a,b and figure 3.5-d,e display the mean horizontal and vertical velocity contours when the upstream source position is working at 1400 Hz and 2000 Hz. We can see that the velocity field is well resolved and there is no major difference between the two measurements in the mean velocity distribution. This is further confirmed in figure 3.5-c, where the horizontal velocity is shown along the vertical lines indicated in plain and filled symbols, which correspond to the lines for $x = 0, W/3, 2W/3, W$. We can see that the curves are similar for the two frequencies and that, outside the cavity, the velocity profile of the shear layer doesn't change with the longitudinal position. Equally important is to notice from the streamlines in figures 3.5-d, that this shear layer is layed out above a recirculation zone, regardless of the frequency case. In figure 3.6-c, the velocity profiles along the vertical lines at $x = 0, W/3, 2W/3$ for the

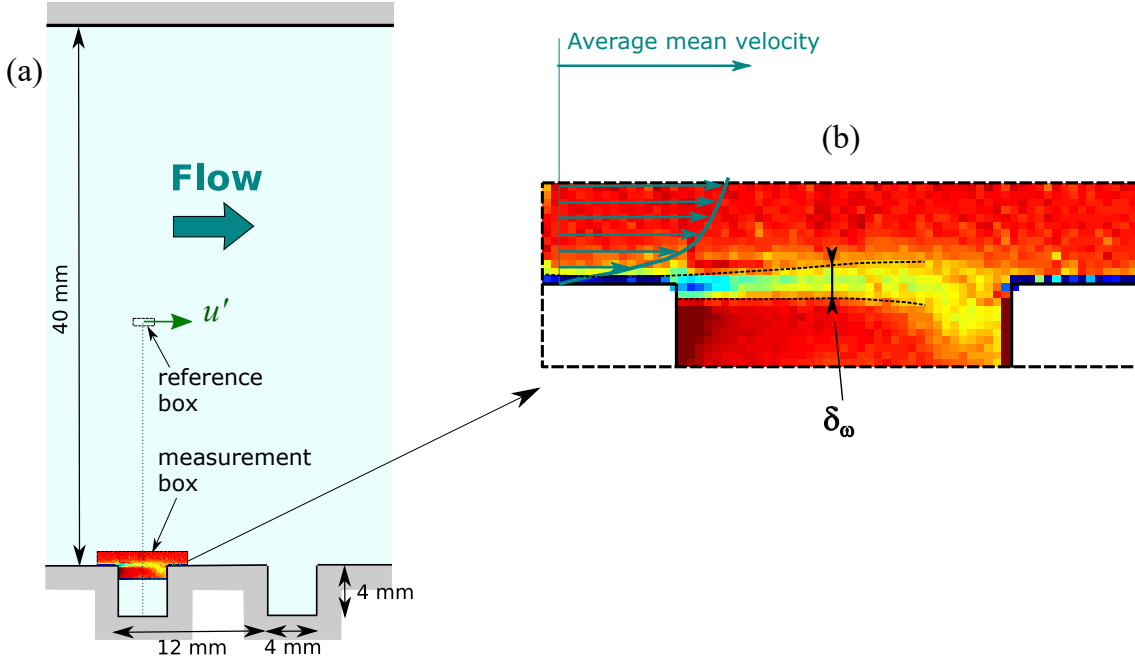


Figure 3.4 – (a) Position of the measurement box and of the reference box. (b) Values of the mean vorticity for $M_\infty = 0.07$.

2000 Hz case, are again shown, from inside the cavity up to the centerline of the channel. In this case, the velocity profiles are shown in the so called wall coordinates $y^+ = y\nu/U_\tau$ and $u^+ = U_0/U_\tau$, where ν is the dynamic viscosity of the air and U_τ is the friction velocity defined through the shear stress $\tau = \mu dU_0/dy|_w$ at the wall as $U_\tau = \sqrt{\tau}/\rho$. This velocity was obtained from the slope of the velocity inside the logarithmic layer [44, 45] and its value is found to be 1.01ms^{-1} . Two layers are then identified: the above mentioned logarithmic layer, closer to the wall, and an external core layer, where the viscosity due to the turbulence ν_t is supposed to be constant. In the first, a velocity profile of the kind

$$u^+ = \frac{1}{K} \ln \left(\frac{1}{K} + y^+ \right) + 5.5 \quad (3.1)$$

is obtained, while for the core layer, a parabolic profile is retrieved

$$\frac{U_\infty - U_0}{U_\tau} = \frac{HU_\tau}{2\nu_t} \left(1 - \frac{y}{H} \right)^2 \quad (3.2)$$

where H is the channel half-height and K is the von Karman constant, $K = 0.41$. These two layers match around $y^+ = 120$ (i.e. $y \approx 2$ mm) while a viscosity $\nu_t = 8.02 \cdot 10^{-4} \text{ m}^2\text{s}^{-1}$ is retrieved. In figure 3.6-b, a cavity close-up of the horizontal mean velocity U_0 along the same three lines is shown. The boundary layer outside the cavity seems to remain unchanged along the cavity length (for $y > 0.2$ mm), while this is not true for the shear layer inside the cavity itself. Inside the cavity, the velocity changes until it reaches an almost steady value. Then, we can define the thickness of the shear layer as the distance between these two points. For the $x = 0$ position, this is roughly 0.6 mm, while for the $x = 2W/3$ mm this grows up to 1 mm.

3.2.4 Acoustic velocity Modeling

As shown later in section 3.4, in the present configuration, the acoustic power can be described by the Howe analogy, which basically accounts for the interaction between a Coriolis force (i.e. the $-\rho_0(\boldsymbol{\omega} \times \mathbf{u})$ term, where \mathbf{u} and $\boldsymbol{\omega}$ are the total velocity and vorticity vectors, respectively, and ρ_0 the density of the fluid). As from the measurements it is not feasible to extract only the acoustic potential velocity component, it is necessary to obtain it through modelling. There are several ways of solving the compressible flow field, but a rather simple way was to use the commercial code COMSOL. To retrieve the acoustic velocity in quiescent conditions (as the Mach number considered is very small), the ACPR Module was used, which solves the acoustic pressure propagation in the frequency domain.

In figure 3.7 we can observe the potential flowfield obtained for a single cavity: the net flow entering in the cavity is zero and the minimum and maximum velocity values appear at the leading and trailing edge, respectively. Since this is a potential flow, the velocity \mathbf{u}_s in all points of the domain is defined w.r.t. a reference (i.e. a boundary condition) value. Therefore, we need to scale the simulated velocity to the actual velocity field at a reference "free stream" position (i.e. the "reference box" indicated in figure 3.7). At this position, the

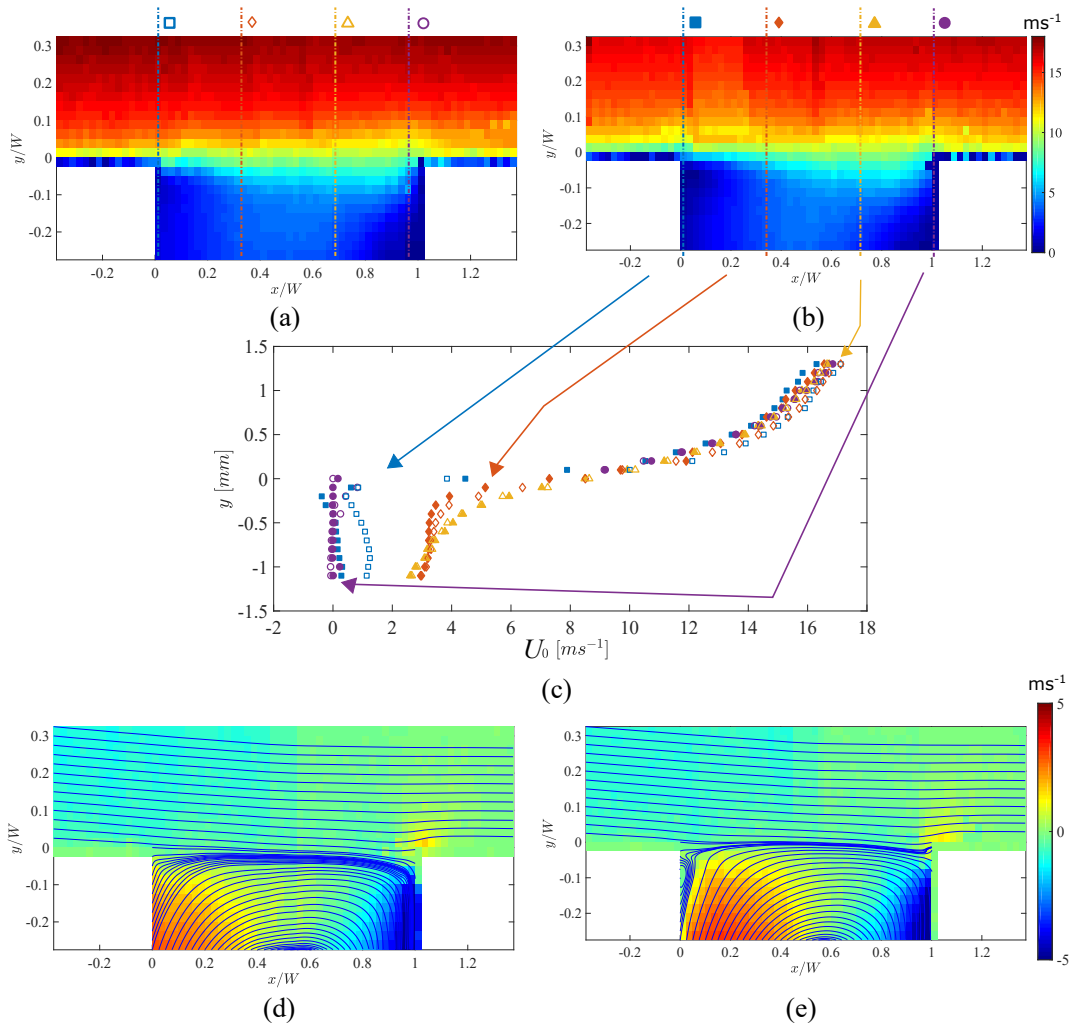


Figure 3.5 – Horizontal mean velocity for the upstream source case at (a) 1400 Hz and (b) 2000 Hz. In (c) the velocity close to the cavity is shown along the vertical lines as indicated in the (a-b) figures. The plain and filled symbols represent the 1400 and 2000 Hz case, respectively. The vertical mean velocity has been shown for the (d) 1400 and (e) 2000 Hz cases, together with streamlines.

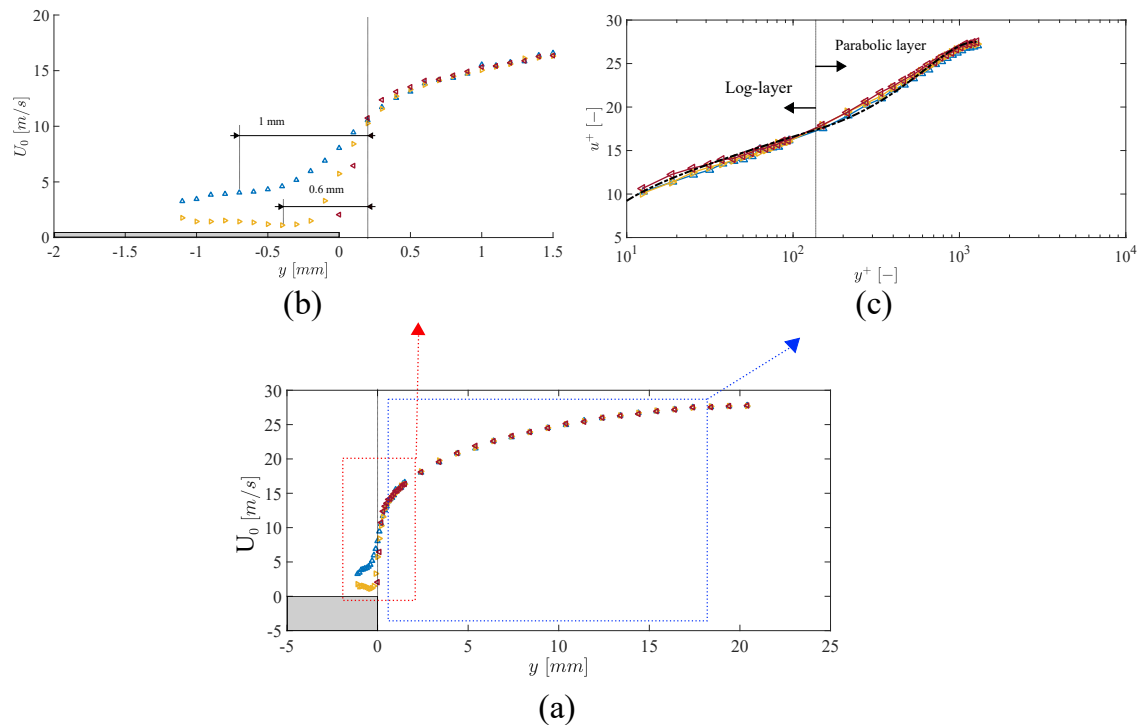


Figure 3.6 – Horizontal mean velocity for the 2000 Hz upstream source case (a).

The velocity is shown along three vertical lines corresponding to the $x = 0, 1/3W, 2/3W$ horizontal positions, to which the \triangleleft , \triangleright , \triangle symbols corresponds. In (b) a zoomed figure of the same velocities inside the cavity is shown, while in (c) the analytical curves are plotted together with the experimental ones in wall coordinates.

measured horizontal coherent velocity component is the actual acoustic velocity.

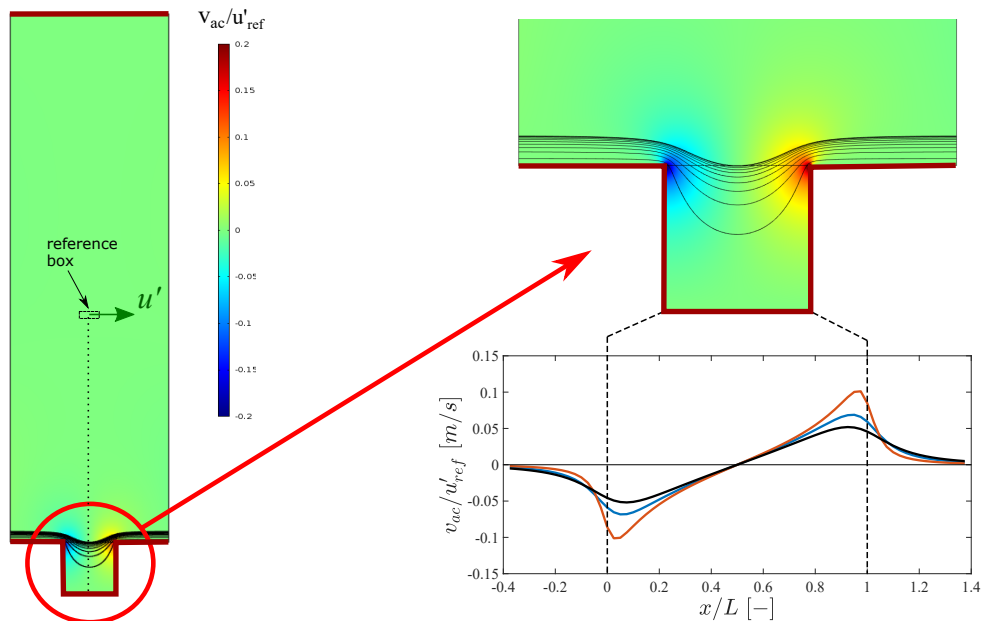


Figure 3.7 – Potential velocity field contour as obtained from the COMSOL simulation. The reference box indicates where the reference velocity was calculated. The zoomed-in contour shows the velocity field close to the cavity while the underlying plot shows the potential velocity along three horizontal lines above the cavity lid.

3.3 Results

3.3.1 Acoustic measurements

The corrugated plate is first characterised by acoustic measurements. Using the 2×4 microphones placed on each side of the plate, the transmission and reflection coefficients are measured with and without flow. The magnitudes of the transmission coefficients (along/against the flow, T^+ and T^- respectively) are given in figure 3.8.

In the no-flow case, due to reciprocity, T^+ and T^- are quite identical and the differences between both curves are only due to measurement errors (limited to 0.5%). The deviation to 1 of these curves indicates that visco-thermal losses are present along the walls of the duct corrugated on one of its faces.

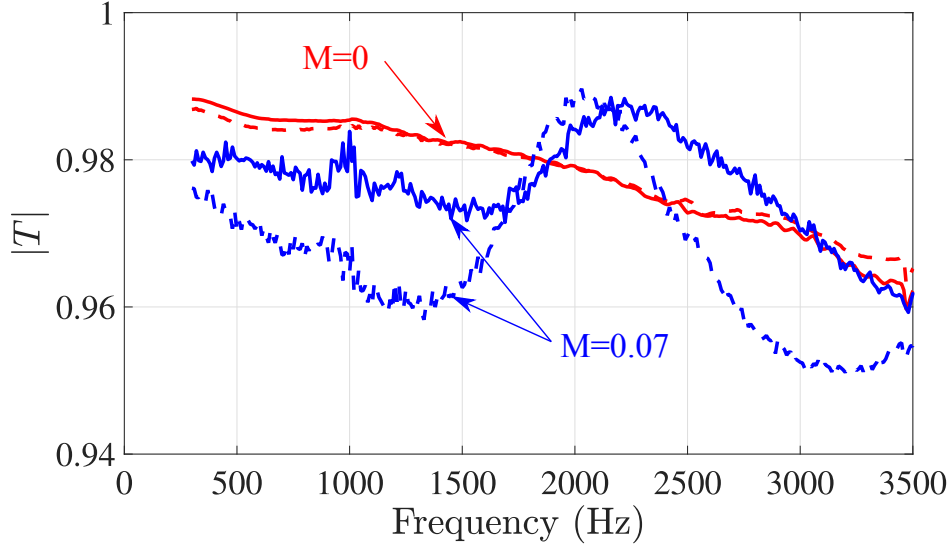


Figure 3.8 – Absolute value of experimental transmission coefficients without flow and with flow ($M = 0.07$). The continuous lines represent $|T^+|$ and the dashed lines $|T^-|$.

When the flow is present, several observations can be made. First, the $|T^+|$ and $|T^-|$ curves are no longer the same, meaning that reciprocity is lost. Secondly, it can be noted that the transmission curves oscillate around the no-flow value. At low frequencies ($f < 1800$ Hz), the attenuation with flow is greater than in the no-flow case. Then, over a specific frequency range ($1880 \text{ Hz} < f < 3100 \text{ Hz}$ for T^+ and $1820 \text{ Hz} < f < 2400 \text{ Hz}$ for T^-), the flow reduces the attenuation. This kind of behavior has already been observed in cylindrical corrugated pipes [40] as well as in the effect of flow on a rectangular slot in a wall [46]. The last point to note is that the transmission coefficients always remain below unity. This means that the acoustic losses due to visco-thermal effects are not compensated by hydrodynamic effects. As a result, and contrary to what would happen with a cylindrical corrugated pipe with similar cavities [40], this plate cannot start a whistling process at this flow velocity. This is mainly due to the fact that, unlike a cylindrical pipe where the entire inner surface is corrugated, only the lower quarter of the channel is corrugated here. The Strouhal number at the frequency ($f = 2200 \text{ Hz}$) for which the hydrodynamic amplification is maximum for

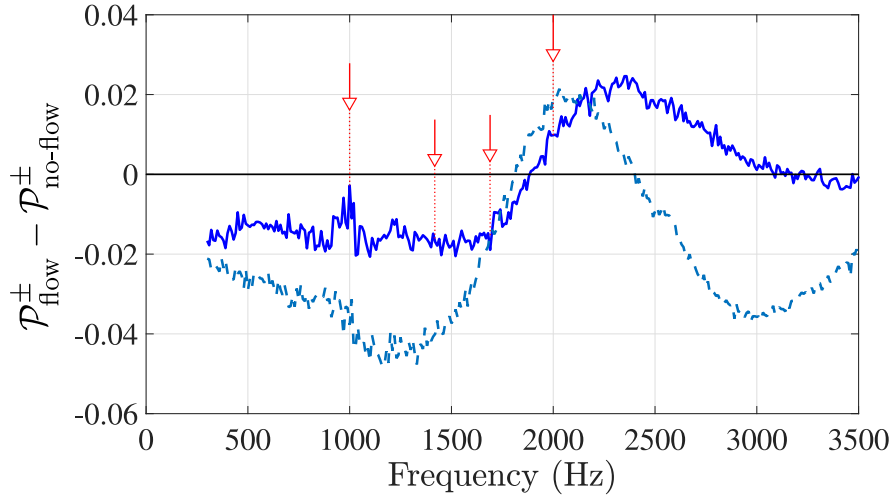


Figure 3.9 – Normalized experimental sound power generated by the grazing flow ($M = 0.07$). The solid line corresponds to the flow with incident sound in the same direction and the dashed lines to the case where waves travel against the flow. The red dashed arrows point out the frequencies at which the LDV measurements were carried out.

T^+ is given by

$$St = \frac{fW}{U_m} = 0.37,$$

where $W = 4$ mm is the cavity width in the flow direction and $U_m = 24$ m.s⁻¹ is the mean velocity of the flow. Since this value is close to that found in cylindrical pipes ($St \simeq 0.4$, [30, 40]), it can be assumed that the same underlying physical phenomenon occurs in the two-dimensional (2D) case and in the cylindrical case.

From the scattering matrix measurement, it is also possible to estimate the sound power produced (or absorbed) at each frequency by the grazing flow. The ratio of the produced sound power to the incident sound power is given by [47]:

$$\mathcal{P}^\pm = |T^\pm|^2 + \frac{(1 \mp M)^2}{(1 \pm M)^2} |R^\pm|^2 - 1. \quad (3.3)$$

The difference between the \mathcal{P}^\pm evaluated with and without flow gives the sound power produced by the flow and normalized by the incident sound power. This is shown in Figure 3.9.

3.3.2 LDV Results

In this section, the interactions between acoustics and hydrodynamics are investigated using LDV. First, it is possible to see in figure 3.10(a) that the periodic velocity field is well resolved with the LDV technique, except, perhaps, in the vicinity of the wall angles where the measurements are slightly under-resolved. Each pixel in the figure 3.10(a) represents a measured value of the vertical periodic velocity $v'/|u'_{\text{ref}}|$. The measured coherent velocities have been nondimensionalised with the respective horizontal coherent velocity at the reference position u_{ref} in order to have a proper comparison between the sets of measurements.

The periodic field is characterized by very clear structures that move horizontally at the cavity lid. Figure 3.10(b,c) gives the amplitude and the phase of the periodic vertical velocity, respectively, along the cavity which is represented for six horizontal lines corresponding to the axis $y = 0, 0.1 \dots 0.5$ mm ($y = 0$ mm is the surface of the plate). The slope of the phase indicates the convection velocity of the structures. In this particular case, the variation of the phase is nearly linear, indicating a constant convection velocity given by the slope of the straight line. Surprisingly, the maximum amplitude of v' is rather constant over the length of the cavity as can be seen in figure 3.10(b). In general, an exponential increase of the disturbance is expected, whereas here there is only a slight increase over the length of the cavity. In figure 3.11, the horizontal coherent velocity is shown. Here, the coherent structures are more elongated in the horizontal direction and their amplitude decreases when arriving close the trailing edge of the cavity due to the presence of the wall.

The coherent vorticity $\omega' = \partial_y u' - \partial_x v'$, nondimensionalised by the reference vorticity $\omega_{\text{ref}} = |u_{\text{ref}}|/W$, is depicted in Figure 3.12. This vorticity is computed using the central difference for inner data points and using one-sided differences for the edges of the domain. The periodic vorticity is tightly packed at the leading edge of the cavity (w.r.t. the trailing edge) and the phase has the same linear variation as the vertical velocity. Then, in this linear regime, the measured structures are associated with a vortical hydrodynamic perturbation

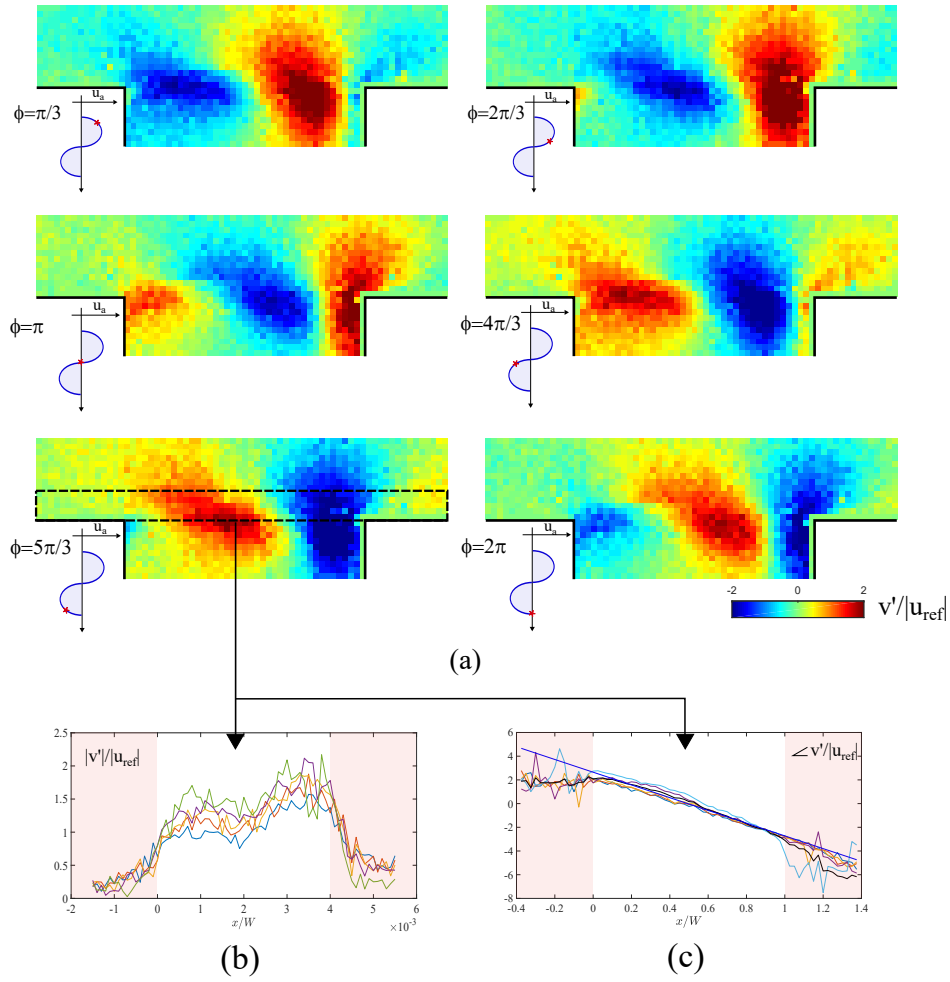


Figure 3.10 – Normalized vertical periodic velocity $v'/|u'_{ref}|$ colormaps (a) at different relative phases: $\phi_s = \pi/3, 2\pi/3 \dots 2\pi$ for the upstream 2000 Hz source position and $M = 0.07$. Vertical periodic velocity amplitude (b) and phase (c) along the six horizontal lines corresponding to $y = 0, 0.1, \dots, 0.5$ mm. The thick black line in (c) is the average over the six values and the blue straight line is a linear fit.

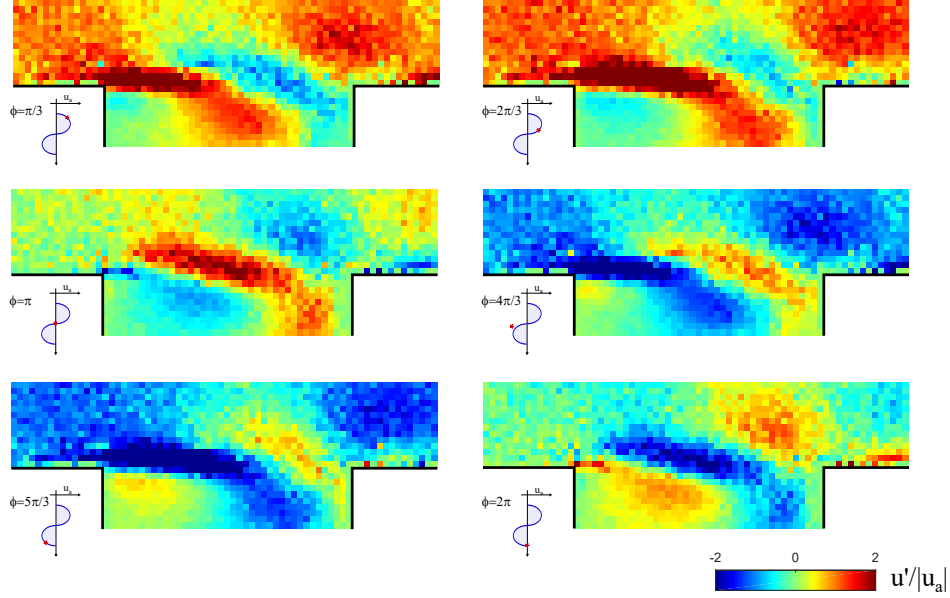


Figure 3.11 – *Normalized horizontal periodic velocity $u'/|u_{ref}'|$ colormaps at different relative phases: $\phi_s = \pi/3, 2\pi/3 \dots 2\pi$ for the upstream 2000 Hz source position and $M = 0.07$*

at the leading edge of the cavity. However, periodic vorticity cannot be considered to be concentrated on an infinitely thin line nor at a point. Thus, none of the simplest models, i.e. shear layer oscillations that increase exponentially with distance from the upstream edge [48, 49] or shear layer oscillations that break down into discrete vortices [36], can be applied here. This is due to the finite thickness of the mean shear layer with respect to the size of the cavity [37].

Furthermore, from figure 3.13, we can see that the vorticity structure is composed of counter-rotating vorticity zones tightly packed. At the leading edge, the vorticity is governed by the term $-\partial u'/\partial y$, while, at the trailing edge, it is the term $\partial v'/\partial x$ which prevails. This could be expected, as at the leading edge the sudden expansion along y is the dominating effect, while at the trailing edge the hard wall imposes a strong x gradient. At the beginning of the cavity, we can observe counter rotating vorticity zones (almost) stacked on top of each other. This is due to the u' profile shape which is not monotonic: instead, a crest shape can be observed, whose maximum is around $y = 0$ (as shown in figure 3.13-inset). This is due

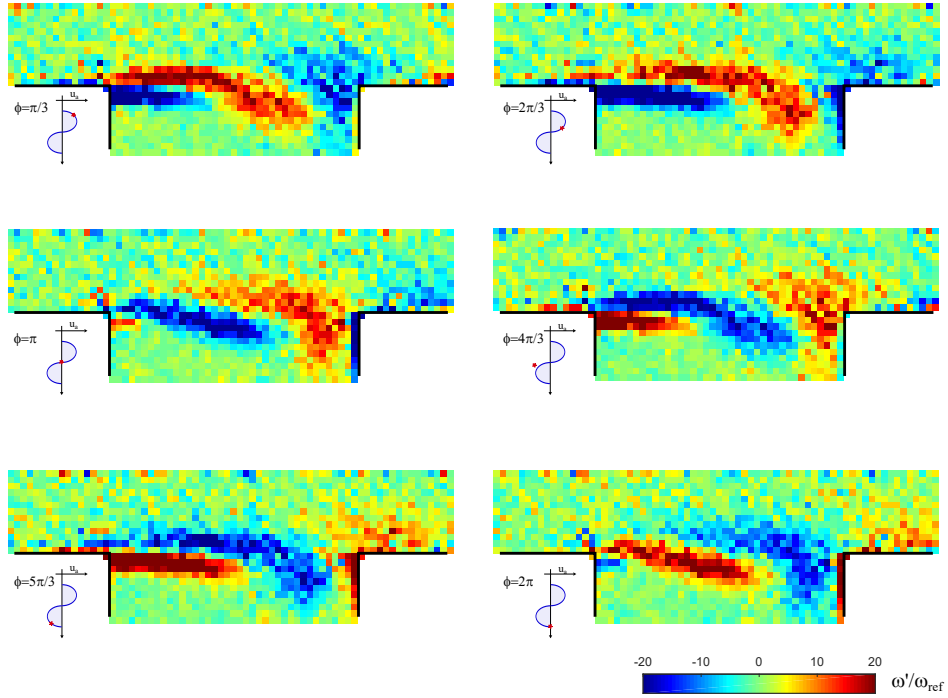


Figure 3.12 – Normalized vorticity ω'/ω'_{ref} colormaps at different relative phases: $\phi_s = \pi/3, 2\pi/3 \dots 2\pi$ for the upstream 2000 Hz source position and $M = 0.07$.

to the interaction between the potential acoustic velocity (which would be infinite at the sharp edge) and the hydrodynamic velocity through the Kutta condition. Therefore, when u' is positive, this translates in a positive vorticity area on top of a negative one. Near the trailing edge, instead, the vorticity distribution ω' is similar to the v' distribution (as here the term $\partial v'/\partial x$ dominates), where wider opposite sign zones follow each other.

To test the linearity hypothesis, the corrugated plate was exposed to two different sound levels, while keeping all other parameters constant. By decreasing the voltage supplied to the source, the horizontal sound velocity in the reference box u'_{ref} was reduced from 0.56 m.s⁻¹ to 0.24 m.s⁻¹ (7.5 dB decrease, see table 3.1). The colormaps of the vertical periodic velocity normalized by u'_{ref} are presented in figure 3.14. Despite some minor differences, the normalized velocities are globally similar, which indicates the linearity of the studied phenomena. It should be noted that in the case of lower amplitudes, the signal-to-noise ratio is lower, which leads to less accurate and more difficult measurements.

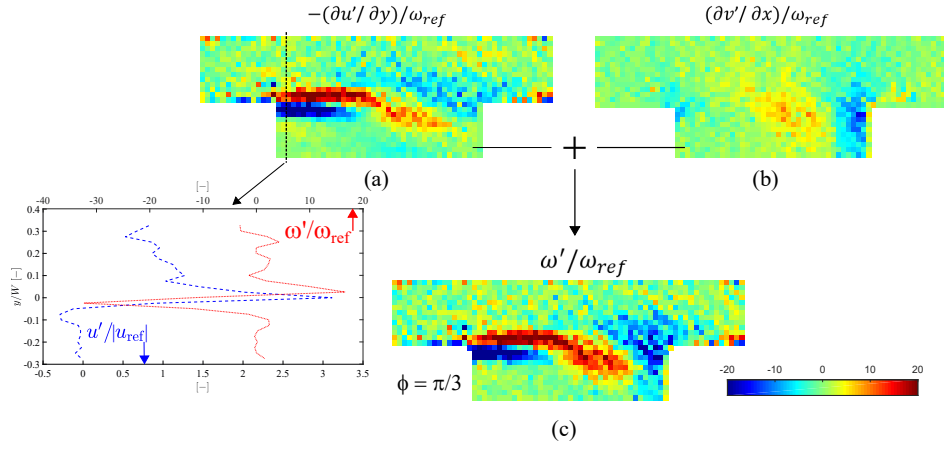


Figure 3.13 – Normalized vorticities (a) $-(\partial u' / \partial y) / \omega_{ref}$, (b) $(\partial v' / \partial x) / \omega_{ref}$ and (c) their sum ω' / ω_{ref} colormaps at $\phi = 0$ for the upstream 2000 Hz source position and $M = 0.07$ case. The inset indicates the horizontal $u' / |u_{ref}|$ velocities and vorticity ω' / ω_{ref} along the $x = 0$ line.

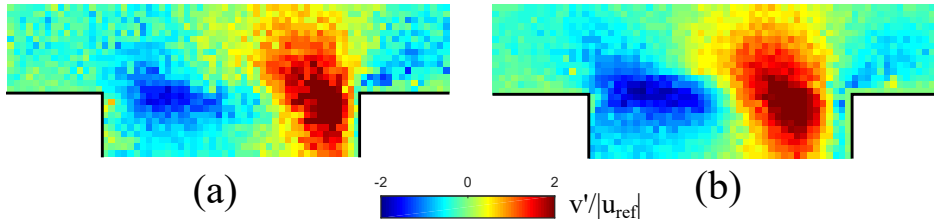


Figure 3.14 – Nondimensionalized vertical periodic velocity colormaps for the (a) low and (b) high amplitude acoustic source cases at $\phi_s = \pi/3$.

Frequency	Source Position	Sound Level
$f = 1000$ Hz	Upstream	140 dB
$f = 1400$ Hz	Upstream	140 dB
	Downstream	140 dB
$f = 1700$ Hz	Upstream	140 dB
$f = 2000$ Hz	Upstream	140 dB
	Upstream (low amp)	132.5 dB
	Downstream	140 dB

Table 3.1 – *LDV measurement configurations*

In the following subsections, different setup configurations have been studied as shown in the table 3.1. These configurations have been chosen in order to investigate the effects of the position of the sound source (w.r.t. the direction of the mean flow) and its frequency. Also, a separate subsection is devoted to the discussion of the convective velocity of aeroacoustic structures.

Frequency effects

In this section, we analyze the corrugated plate for two different values of the source frequency: 1400 and 2000 Hz. These two configurations are detailed in Table 3.1 and the only difference is the source frequency: the value of 2000 Hz corresponds to a (nearly) maximum produced acoustic power (w.r.t the baseline no-flow case), while the 1400 Hz corresponds to an absorbed one. From Figure 3.15, it is possible to appreciate how frequency difference

creates a different relative position of the maxima and minima in the velocity field, for the $f = 2000$ and 1400 Hz upstream source cases. Furthermore, we can see that in the 2000 Hz case, a third positive velocity area appears at the trailing edge of the cavity. It is important to outline that the velocity distribution is directly responsible for acoustic production, as shown in the later Section 3.4. These structures are characterised by a wavelength λ_i which is given by

$$\lambda_i = \frac{U_c}{f_s} \quad (3.4)$$

where f_s is the source frequency and U_c is the velocity at which such structures are convected downstream, i.e. the convective velocity. For the 1400 Hz case (3.15-a), this length is $\lambda_1/2 \approx 2.7$ mm while for the 2000 Hz case (3.15-b) the length is $\lambda_2/2 \approx 2.2$ mm. On the other hand, the ratio between the lengths λ_1 and λ_2 is not exactly equal to the inverse of the frequency ratio, as one might expect: while the ratio of lengths is ≈ 1.23 , the inverse ratio of frequency is ≈ 1.43 suggesting that the velocity of propagation of disturbances is a function of frequency. This is shown in figure 3.16, where the vertical coherent velocity phases have been traced along the cavity. As this slope is directly linked to the convective velocity through the acoustic frequency as

$$U_c = \frac{2\pi f_s W}{|\Delta\phi/W|} \quad (3.5)$$

where now $|\Delta\phi/W|$ is the phase slope, we can see that the convective velocity grows with the signal frequency at most 16%. This result challenges the common assumption, when modeling the shear layer amplification in the linear regime, that this velocity is constant.

Acoustic Source Position Effect

In this paragraph, we are interested in analysing the effect of the of the relative direction of propagation between the acoustic wave and the flow. The main discrepancy introduced by the different propagation direction of the acoustic wave is a phase difference. As the measure-

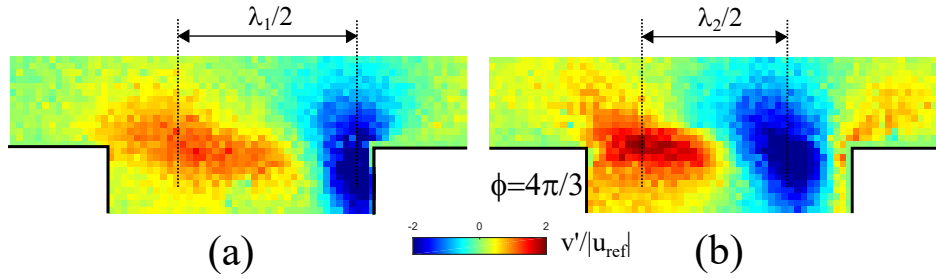


Figure 3.15 – Vertical periodic velocity (Real part) colormaps for the $f_s = 1400$ (a), 2000 (b) Hz upstream cases, $\phi = 4/3\pi$

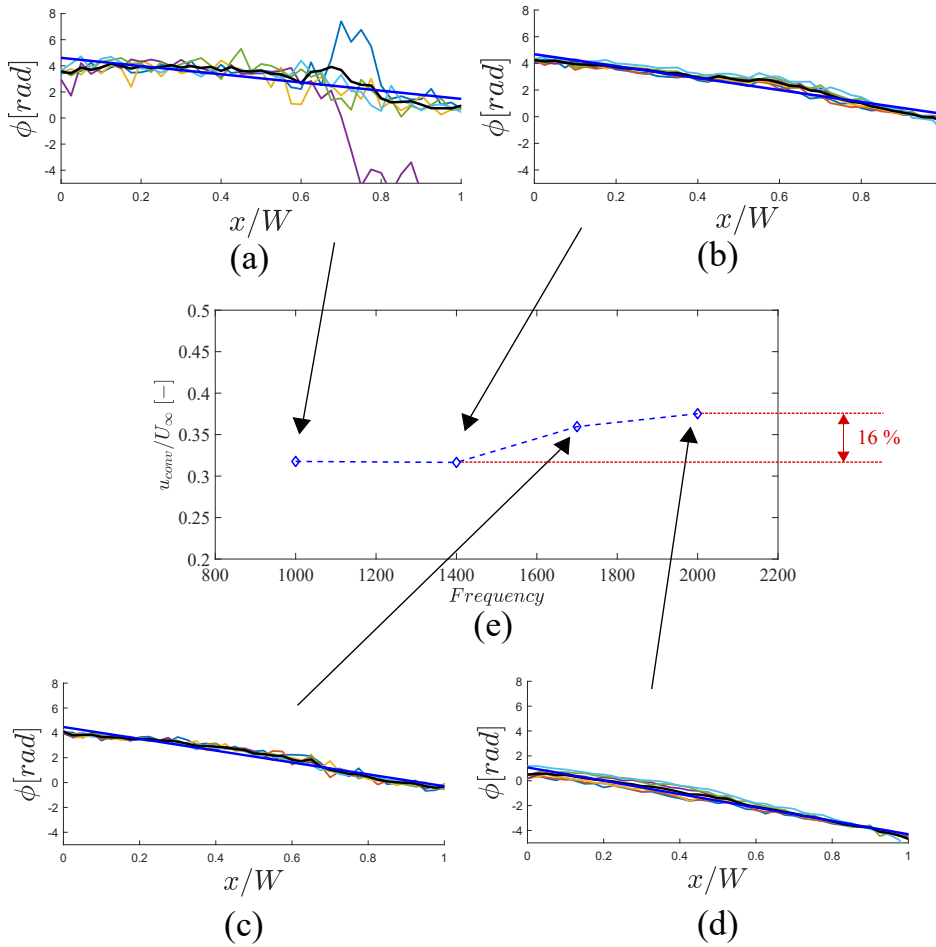


Figure 3.16 – Vertical periodic velocity phases (a-d) along the six horizontal lines corresponding to $y = 0, 0.1, \dots, 0.5$ mm for the $f_s = 1000, 1400, 1700, 2000$ Hz upstream cases. In (e) the convective velocities calculated from the phase slopes for the same four cases are shown.

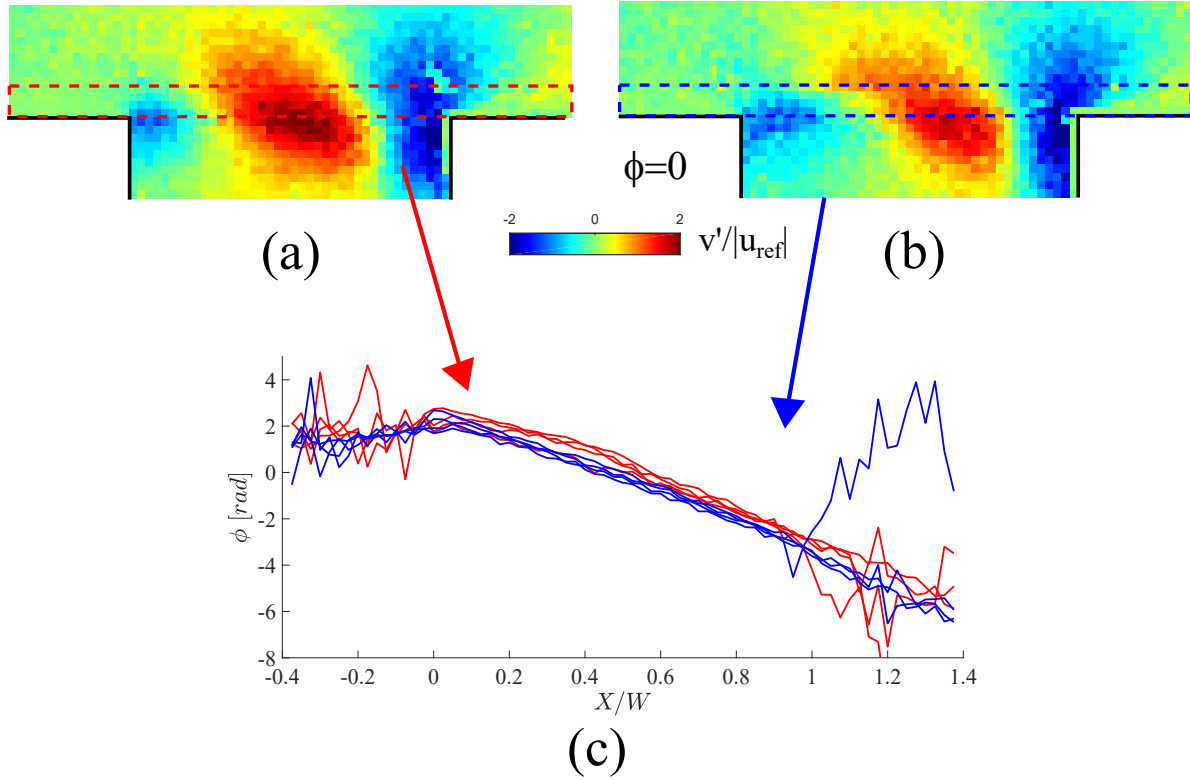


Figure 3.17 – Vertical periodic velocity (Real part) colormaps for the (a) downstream and (b) upstream $f_s = 2000$ Hz cases, $\phi = 0$. In (c) the vertical periodic velocity phases calculated along the corresponding indicated coloured lines are also shown

ments are taken w.r.t. the reference box, we can see that, at the same phase reference, for the downstream case, the velocity structures are lagging behind by a small phase difference. This can be directly seen from the periodic velocity colormaps, as done in the precedent paragraph and shown here in Figure 3.17, which show the vertical periodic velocity for the two cases. It can be seen that the same field structures are retrieved and in the downstream case the cores of these structures are slightly closer to each other (again, from eq. 3.4, we can measure $\lambda_d = 2$ mm for the downstream case while $\lambda_u = 2.2$ mm for the upstream one). The same results, not shown here, have been obtained at the forcing frequency of $f_{ref} = 1400$ Hz.

Leading Edge Shape Effect

The leading edge of the cavity can also have an influence on the velocity field inside the cavity. As shown by [30], this effect can be globally accounted for through some corrective added length, in the calculation of the Strouhal number corresponding to the peaks and valleys of acoustic power curve. In Figure 3.18, the vertical velocity field is shown for two types of leading edges, a rounded edge and the sharp one, for a source frequency of 2000 Hz. It is possible to appreciate that, at the same phase reference, the velocity field is slightly earlier for the rounded edge case. This result is similar, but accentuated, to what has been found by shifting the acoustic source from an upstream position to a downstream one. For this reason, this justifies the acoustic power curve characteristic frequencies towards lower values.

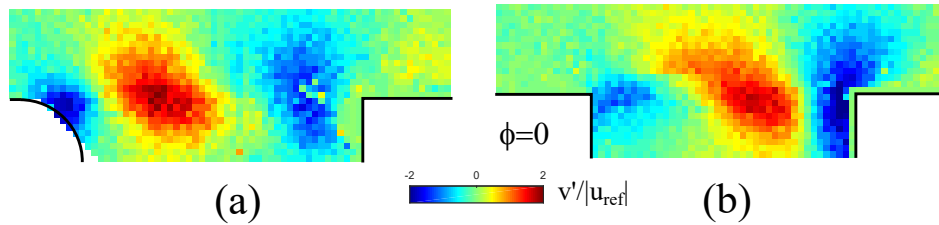


Figure 3.18 – *Acoustic pressure contours for the (a) rounded and (b) square upstream cavity edge at $f = 2000$ Hz and $M=0.07$.*

3.4 Acoustic Power

Considering an homoentropic flow (with the additional constraint of a low Mach number), Howe [50] computed the acoustic power formulation as follows:

$$\langle P_H \rangle = - \int_V \rho_0 \langle (\boldsymbol{\omega} \times \mathbf{u}) \cdot \mathbf{u}_a \rangle dV = \int_V \langle (F_x u_a + F_y v_a) \rangle dV, \quad (3.6)$$

where $\boldsymbol{\omega} = (\Omega_0 + \omega') \cdot \mathbf{z}$, $\mathbf{u} = (U_0 + u') \cdot \mathbf{x} + (V_0 + v') \cdot \mathbf{y}$ and $\mathbf{u}_a = u_a \cdot \mathbf{x} + v_a \cdot \mathbf{y}$ are respectively the total vorticity, the total velocity and the acoustic (i.e. potential) velocity of the flow,

while $\mathbf{F} = F_x \cdot \mathbf{x} + F_y \cdot \mathbf{y} = -\rho_0 (\boldsymbol{\omega} \times \mathbf{u})$ is the Coriolis force vector. The symbol $\langle \rangle$ represents the average over one time period. In the case of complex functions, such average can be directly computed as (e.g. for the first term inside the integral of eq. 3.6) :

$$\langle F_i u_a \rangle = \frac{1}{2} \text{Re} (\bar{F}_i u_a) \quad (3.7)$$

for $i = x, y$ and \bar{F}_i is the complex conjugate of vector F_i .

It is interesting to notice that the vector product $\mathbf{F} = (F_x, F_y) = -\rho_0 (\boldsymbol{\omega} \times \mathbf{u})$ is composed of an horizontal and a vertical Coriolis force term (by unit volume). As explained in section 3.2.4, since the acoustic velocity in Eq. 3.6 cannot be measured directly, a COMSOL frequency domain simulation was carried out to solve the Helmholtz equation. Furthermore, the acoustic power is nondimensionalised w.r.t. a reference power calculated as follows:

$$P_a = \frac{|u_{\text{ref}}|^2 \rho_0 c_0}{2} \quad (3.8)$$

since, in a centerline position, the relationship $p_{\text{inf}}/u_{\text{ref}} = \rho_0 c_0$ is a fair assumption and the periodic horizontal velocity equals the acoustic velocity, i.e. $u_{\text{ref}} \approx u_a$.

It should also be noted that from the vector $\mathbf{F} = -\rho_0 ((\boldsymbol{\Omega}_0 + \boldsymbol{\omega}') \times (\mathbf{U}_0 + \mathbf{u}'))$, when the time average inside eq. 3.6 is carried out, the inner product of the mean values do not contribute, while, at order one, the inner product of the coherent terms can be neglected. Then, each component of the vector \mathbf{F} can be written as

$$F_x = \rho_0 (\omega' V_0 + \Omega_0 v') \quad (3.9)$$

$$F_y = -\rho_0 (\omega' U_0 + \Omega_0 u') \quad (3.10)$$

Therefore, each component of the Coriolis force can be split into two contributions and the total acoustic power will result from their inner product with the acoustic velocity. In other words, the more the Coriolis vector is aligned along the acoustic velocity streamlines, the larger the acoustic production will be. We can then define, in a definitely improper but practical way, an 'horizontal' and 'vertical' acoustic power as the contributions due to

the corresponding horizontal and vertical Coriolis forces. In figure 3.19, these components are shown, time-averaged, for the 2000 Hz upstream source case, together with the total acoustic power distribution. It is interesting to notice that the two contributions inside each component of the Coriolis force are of the same order of magnitude, while, on the other hand, they are not at all similarly distributed. In the following sections we consider the spatial distributions of the four contributions for the $f = 2000$ Hz upstream source case. This frequency corresponds to a net positive normalized sound-power generation.

3.4.1 Acoustic Power $\rho_0(\omega'V_0)u_a$ contribution

The acoustic power generated by the Coriolis component $\rho_0(\omega'V_0)$ is $\rho_0(\omega'V_0)u_a$ and is shown, averaged over one period, in figure 3.19-b. As we can see, this power contribution is very small at all points in the flowfield. By looking at the mean vertical velocity V_0 (see figure 3.5), we can see that this velocity is small (when compared with U_0) and confined inside the cavity, while almost zero elsewhere. At the same time, the coherent vorticity ω' is concentrated inside the shear layer, which is thin along the cavity lid (see figure 3.12). Only near the trailing edge, the vorticity slightly spreads inside the cavity as the shear layer becomes thicker. Then, these terms cannot interact with each other: the Coriolis component $\rho_0(\omega'V_0)$ and, as a consequence, the corresponding acoustic power $\rho_0(\omega'V_0)u_a$, will be very small. These observations would probably still hold when the frequency changes.

3.4.2 Acoustic Power $\rho_0(\Omega_0v')$ contribution

The term $\rho_0(\Omega_0v')$ is the one which gives the global structure to the total horizontal power, as can be observed from Figure 3.19-a,c (time averaged) and Figure 3.20 for $\phi = \pi/3$. In this case, we can identify two distinct absorption and production areas which are isolated from each other. The mean vorticity Ω_0 is shed clockwise (i.e. negative) at the leading edge

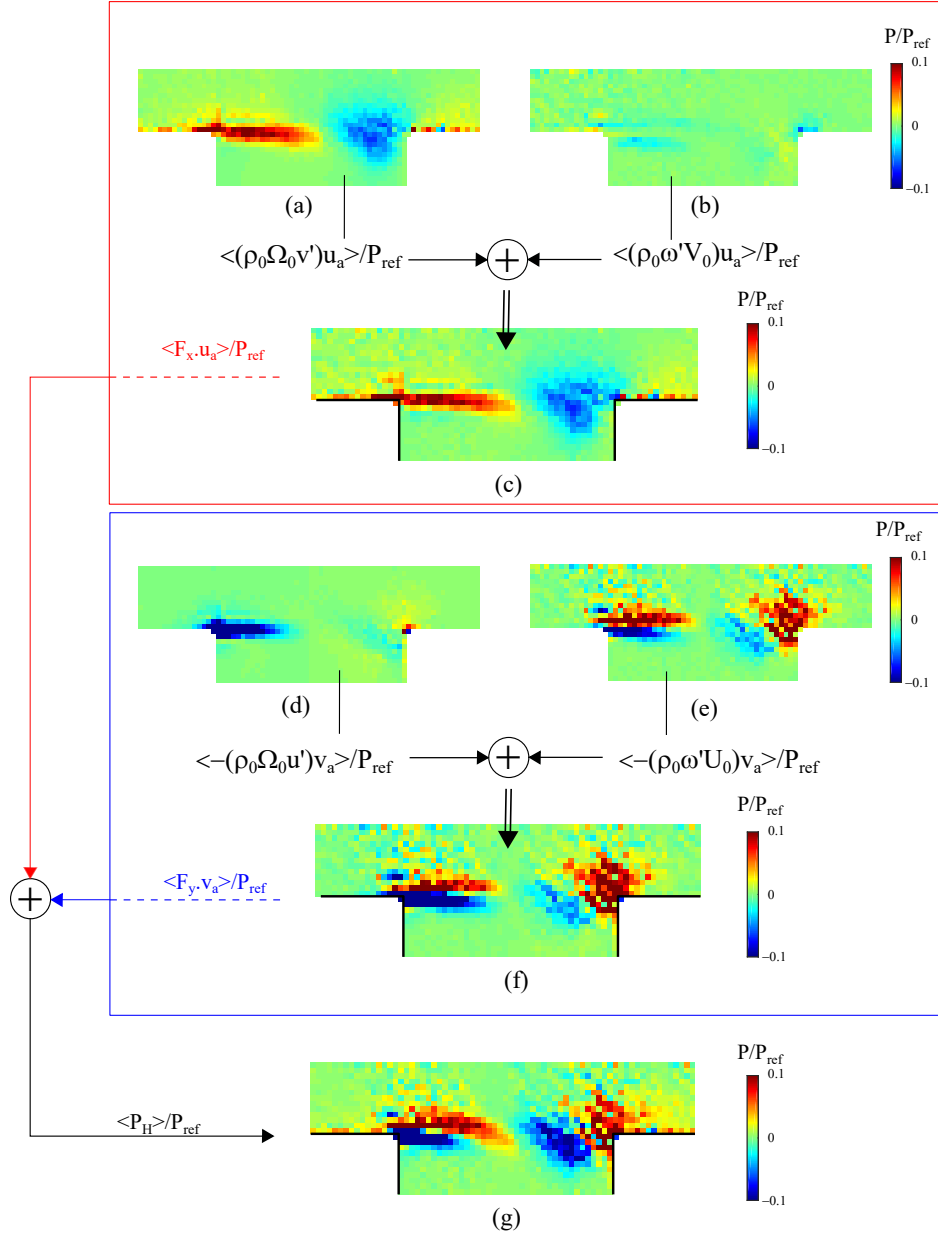


Figure 3.19 – Normalised acoustic power due to the horizontal (c) and vertical (f) Coriolis force, respectively split into their two main contributions (a-b) and (d-e) following Eq. 3.10, for the 2000 Hz case. Finally, the total acoustic power (g) is shown.

discontinuity. Furthermore, from figure 3.10, we can see that the velocity v' has a very small phase gap with the vertical acoustic velocity v_a and therefore the two components have the same sign. Therefore, when the vertical acoustic velocity v_a is negative at the leading edge, the Coriolis term $\rho_0(\Omega_0 v')$ is here positive. At the same time, the horizontal acoustic velocity

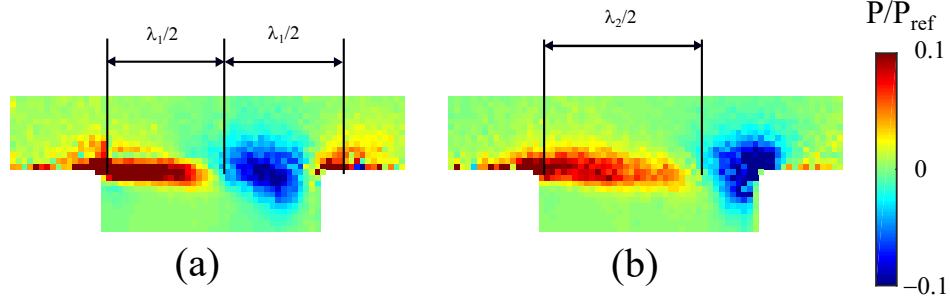


Figure 3.20 – *The normalised acoustic power contribution $(\Omega_0 v')u_a$ for the (a) 2000 Hz and (b) 1400 Hz upstream case at $\phi = \pi/3$.*

u_a here is positive and so is the contribution $\rho_0(\Omega_0 v')u_a$. Meanwhile, at the trailing edge, the vertical velocity v' is now positive (see figure 3.10) while Ω_0 is still negative and the Coriolis term $\rho_0(\Omega_0 v')$ is therefore negative. As the horizontal acoustic velocity u_a is here still positive, an acoustic absorption will be observed. From figure 3.20, we notice that the main change with frequency is the absorption position at the trailing edge. This is due to the fact that the length λ_i is influenced by the frequency while the phase gap between the acoustic and coherent velocities is not. Furthermore, the fact that the magnitudes of the velocities v' (see figure 3.11-b) and u_a don't change along the cavity and that the Ω_0 integral along the y -axis is supposed to stay constant while moving from the leading onto the trailing edge, suggests why the contribution $\rho_0(\Omega_0 v')u_a$ does not show a dependency on frequency (see figure 3.23).

In figure 3.20, the comparison of the $\rho_0(\Omega_0 v')u_a$ contribution for the 2000 and 1400 Hz case is shown, at $\phi = \pi/3$.

3.4.3 Acoustic Power $-\rho_0(\Omega_0 u')v_a$ contribution

In order to describe the $-\rho_0(\Omega_0 u')v_a$ contribution, the same considerations that were made above for the Ω_0 term apply also here. At the leading edge, it can be seen from Figure 3.11 that the horizontal coherent velocity u' is positive when the acoustic velocity v_a is negative. Then, in this position, the Coriolis force is positive when it interacts with a

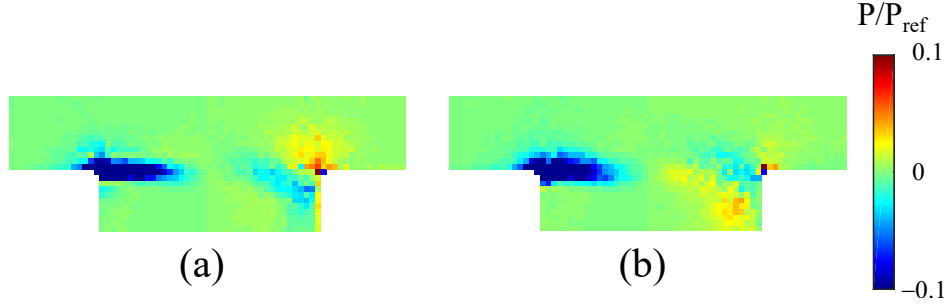


Figure 3.21 – *The normalised acoustic power contribution $(-\Omega_0 u')v_a$ for the (a) 2000 Hz and (b) 1400 Hz upstream case at $\phi = \pi/3$.*

negative (downward) acoustic velocity, and viceversa. Thus, a negative acoustic contribution $-\rho_0(\Omega_0 u')v_a$ is induced. Also, we can see from Figure 3.11, that the velocity u' is always very small close to the trailing edge of the cavity, due to the presence of the cavity hard wall. This explains why, in Figures 3.21, the acoustic power at the trailing edge is very small. From this follows also why this contribution is negative over the period and for all frequencies (see figure 3.23).

In figure 3.21, the comparison of the $-\rho_0(\Omega_0 u')v_a$ contribution for the 2000 and 1400 Hz case is shown, for $\phi = \pi/3$.

3.4.4 Acoustic Power $-\rho_0(\omega'U_0)v_a$ contribution

If we look at the acoustic power contributions from the vertical Coriolis force F_y (see figure 3.19-e,f), the term $-\rho_0(\omega'U_0)v_a$, which is the largest contribution, appears to be the one that gives the power distribution its complexity. Inside the Coriolis force $-\rho_0(\omega'U_0)$, the mean horizontal velocity U_0 is positive at all points. Moreover, its magnitude does not change strongly along the cavity length and these variations are confined in a very thin shear layer at the cavity lid. The largest thickness of this layer is around 1 mm (see figures 3.5a-c). Therefore, the Coriolis contributions inside the cavity are filtered out and their sign are opposite to the vorticity one. Then, at the leading edge, two counter rotating vorticity zones

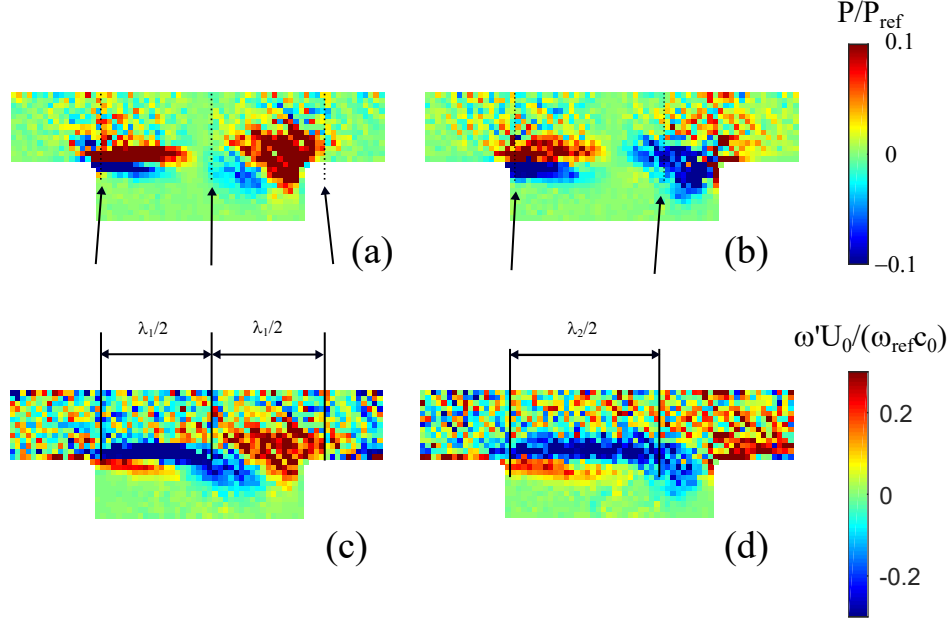


Figure 3.22 – The normalised acoustic power contribution $(-\omega'U_0)v_a$ for the (a) 2000 Hz and (b) 1400 Hz upstream cases at $\phi = \pi/3$. In (c) and (d) the Coriolis force $-\rho_0(\omega'U_0)$ is shown for the 2000 and 1400 Hz cases, respectively, at the same phase.

(as explained before, see figure 3.13) will interact with the v_a component, giving opposite acoustic powers, of which the positive one (over the cycle) is larger. At the trailing edge, the ω' structure will vary with frequency as the v' structure does. In order to have production at the trailing edge, vorticity here should have the same sign of the prevailing vorticity at the leading edge, as here the velocity v_a has an opposite sign. This should happen optimally when the vorticity period is $\approx 2(W/U_c)/3$. For the 2000 Hz case, the period is slightly larger at $\approx W/U_c$. Thus, we are not at the point of maximal production, but two co-rotating vorticity areas at the edges of the cavity are however allowed. When the period becomes larger (e.g. for the 1400 Hz case), this is not possible anymore and the vorticity at the leading and trailing edges will have opposite sign, which translates in absorption at the trailing edge. In figure 3.22, the comparison of the $-\rho_0(\omega'U_0)v_a$ contribution for the 2000 and 1400 Hz case is shown, for $\phi = \pi/3$.

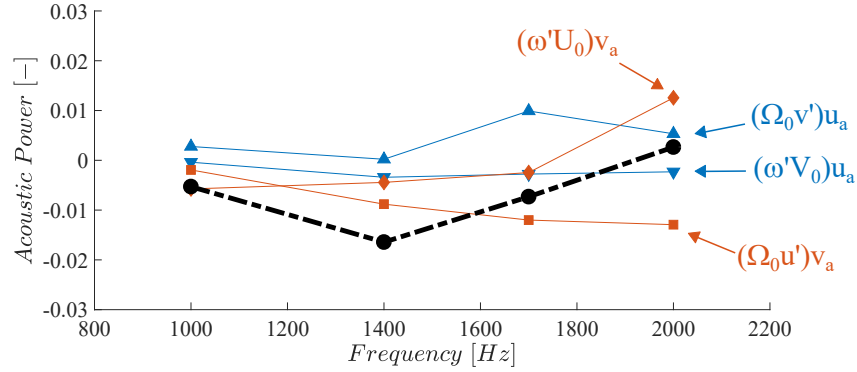


Figure 3.23 – Normalised acoustic powers contributions $(\Omega_0v')u_a$ and $(\omega'V_0)u_a$ (filled upward and downward blue triangles, respectively) and contributions $(\Omega_0u')v_a$ and $(\omega'U_0)v_a$ (filled red squares and diamonds, respectively) for the $f = 1000, 1400, 1700, 2000$ upstream source cases. Also, the total acoustic power is shown in filled black circles

3.4.5 Acoustic Power contributions: Summary

In summary, it has been shown that the acoustic power related to the horizontal Coriolis force is on the average close to zero: this is because the component $\rho_0(\omega'V_0)u_a$ is negligible everywhere in the aeroacoustic field while the integral of the $\rho_0(\Omega_0v')u_a$ contribution over the period is zero, even if local production and absorption areas are present at the cavity edges. Therefore, it is the vertical Coriolis force contribution who finally determine the behaviour of the corrugated wall. In this contribution, the $-\rho_0(\Omega_0u')v_a$ term is responsible for an absorption area at the leading edge which is always negative with frequency. Then, the frequency dependency of the absorption and production mechanisms derives from the $-\rho_0(\omega'U_0)v_a$ term, which is also responsible for the complexity of the acoustic power distribution. In this case, the acoustic frequency influences the hydrodynamic wavelength and the coupling with the cavity length: when the wavelength is close to the $2W/3 + nW$ value (with n integer), global acoustic production is possible.

The complexity resulting from the different contributions to acoustic production cannot be captured through the models usually employed when whistling is present. The simplifications adopted in this case are not applicable here: vorticity cannot be considered concentrated

in a single moving vortex (like in the SCV model) as it is distributed over the entire cavity. Furthermore, it has a complex distribution perpendicular to the shear layer while spreading out along the cavity, a behaviour which is not taken into account in the SDV model. This shows that the models usually adopted in presence of the whistling cease to be applicable in the linear regime.

3.4.6 Effect of Sound Propagation Direction

As explained before (see section 3.3.2), the main effect of changing the acoustic source position is the introduction of a phase difference in the hydrodynamic structures. This influences the acoustic production, as shown in Figure 3.24, where the total acoustic production for an acoustic source frequency of 2000 Hz is presented, for both a relative upstream and downstream source positions. Indeed, the phase difference for the downstream case shifts upstream the production region at the trailing edge, which increases the overall interaction. At the same time, the differences at the leading edge appears negligible. This is highlighted in Figure 3.24-c,d, where the nondimensionalised vertical Coriolis force $-\rho_0(\omega'U_0)$ is shown. There, it appears that the main difference in the Coriolis distribution is the upstream shift of the trailing peak, which will therefore have a larger contribution.

3.4.7 Leading Edge Shape Effect

The effect of changing the leading edge is dual: the hydrodynamic structures will be able to start forming earlier (as the detachment point will be moved upstream w.r.t. the sharp leading edge) and they will have to travel a larger length before encountering the trailing edge. The way these two effects can influence the acoustic production can be understood from Figure 3.25: in (c-d), the Coriolis contributions $-\rho_0(\Omega_0 u')v_a$ are shown for the two types of leading edges with an upstream acoustic source at 2000 Hz. We can see that, for a rounded leading edge, the second positive node is almost not modified by the trailing edge

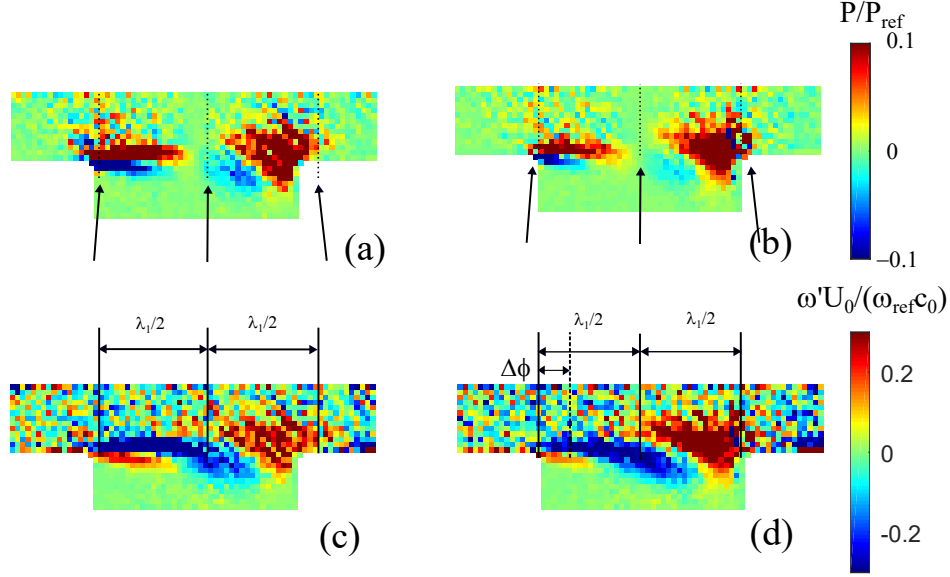


Figure 3.24 – *The normalised acoustic power contribution $(-\omega'U_0)v_a$ for the 2000 Hz (a) upstream and (b) downstream case at $\phi = \pi/3$. In (c) and (d) the Coriolis force $-\rho_0(\omega'U_0)$ is shown for the 2000 Hz upstream and downstream cases, respectively, at the same phase.*

when compared to the sharp edge case. Also, this interacts with weaker acoustic vertical velocity thus delivering less acoustic production (as seen from Figure 3.25 -b). At the leading edge, the difference is due to the different Kutta condition: for the rounded case, the vertical gradient of the acoustic velocity u' is not as strong reducing the bottom counter rotating area.

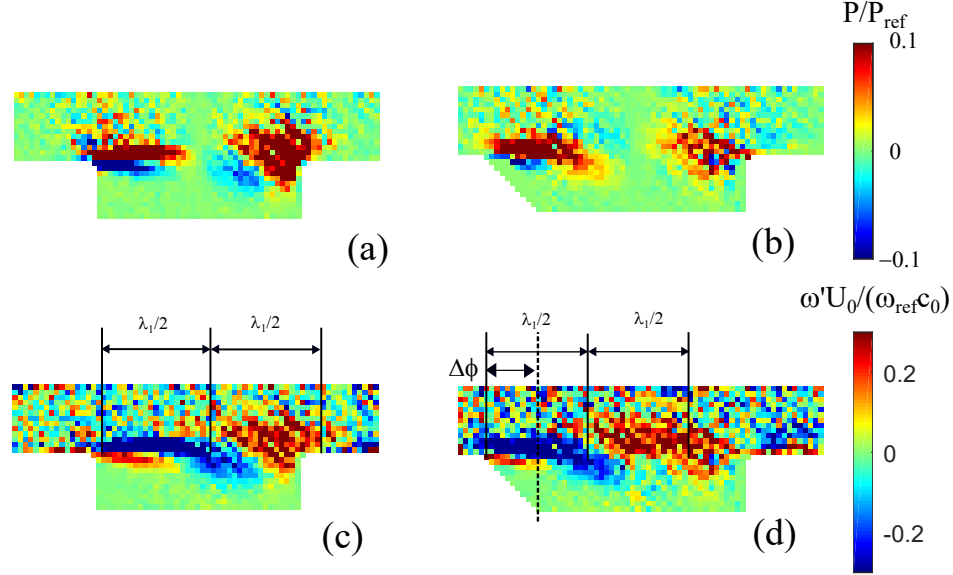


Figure 3.25 – *The normalised acoustic power contribution $(-\omega'U_0)v_a$ for the 2000 Hz upstream (a) sharp and (b) round case at $\phi = \pi/3$. In (c) and (d) the normalised Coriolis force $-\rho_0(\omega'U_0)$ is shown for the 2000 Hz upstream sharp and round cases, respectively, at the same phase.*

3.5 Conclusions

The aeroacoustic field around a corrugated wall in a grazing flow configuration has been studied. First, we investigated the behaviour of the corrugated plate over a wide frequency band by measuring the scattering matrix of the test sample. This allows to understand how the corrugations behaved globally and whether or not the Strouhal numbers corresponding to the characteristic frequencies were similar to the ones obtained in previous studies. Indeed, as expected from the literature, characteristic frequency ranges where transmission coefficients were higher/lower (namely "gain/loss" zones) than the corresponding no-flow configuration have been identified. For all cases, however, the transmission coefficients stay below unity as opposed to other studies. This is mainly because in the present setup the corrugated plate is covering only one side of the waveguide. Then, the acoustic source frequency and the flow Mach number have been set in order to investigate four points between the "gain" and the

"loss" zones using the optical LDV technique. The main quantities which identify the fluid-dynamic as well as the acoustic fields have been fully resolved. In particular, coherent velocity structures are clearly visible and their propagation velocity appears to be weakly function of frequency. Also, the coherent vorticity, which is directly responsible for the acoustic power production/absorption is well resolved. However, it is not possible to isolate distinct zones of absolute acoustic power absorption or production as these are usually entangled in a complex form due to the acoustic forcing of the hydrodynamic velocity at the leading edge. However, even in this complex scenario, it is possible to appreciate how a change in frequency (i.e. a different separation between the velocity structure) or in the source position (i.e. a relative space shift in the velocity structures) can explain the gain/loss mechanism. These results also indicate that either one of the 1D models (DV/CV models) is hardly going to give good predictions. First, source/sink contributions are not distinct between each other in the measurement volume. Furthermore, the entanglement at the leading edge cannot be considered in a 1D modeling, as well as the power contribution from the longitudinal Coriolis term. Also, the contribution to the vertical Coriolis term of the horizontal coherent velocity (i.e. $(\Omega_0 u')$) is somewhat non negligible and usually not considered. All these contributions are necessarily not taken into account in a 1D model, which suggests that such a model would not be a good predictor of the acoustic power. Further studies will therefore need to account for these discrepancies in order to improve the modeling accuracy. The open access to the dataset [43] will help speed up this process, which combined efforts should be able to solve.

Chapter Four

Investigation about Helmholtz resonators and a Transparent Layer

4.1 Introduction

Metamaterials offer new opportunities to attenuate or redirect sound waves [51, 52]. New applications are already being considered, particularly in the field of aeronautics [53]. In this framework, metamaterials are subjected to flows that can change their effect [54, 55]. In some applications, the metamaterials under consideration are porous, which raises the question of how acoustic waves can penetrate the material without the flow penetrating it. In the same way, acoustic cloaking with flow relies on the assumption that "the cloak's metamaterials are rigid and impervious to fluid but are transparent to sound waves" [56]. As this last research field is still mainly theoretical and numerical [57, 58], practical realizations of such a magic layer are not often discussed. The idea of using a Kevlar sheet is sometimes suggested [59] since acoustically transparent walls made from tensioned Kevlar cloth are nowadays used in wind tunnels [60]. However, the acoustic behavior of very large Kevlar walls (with respect to wavelength) is very different from that of smaller pieces. In fact, Kevlar cloth is a permeable membrane through which acoustics can pass in two ways. One is related to vibration, as through an impermeable wall, and the second to permeability, as through a rigid resistive

wall. For the first effect the important parameters are the mass per unit area and the tension of the film, while for the second it is the acoustic resistance (pressure drop divided by the normal fluid velocity). Of course, these two effects are always present [61] but we can think that when the size of the panels is small compared to the wavelength, it is the resistive effect which predominates and that if vibrations are involved, it is in the form of resonances which are localized in frequency. That is the subject of this paper.

For this, we consider an array of Helmholtz resonators located in the wall of a waveguide. The acoustic behavior of this metamaterial is first analyzed without flow. Then, it is shown that the addition of a flow greatly disturbs the resonator's acoustic performance, as whistling is induced. Finally, the array is covered with a kevlar fabric. The cloth strongly affects the acoustic behavior of the metamaterial in absence of flow, while whistling is prevented in presence of flow.

4.2 Experimental investigation

The model metamaterial studied in this paper consists of five identical Helmholtz resonators mounted in series [62, 63]. The scattering matrix of this sample is measured with and without flow, and with and without a Kevlar cloth glued on the top of the resonators.

4.2.1 Test rig and measurement procedure

An array of five Helmholtz resonators is located in the wall of a waveguide of rectangular section $H \times B$ with $H = 40$ mm and $B = 50$ mm, see Fig. 4.1(a). This duct facility has already been introduced in Chapter 2 and a mean flow whose velocity is up to 80 m/s can be produced by a centrifugal fan. The unit cell resonator is a square cuboid with a volume equal to $31 \text{ mm} \times 31 \text{ mm} \times B$. Five resonators are placed side by side, forming an array with a period of 35 mm, and the surface in contact with the flow has been polished to avoid any discontinuity that could disturb the mean flow, see Fig. 4.1(b). The cavity volume has

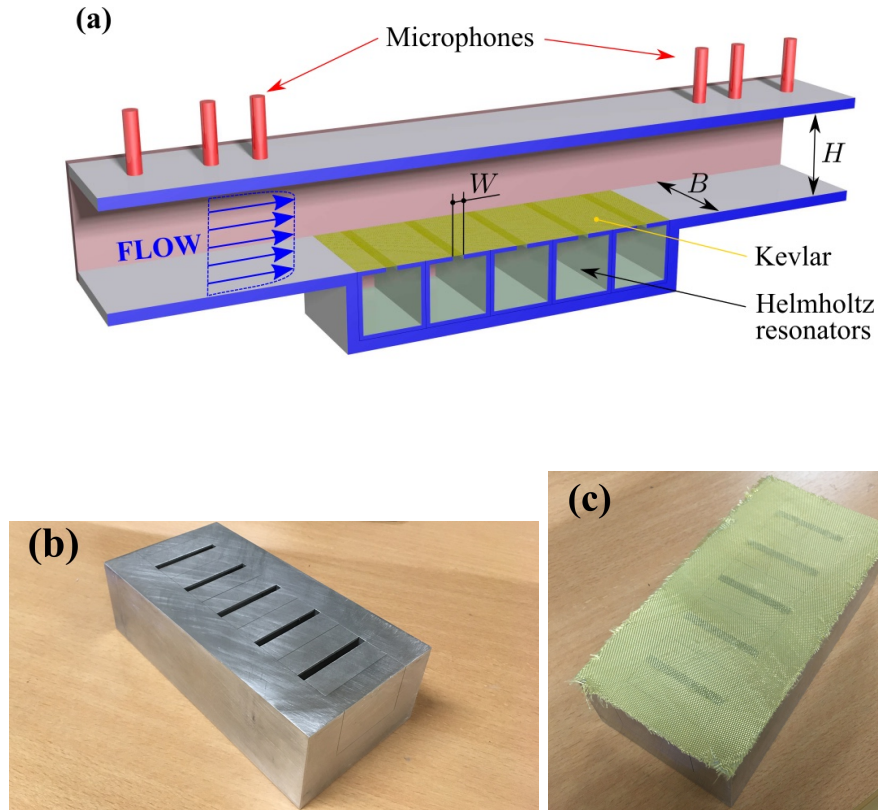


Figure 4.1 – (a) Sketch of the Helmholtz resonators mounted in a waveguide of rectangular section $H \times B$ with $H = 40$ mm and $B = 50$ mm. Three microphones are located on each side of the sample to determine its scattering matrix. The resonator cavity is a square cuboid with a volume equal to 31 mm \times 31 mm \times B . The neck of the resonator is a slit of thickness $t = 1.9$ mm, and its dimension in the direction of the flow is $W = 5$ mm. (Below) Picture of the metamaterial, without (b) and with (c) the Kevlar cloth. Only the central part, where the slits can be seen, is in contact with the inside of the duct.

been chosen so that a large transmission loss should occur within the target frequency range of liners designed for aircraft nacelles. The neck of the resonator is a slit whose dimension in the direction of flow is $W = 5$ mm. The slit extends over the entire width of the waveguide B , and its thickness is equal to $t = 1.9$ mm. These dimensions have been picked so that whistling phenomena would be expected in presence of flow for the range of flow velocities that are provided by the fan.

More than two meters of duct separate the fan from the test section. Thus, the flow can be considered as turbulent and fully developed when it reaches the Helmholtz resonators. The flow velocity is evaluated at the center of the duct downstream of the test section by a Pitot tube connected to a differential pressure sensor. This measurement gives the maximum value of the flow velocity in the duct section. It is then multiplied by 0.8 so that the value of the average velocity and the Mach number M are obtained [64]. The temperature inside the duct is measured by a type K thermocouple placed upstream of the test section.

The acoustic waves are generated by two compression chambers which can be placed either upstream, or downstream, of the test section. A sinusoidal sweep ranging from 200 Hz to 4000 Hz with a step of 5 Hz is used. As the frequencies studied are below the first cut-off frequency of the waveguide, only plane waves can propagate.

The sound pressure in the duct is recorded by two sets of three flush-mounted microphones located upstream (u_i) and downstream (d_i) of the test section, where $i = 1$ indicates the microphone located the closest to the test section. The positions of the microphones are $x_{u_1} - x_{u_2} = x_{d_2} - x_{d_1} = 30$ mm, $x_{u_1} - x_{u_3} = x_{d_3} - x_{d_1} = 175$ mm, and both u_1 and d_1 are placed 113 mm away from the metamaterial. All the microphones are calibrated relative to u_1 in a separate cavity mounted on a loudspeaker. At each frequency step of the sine sweep, the acoustic pressure on each microphone is calculated by averaging the pressure value over 400 cycles without flow, and over 1000 cycles with flow.

An overestimated determination of the incident and reflected waves on both sides of the metamaterial is performed. This decomposition is used to ensure, at each frequency step and

for every flow velocities, a constant amplitude of the incident acoustic wave. For that purpose, a first measurement is performed with a constant source level, and the recorded pressure field is decomposed in terms of incident and reflected acoustic plane waves. It appears that depending on the duct resonances, the incident wave amplitude changes with frequency. Next, we estimate the voltage that should be applied to the loudspeakers to compensate for the resonances. The experiment is then run again using these estimated levels, and the amplitude of the propagating waves are computed. If the amplitude of the incident acoustic wave is not in a 2% interval around the target value, here chosen as 120 dB, the optimisation routine is repeated. Otherwise, the elements of the scattering matrix of the metamaterial, namely the reflection and transmission coefficients (R^\pm, T^\pm) defined for incident plane waves coming from upstream (R^+, T^+) and downstream (R^-, T^-) of the sample, are computed. To obtain these four coefficients, two different acoustic states are needed. The first one is obtained by placing the compression chambers upstream of the resonators, the second one by placing them downstream. More details about this measurement technique, for the case of a cylindrical duct, can be found in [65].

4.2.2 Results without Kevlar

First, all the measurements with and without flow were carried out on the resonator array before gluing the Kevlar fabric on it. The results are shown by Fig. 4.2, which draws the transmission coefficients as functions of frequency. Without flow, there is a transmission dip in the vicinity of the resonance frequency of the Helmholtz resonators. There, the transmission goes down up to $|T| = 1.5 \cdot 10^{-4}$ (-76 dB). In the present investigation, the Bragg band gap lies outside the frequency range studied.

When the flow is present, it can be noticed that the transmission coefficients in both directions are now different. This is due to the loss of reciprocity when there is a flow. But the most striking fact is the peak at 1220 Hz which is larger than 1. It actually corresponds to

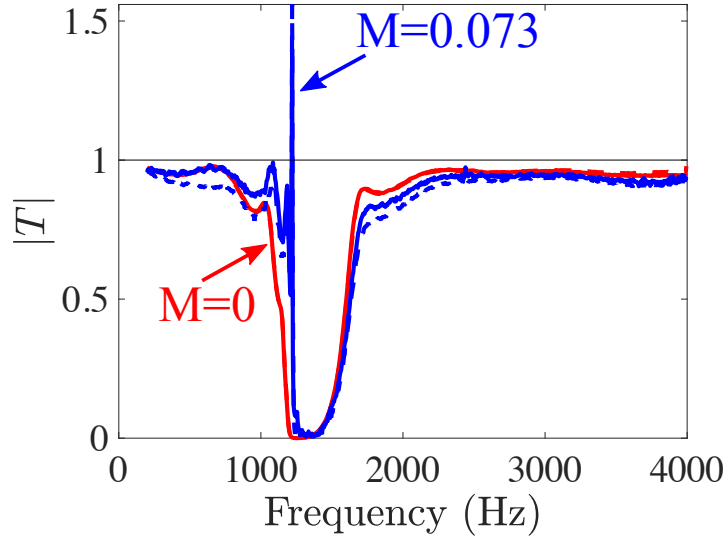


Figure 4.2 – *Transmission coefficients without Kevlar as a function of the frequency. The continuous lines represent T^+ (in the flow direction) while the dashed lines represent T^- (against the flow). The cases $M = 0$ and $M = 0.073$ are indicated in the figure.*

a whistling that is audible through the whole duct even in the absence of acoustic excitation. It should be noted that when whistling is present, the phenomenon becomes non-linear and the linear transmission as given in Fig. 4.2 becomes meaningless at the frequency of the whistling.

Consequently, even a weak flow as in the present case (the mean velocity in the duct is $U = 25 \text{ m.s}^{-1}$ corresponding to a Mach number $M = 0.073$) has a dramatic effect, since the metamaterial starts to produce sound. This whistling is quite usual when a flow grazes a Helmholtz resonator. Moreover, it appears in the classical range of the Strouhal number [66], since here $S_r = fW/U = 0.24$ where f is the frequency.

These results prove that something has to be done to prevent such sound-flow interactions and instabilities when metamaterials are exposed to a flow.

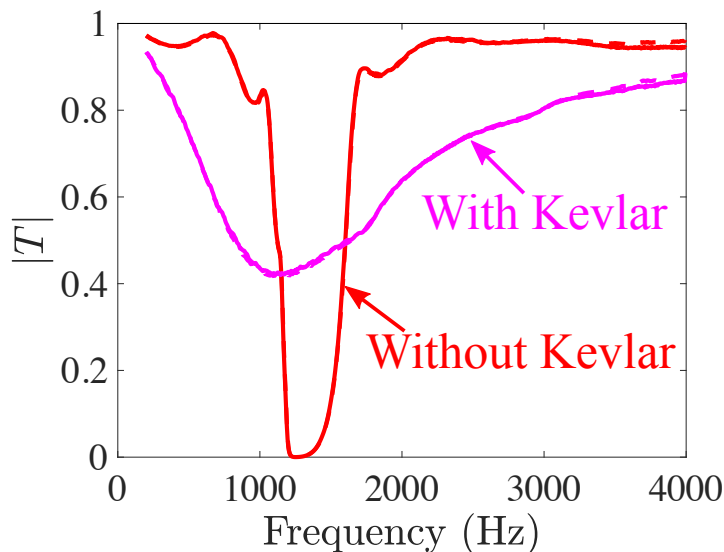


Figure 4.3 – *Transmission coefficients with and without Kevlar when there is no flow. The continuous lines represent T^+ (in the flow direction) while the dashed lines represent T^- (against the flow). The cases with Kevlar and without Kevlar are indicated in the figure.*

4.2.3 Results with Kevlar

A lightweight Kevlar 49 fabric (weight = 61 g/m², thickness = 0.12 mm) is now used to cover the resonators [67], see Fig. 4.1(c). Before being glued to the metamaterial, the piece of Kevlar was tensioned uniformly by using the mechanism of a 13-inch drum. The effect of the Kevlar sheet on the acoustic behavior of the Helmholtz resonators array when there is no flow is shown in Fig. 4.3, where the transmission coefficients measured with and without Kevlar are compared.

The drop in transmission in the vicinity of the resonance is much less pronounced with Kevlar (the minimum transmission is $|T| = 0.42$ i.e. -7.6 dB) than without it. On the other hand, this drop in transmission occurs over a much wider frequency range. This indicates that Kevlar produces a strong damping that decreases the resonance peak while widening it.

It is therefore incorrect to consider that the Kevlar sheet is completely transparent to acoustic waves.

The effect of flow on a Kevlar coated metamaterial is shown in Fig. 4.4. Again, it

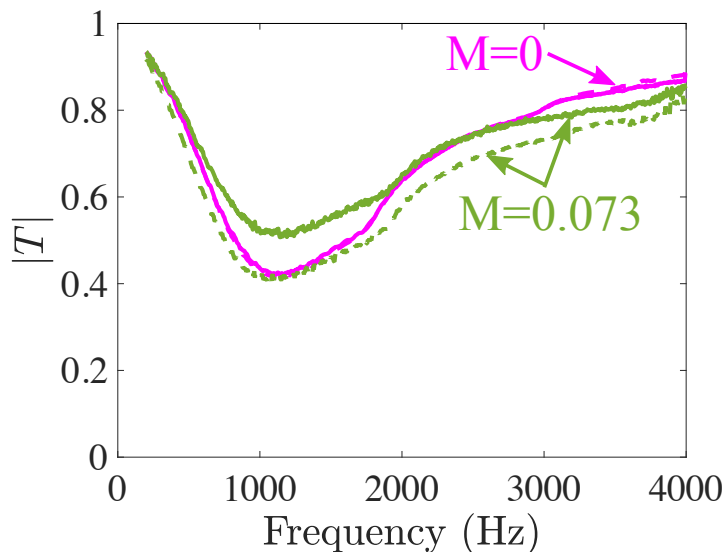


Figure 4.4 – *Transmission coefficients with Kevlar as a function of the frequency. The continuous lines represent T^+ (in the flow direction) while the dashed lines represent T^- (against the flow). The cases $M = 0$ and $M = 0.073$ are indicated in the figure.*

can be noted that, due to the lack of reciprocity, the transmissions in both directions are slightly different. Most noticeably, the effect of the flow is now much weaker than without the Kevlar cover. In particular, the whistling that appeared without Kevlar, has now completely disappeared.

4.3 Numerical approach

In order to better understand the phenomena involved in both Kevlar coating and flow, a numerical simulation is carried out. To this end, a multimodal method is used to calculate the linearized two-dimensional lossless problem with and without flow and to compare its results with experimental data. This method has already been described in detail elsewhere [68, 69, 70] and therefore only a few points are merely reported.

The linear propagation of small perturbations in a parallel sheared flow can be described by the linearized Euler equations (LEE). The multimodal method is used and the perturba-

tions are therefore expressed as a linear combination of acoustic and hydrodynamic transverse modes. These modes and wave numbers are computed on uniform segments using a finite difference method by discretizing the LEE in the transverse y -direction. The modes must be calculated in the neck of the resonator, knowing that there are: a shear flow above (for $0 < y < H$), a pressure discontinuity due to an impedance Z at $y = 0$, and no flow in the cavity (for $-t - C < y < 0$ where C is the cavity depth). The modes must also be computed outside the neck in the rigid pipe with a shear flow ($0 < y < H$) and in the cavity ($-t - C < y < -t$). The scattering matrix of one cell is found by using axial velocity cancellation on the vertical walls and by matching the modes at each discontinuity. The transmission and reflection coefficients of all five Helmholtz resonators are determined by combining the unit scattering matrices.

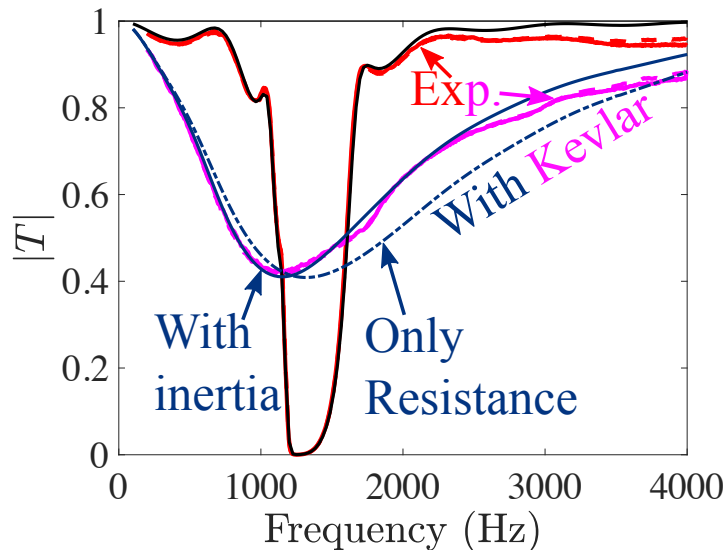


Figure 4.5 – Transmission coefficients without flow ($M = 0$) with and without Kevlar as a function of the frequency. The experimental results are indicated in the figure, all the other curves are obtained with the multimodal method. For the results with Kevlar, the dash-dotted line is produced when $Z = 0.34$ (purely resistive case) and the continuous line when inertia is added: $Z = 0.34 + i 0.075(f/f_R)$ where $f_R = 1250$ Hz.

The results without flow are presented in Fig. 4.5. Without Kevlar, the agreement between the measurements and the calculations is quite good, although there is a small

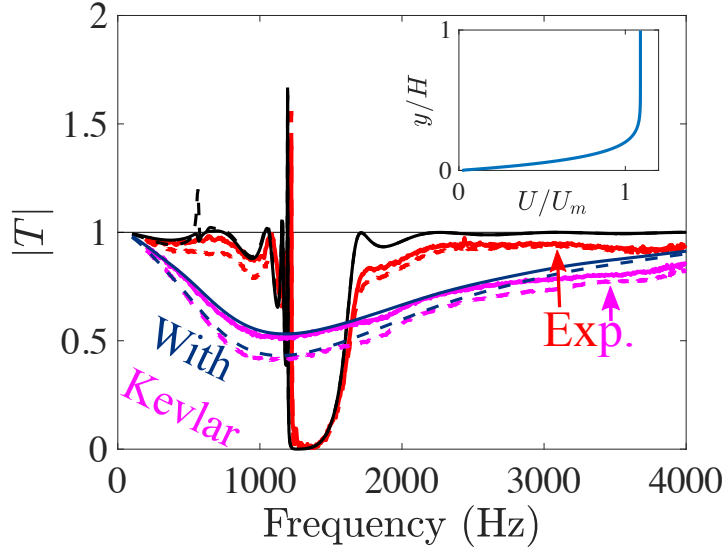


Figure 4.6 – *Transmission coefficients with flow $M = 0.073$ with and without Kevlar as a function of the frequency. The experimental results are indicated in the figure, all the other curves are obtained with the multimodal method. The continuous lines are in flow direction and the dashed lines are measured or computed against the flow. The multimodal method results with Kevlar are obtained with $Z = 0.42 + i0.062(f/f_R)$ where $f_R = 1250$ Hz. The inset gives the flow profile used during the computation.*

deviation at high frequency which must be due to the lack of consideration of viscous losses in the model. The presence of Kevlar was first modeled by a pure resistance and this gives the dash-dotted curve in the Fig. 4.5. In this case, the reduced impedance of Kevlar is purely real and equals to $Z = 0.34$ where $Z = \Delta p / \rho_0 c_0 v$, Δp is the difference in sound pressure between the two faces of Kevlar, ρ_0 is the density of the air, c_0 is the speed of sound and v is the acoustic velocity through Kevlar. The main effect of Kevlar is therefore the addition of a resistance. Beside this, a slight shift in frequency of the attenuation peak is observed and a better tuning is obtained when an inertial part is added to the impedance as $Z = 0.34 + i0.075(f/f_R)$ where $f_R = 1250$ Hz is the resonance frequency of the resonator. However, our experimental device does not allow us to know if this added mass comes from a vibration of the Kevlar or from a contraction effect when the sound enters the Kevlar fabric openings.

The numerical results with flow are compared in Fig. 4.6 with the experimental results. An amplification ($|T| > 1$) at a frequency very close to the whistling frequency is predicted by the model. This amplification is very sensitive to the shape of the profile which is here defined by a number n such that $U = U_m(1 - (1 - y/H)^n)(n + 1)/n$, where U_m is the mean velocity. In the present calculation, this number is equal to $n = 15$ and the profile is given in the inset in Fig. 4.6. As n increases, the flow boundary layer becomes thinner and the calculation becomes more unstable. In the presence of Kevlar, the computation correctly predicts the measurements when the impedance is equal to $Z = 0.42 + i0.062(f/f_R)$. It can be noticed that with flow the resistance of Kevlar is slightly greater than without flow, and the added mass is smaller. The same observations have for instance already been made for perforated plates [1] or for a thin slow sound material [55]. The boundary layer instability that occurs in the neck of the resonator in the absence of Kevlar is completely removed by the addition of the resistive layer that Kevlar constitutes. In this sense, Kevlar allows much closer acoustic behavior with and without flow.

4.4 Conclusion

The metamaterials must be protected from flow, otherwise extremely unpleasant interactions between acoustics and flow can occur. For the metamaterial studied in this paper, this is materialized by the appearance of a loud whistling sound in the vicinity of its resonance frequency. To avoid these undesirable effects, it would be good to have a "magic layer" that allows acoustics to pass through while suppressing sound-flow interactions in the vicinity of the material. A possible realization of this layer based on Kevlar fabric has been tested. Although reducing the effects of flow, this Kevlar layer is not acoustically neutral. It can be described by an acoustic resistance (associated with a low inertial effect). This resistance partly destroys the effect of the metamaterial on the sound when it is not accounted for in the design. Thus, Kevlar is not a magic layer.

Other realizations can be imagined (membranes, flexible beams with micro-slits, ...) which overcome the effect of the flow, but which also allow taking advantage of the interactions between the flow and the deformable structures to have very original behaviors.

Chapter Five

Vibrating Beams Investigation

5.1 Introduction

Since the aero-acoustic dissipation process in presence of an external flow is not a conservative one, it implies that there could be clever ways for exploiting this process. In this sense, in the past there has been a vast interest into vibrating mechanisms as they are able to absorb energy around their natural frequency (or even extract energy, e.g. in the case of loudspeakers). Among the first studies about vibrating membranes, we can find [5] and [6]. Here, the paper investigates a system of membranes put above an honeycomb structure and the relative performance of single elements compared to their combination. Similarly in [71], the analysis of a membrane both with and without perforation is carried out: the perforation is shown to reduce the maximum TL but to introduce at the same time an antipeak at a lower frequency than the main one, thus enhancing low frequency response. In [7] hybrid resonances are, on the other hand, obtain through a backed up cavity sealed off and filled with *SF6* gas which allow the membrane to obtain perfect absorption for a normal propagation at large subwavelength conditions. In [72] the transversal propagation along a vibrating membrane is investigated, together with an active mechanism based on electromagnetic forces to control the membrane itself. Results show interesting effects regarding the adoption of an electromagnetic mechanism as its effects are both positive, through a dynamic effect,

in enhancing the absorption around first eigenmodes and toward lower frequencies but also detrimental, through a static effect, that increases the stiffness of the membrane by an added tension contribution. Finally, in [73] a beam-like vibrating element was adopted together with a backing cavity to achieve perfect absorption at mid frequency and non negligible absorption at lower frequencies.

Using this idea as a starting point, the concept of cantilevered thin blades that can move above a cavity is investigated. In order to soften these blades, two I-shaped cuts are introduced. The first one makes the fixation less rigid while the second, realised in the middle of the beam, leads to bi-articulated blades with two degrees of freedom and a low stiffness. First, a simple analytical model is proposed to predict the behaviour of the blade. Then, a parametric study is performed in order to design experimental samples. The first experiments are conducted in an impedance tube, where both the acoustic in the duct and the vibration of the beam are measured. The closeness of the experimental and the analytical results indicates that the right physical phenomena have been identified. Finally, a last set of experiments performed in a grazing flow facility gives hint about the possible application of such acoustic treatments to aircraft noise reduction.

5.2 Vibrating Beams

The considered vibrating beam is composed of 5 x 3 identical beams, each backed up by an independent cavity, in order to cover the whole width of the channel and thus reproduce a quasi-2D system. Then, this system can be represented by an in-line series of 5 beams of constant thickness (which depends on the material used, see table 5.1) and 18 mm long. Each cavity is 29 x 22mm and communicates with the main duct through a laser-cut micro-slit. The technology used makes it possible to create a slightly conical groove with a width of 50 μm at the narrowest point. These dimensions, as will be clear from the results shown in sections 5.5.1 and 5.5.2, were chosen in order to have the lowest resonance frequency (and

therefore the absorption peak) at the lower limit for a realistic problem such as an acoustic liner.

The test section in this case is shown in Figure 5.1, together with the 2D schematic system. Regarding the physical properties of the beam, the Young modulus can be expressed as $E = E_0(1 + j\nu\omega)$ where the coefficient ν represents damping. Finally, in order to obtain low resonance frequencies, one and two I-shaped cuts were made, depending on the configuration. These cuts were made using a very thin beam laser, as mentioned before, and divide the beam in two elements 9 and 7 mm long, starting from the clamped boundary.

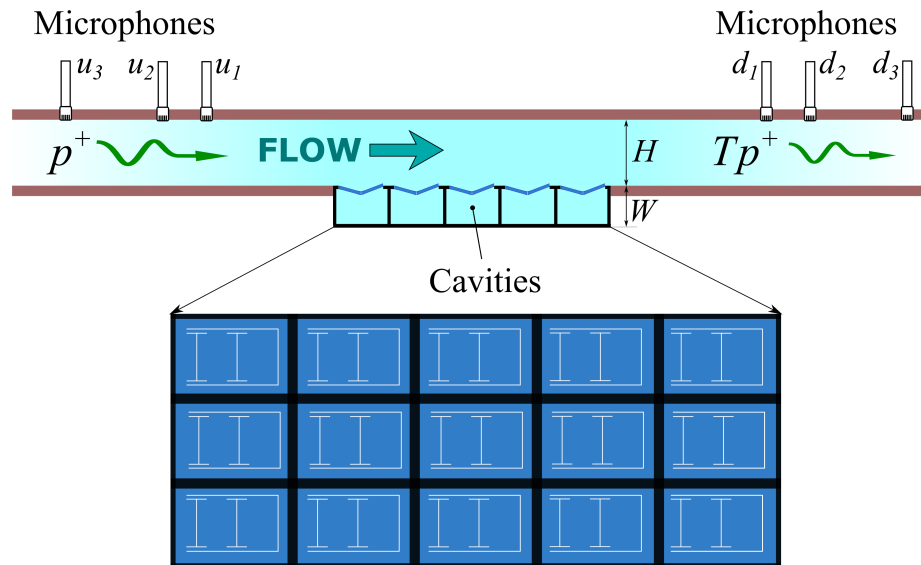


Figure 5.1 – (Top) Schematic representation of the grazing incidence facility used to characterise the liner sample using two sets of three microphones. The duct has a rectangular cross section of height $H = 4$ cm and a rotating lobe blower is used to introduce flow. (Bottom) The composite plate has been glued over 15 cavities of section 15×22 mm² so that there is one cantilever beam per cavity. The height of the cavities is $W = 30$ mm.

Material	Thickness	Young's Modulus	Configuration
Composite	0.46 mm	125 GPa	Double "I" cuts
Titan	0.20 mm	100 GPa	Double "I" cuts
Titan	0.20 mm	100 GPa	Single "I" cuts

Table 5.1 – *Vibrating Beam configurations*

5.3 Cantilever Beam Modeling

In this section, we want to investigate the behaviour of the cantilever beam when subjected to an aeroacoustic forcing. In order to do so, it is important to model the parameters of such a beam which characterise its frequency response. Generally, as we are considering harmonic excitations, we can assume that the beam will react through the sum of proper mode displacements each corresponding to a natural frequency of the system. Then, the displacement of the beam can be described as:

$$\delta(x, t) = \delta(x)e^{j\omega t} \quad (5.1)$$

where the spatial contribution can be written as

$$\delta(x) = \sum_i A_i \phi_i(x) \quad (5.2)$$

i.e. as a sum of the i -th ϕ_i mode multiplied by its amplitude A_i . The modal displacement is a continuous function of the longitudinal coordinate along the beam. A first case could be the example of the dynamic equation of a cantilever beam while a second case could be represented by a piecewise elements beam. If we consider then a 2D cantilever beam, its vertical displacement can be described by the following equation:

$$M \frac{\partial^2 \delta}{\partial t^2} + K \frac{\partial^4 \delta}{\partial x^4} = \Delta p \quad (5.3)$$

where M is the beam mass, K its flexural rigidity and Δp the total difference pressure load between its lower and upper surface. The beam mass can be expressed as $M = \rho_b e$ where

ρ_b is the beam material density and e its thickness, while the flexural rigidity K can be expressed as $K = EI$ i.e. the product of the Young modulus E and the momentum inertia I . Then, by applying the boundary conditions for a displacement in the form of eq. 5.2 and relative reacting forces, it can be shown that we obtain a trascendent displacement equation

$$\cos(\beta L) \cosh(\beta L) = -1 \quad (5.4)$$

where

$$\beta = \left(\omega^2 \frac{M}{K} \right) \quad (5.5)$$

and whose solution is in the form $\beta_i L = \frac{[(i-0.5)\pi]^2}{2\pi}$ for $i = 4, \dots, n$ while $\beta_{1,2,3} L = 1.875, 4.694, 7.855$ (see, for example, [74]). Therefore, the natural frequencies will be described as

$$\omega_i = \frac{\beta_i^2}{2\pi} \sqrt{\frac{K}{M}} \quad (5.6)$$

Alternatively, the beam can be assimilated to a plate rotating around its end with a restoring torque due to the deformation. The motion equation linking the rotation angle θ to the pressure difference between the two faces of the beam Δp is given in the frequency domain (time dependence in $\exp(j\omega t)$ where ω is the frequency) by:

$$- J\omega_i^2 \theta = \sum M = l\Delta p S_b / 2 - \beta\theta - \gamma j\omega\theta \quad (5.7)$$

where the moment of inertia is $J = \rho_b e S_b l^2 / 3$, ρ_b is the density of the plate, e the thickness of the plate and S_b is the area of the plate. The two coefficients β and γ are linked respectively to the stiffness and to the damping of the beam.

By defining the mean normal velocity of the beam by $v_b = lj\omega\theta/2$, the Eq. 5.7 can be transformed into an equation linking the pressure difference $\Delta p = p_i - p_c$ (p_i and p_c are the pressure just above the plate and just under the plate in the cavity) to v_b :

$$\begin{aligned} \Delta p &= \left[j\omega \frac{4}{3} \rho_b e \left(1 - \frac{\omega_b^2}{\omega^2} \right) + \rho_0 c_0 \delta \right] v_b \\ &= \rho_0 c_0 \left[jk_b e_b \frac{\omega}{\omega_b} \left(1 - \frac{\omega_b^2}{\omega^2} \right) + \delta \right] v_b = \rho_0 c_0 Z_b v_b \end{aligned} \quad (5.8)$$

where $k_b = \omega_b/c_0$ and $e_b = 4\rho_b e/(3\rho_0)$ is an equivalent thickness of the beam.

In the slits, the same pressure difference induces a mean velocity v_s given by

$$\begin{aligned}\Delta p &= \rho_0 c_0 (R_s + j k_b e_s \omega / \omega_b) v_s \\ &= \rho_0 c_0 Z_s v_s\end{aligned}$$

where R_s is the slit resistance and e_s the equivalent length of the slit. The continuity of the acoustic flux implies that

$$S_i v_i = S_b v_b + S_s v_s = S_c v_c \quad (5.9)$$

where S_i is the area corresponding to one periodic cell of the material, v_i is the incident vertical mean velocity on one cell, S_s is the area of the slits, S_c the transverse area of the cavity and v_c is the mean vertical velocity at the entrance of the cavity. The impedance of the cavity is given by

$$p_c = \rho_0 c_0 Z_c v_c = \frac{\rho_0 c_0}{j \tan(k_b W \omega / \omega_b)} v_c \quad (5.10)$$

where W is the thickness of the cavity. The continuity equation can be written as:

$$\left[\frac{S_b/S_i}{\rho_0 c_0 Z_b} + \frac{S_s/S_i}{\rho_0 c_0 Z_s} \right] (p_i - p_c) = v_i$$

from which the impedance Z_i seen by an incident wave can be calculated:

$$Z_i = \frac{p_i}{\rho_0 c_0 v_i} = \left[\frac{S_b/S_i}{Z_b} + \frac{S_s/S_i}{Z_s} \right]^{-1} + \frac{S_i}{S_c} Z_c \quad (5.11)$$

This impedance is that of a resonator placed in parallel with a resistor and loaded by a cavity.

Even if considered a simple vibrating beam, it is possible to consider several modes appearing. The displacement of the plate is then written as a sum of the displacements induced by these modes. The continuity equation (5.9) can then be written as such

$$S_i v_i = \sum_j S_b v_{bj} + S_s v_s = S_c v_c \quad (5.12)$$

where v_{bj} is the mean velocity induced by the j mode. Then, we can model the effect of the various modes j by considering that the impedance of the j mode can be written as

$$Z_{bj} = jk_b e_{bj} \frac{\omega}{\omega_b} \left(1 - \frac{\omega_{bj}^2}{\omega^2} \right) + \delta_j$$

ant that they are in parallel with the impedance of the micro-slits leading to

$$Z_i = \left[\sum_j \frac{S_b/S_i}{Z_{bj}} + \frac{S_s/S_i}{Z_s} \right]^{-1} + \frac{S_i}{S_c} Z_c \quad (5.13)$$

The three parameters that define each of the modes (equivalent mass, resonance frequency and modal damping) can be determined either analytically from the plate deformation equation (as mentioned above), numerically or experimentally.

5.4 Analytical results

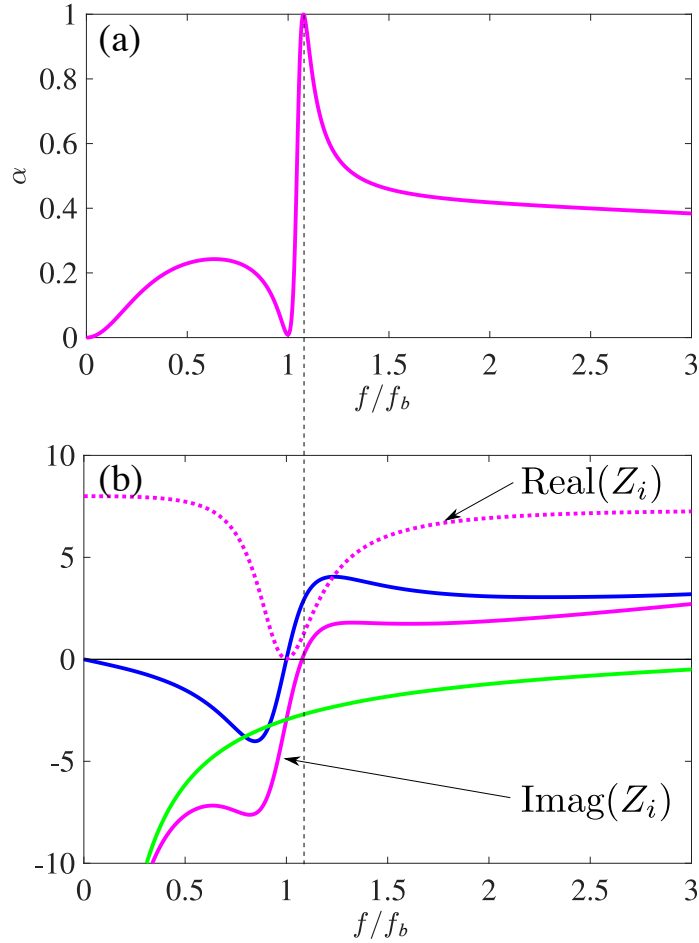


Figure 5.2 – (a) Absorption coefficient and (b) impedance computed from the mono-articulated model as a function of the frequency normalised by the plate resonance frequency. $S_b/S_i = 0.48$, $S_s/S_i = 0.0083$, $S_c/S_i = 0.825$, $k_b e_b = 0.8133$, $\delta = 0.01$, $R = S_i/S_s R_s = 8$, $k_b e_s = 0.0065$, $k_b W = 0.39$. The green curve is the imaginary part induced by the cavity and the blue curve is the imaginary part induced by the plate and the micro-slits.

The predicted acoustic behaviour of the system is displayed in Fig. 5.2. The absorption at normal incidence ($\alpha = 1 - \|(1 - Z_i)/(1 + Z_i)\|^2$) as well as the imaginary and real parts of the impedance Z_i are shown as functions of the frequency normalised by the plate resonance frequency. The values of the parameters given in the figure caption correspond to values close to those obtained experimentally. It can be seen that perfect absorption at normal

incidence can be achieved at a frequency that is closed to the resonance frequency of the plate. What generally limits the possibility to obtain low frequency attenuation with liners is the presence of the backing cavity whose reactance (green curve on Fig. 5.2) goes towards $-\infty$ as $1/k_0W$. The plate creates an additional reactance that is negative at low frequency and positive at high frequencies, with a rapid variation at the beam resonance frequency where zero is reached. If the plate reactance rises high enough, the cavity reactance can be counterbalanced and a total zero reactance is obtained for a frequency close to that of resonance. In the particular case displayed in Fig. 5.2, the ratio between the wavelength at the plate resonance and the thickness of the cavity is 16.2.

At the same time, in order to obtain perfect absorption, which occurs when $Z_i = 1$ for normal incidence, the coupled system resistance must be equal to 1. The resistance comes mainly from the dissipation in the micro-slits. However, near the resonance frequency the slits are short-circuited, and the velocity in the cavity comes mainly from the motion of the blade. As the structural damping of the plate is considered to be significantly lower than the slit resistance, the short-circuit in the vicinity of the resonance produces a localised dip in the resistance curve whose minimum value depends on the beam structural damping δ . Then, an appropriate choice of R and δ permits to obtain a resistance of 1 for the frequency at which the reactance is zero. Thus, perfect absorption is provided for a normally incident wave.

5.4.1 Influence of the parameters

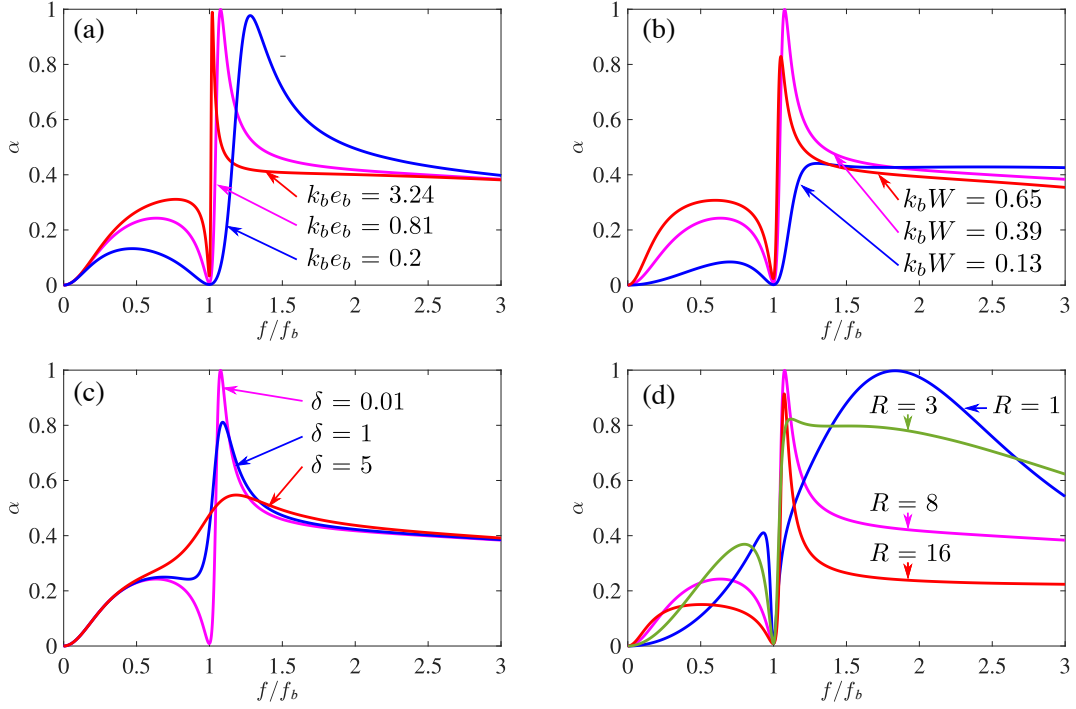


Figure 5.3 – Absorption coefficient computed by the mono-articulated model as a function of the normalised frequency. (a) Variation of the mass of the plate. (b) Variation of the thickness of the cavity. (c) Variation of the structural damping (d) Variation of the resistance. The magenta curves are the same that in Fig. 5.2(a).

The analysis of the effects of the problem parameters is illustrated in Fig. 5.3 where, starting from the reference configuration already shown in Fig. 5.2, the parameters are varied one by one.

The first parameter that can be changed is the mass of the plate, see Fig. 5.3(a). In practice, this mass can be changed either by modifying the material and thus the density, or by changing the thickness of the plate. Obviously, these changes will also involve a change in the plate resonance frequency f_b . A reduction in mass ($k_b e_b$ decreases) leads to a softer resonance but with the same amplitude. This leads to an increase in the frequency where the system is efficient, as well as a widening of the absorption bandwidth. A small adjustment of the structural damping δ is needed to achieve perfect absorption again.

A second parameter that could be modified is the thickness of the cavity W , see Fig. 5.3(b). As it is decreased, the zero crossing of the reactance moves to higher frequencies. At these frequencies, the corresponding resistance doesn't display a dip and is thus too high to induce good absorption.

The third parameter that is studied is the structural damping δ , see Fig. 5.3(c). The increase of δ makes the resonance less pronounced and increases the overall resistance (the resistance dip is less marked). On the other hand, it can be noted that the very low absorption values that were reached when $f = f_b$ are now increased because the structural damping takes over the damping in the slits when δ is large enough.

The last parametric study considers the resistance in the slits and the results are shown in Fig. 5.3(d). For this, we consider the resistance $R = S_i/S_s R_s$, which takes into account the percentage of open surface. Therefore, it is referred to the total surface. If the resistance increases, the width of the system efficiency peak is reduced. When $R=1$, the system works very differently. Indeed, the change in reactance due to the plate resonance is very weak and the reactance passes through zero for higher frequencies ($f/f_b= 1.84$ in this particular case). Such a frequency is outside the resistance dip and the resistance value is then very close to the nominal value of 1, which leads to perfect absorption for a frequency close to twice the resonance frequency of the plate. In fact, in this operating mode, the plate is in its inertial regime. Perfect absorption is then obtained with a system that consists of a mass (the plate), a resistance (the slits) placed in parallel and a stiffness (the cavity). Such systems are called In-Parallel Resonator and have been investigated in detail in [75]. In the present study, we are not interested in this type of operating mode, since the goal was to take an acoustic advantage of the plate resonance that occurs at lower frequencies. It can be noted that an intermediate resistance ($R = 3$) induces the two operating modes to work at the same time. Then, the operating band of the absorber is widened, at the cost of a decrease in maximal absorption which is now of the order of $\alpha = 0.8$ for $1.05 < f/f_b < 1.85$.

5.4.2 Influence of other modes of the plate

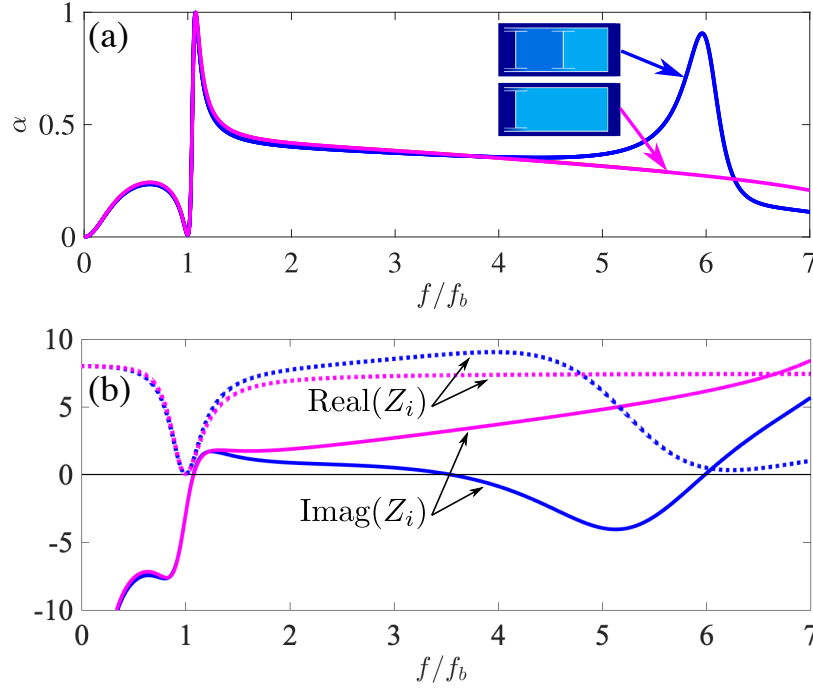


Figure 5.4 – (a) Absorption coefficient and (b) impedance as a function of the normalised frequency when one (mono-articulated plate, in magenta) or two (bi-articulated plate, in blue) modes are considered. For the first mode, the parameters are the same that in Fig. 5.2. The second mode is defined by $\omega_{b2} = 6.05\omega_b$, $k_{b2}e_{b2} = k_b e_b/8$ and $\delta_2 = 2.5\delta$.

In any deformable system, several modes can appear. The displacement of the plate is then written as a sum of the displacements induced by each of these modes. Thus, the continuity equation (5.9) now reads

$$S_i v_i = \sum_j S_b v_{bj} + S_s v_s = S_c v_c, \quad (5.14)$$

where v_{bj} is the mean velocity induced by the j -th mode. Then, the effect of the various modes j can be modelled by writing the impedance of the j -th mode as:

$$Z_{bj} = j k_b e_{bj} \frac{\omega}{\omega_b} \left(1 - \frac{\omega_{bj}^2}{\omega^2} \right) + \delta_j.$$

Considering that this impedance is in parallel with that of the micro-slits and in series with the one of the cavity leads to the following expression for the impedance of the coupled

system:

$$Z_i = \left[\sum_j \frac{S_b/S_i}{Z_{bj}} + \frac{S_s/S_i}{Z_s} \right]^{-1} + \frac{S_i}{S_c} Z_c. \quad (5.15)$$

The three parameters that define each of the modes (equivalent mass, resonance frequency and modal damping) can be determined either analytically from the plate deformation equation, numerically or experimentally.

To examine the effect of the additional modes, two modes are used to calculate the impedance and the absorption displayed in blue and compared in Fig. 5.4 to the results with only one mode. It can be observed that the first absorption peak is only slightly modified and that a second peak appears near the resonance frequency of the second mode. The resistance remains close to its nominal value (here $R=8$) except near the resonance frequencies where dips are found. An interesting effect of the presence of the additional mode is that the reactance decreases just after the first peak. Between peaks the reactance therefore remains close to zero, which is usually required for large acoustic attenuation.

5.5 Experimental validation

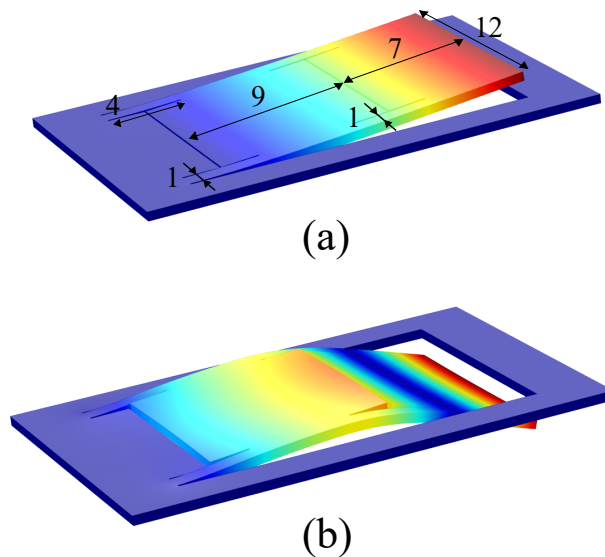


Figure 5.5 – (a) First and (b) second mode of the cantilever beam with the I-cut shaped slits, as computed using a finite elements method (Comsol). l_1 and l_2 are the lengths of the two parts of the beam.

To test the validity of the above model, tests were performed on a composite material plate. The plate of thickness 0.48 mm is made with a M21E/IMA carbon fiber/epoxy material. The IMA component (HexTow IMA, Intermediate Modulus Fibers) are continuous carbon fibers which are impregnated with a (Hexply M21E) epoxy resin. The density is 1586 kg.m^{-3} , the Young modulus is 125 GPa and the Poisson coefficient is 0.35.

Using the geometry and the material parameter, the vibration modes of the beam can be computed using a finite element method (Comsol). The first two vibration modes are shown in figure 5.5 . The first one corresponds to a mode where the motion is almost a pure rotation of the whole beam. The stiffness results from the deformation of the two arms at the base of the beam. There is a slight difference between the calculated frequency (854 Hz) and the measured frequency ($f_b = 730 \text{ Hz}$) which may result from uncertainties in the

material parameters due to the possible misalignment of the cuttings with the axes defined by the fibres of the material. The second mode is a bending mode ($f= 5315$ Hz) while the third mode ($f= 5371$ Hz) is a torsion mode which has an average velocity equal to 0 and is therefore assumed not to interfere with the acoustics.

Two samples have been made: one for a measurement in a normal incidence tube and a second one for a measurement in the wall of a rectangular duct. For these two samples the micro-cutting was performed in the same way and with the same geometry.

5.5.1 Normal incidence measurements

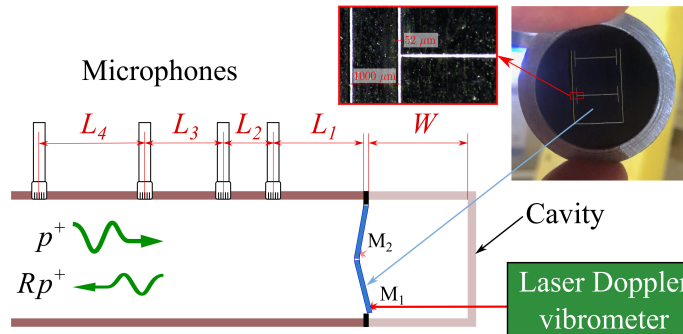


Figure 5.6 – Schematic diagram of the experimental setup for impedance tube measurements. The back cavity can be removed for measurements with the laser vibrometer.

The circular sample is glued onto a ring (inner diameter 30 mm, outer diameter 38 mm) and then placed in an impedance tube which is made of steel tubes with an inner diameter of 30 mm and a wall thickness of 4 mm, see Fig. 5.6. Four microphones (B&K 4136 and 2670 with amplifier Nexus 2690) are used for the overdetermined separation of incident and reflected waves. The microphones are distant of $L_2 = 30$ mm , $L_3 = 100$ mm and $L_4 = 285$ mm in order to cover a large range of frequencies. The length between the first microphone and the sample is $L_1 = 230$ mm. After an in-situ calibration of the microphones, the signal from the microphones and a laser vibrometer is transferred to a data acquisition system.

This system is used in sine sweep mode (from 100 to 4000 Hz with a 5 Hz step). At each frequency, all transfer functions are averaged over 500 cycles.

The measurement system allows to control the acoustic level of the incident wave. Several levels were tested but no non-linear effects were detected.

Vibrometer measurements

First, the velocity of the bi-articulated plate located at the end of the tube (without cavity) was measured at two points using a laser vibrometer when acoustic excitation is present. From the sound pressures measured on the three microphones, it is possible to calculate the sound pressure p_i that is applied to the plate. The velocities v_{M_1} and v_{M_2} measured respectively at the end of the plate and in the middle of the plate (on the first part, see Fig.5.6) related to the incident pressure are plotted in Fig. 5.7. The first two modes of the bi-articulated plate can be seen very clearly. The first mode is at a frequency of 700 Hz. For this mode, we find that $v_{M_1}/(l_1 + l_2) = v_{M_2}/l_2$ (l_1 and l_2 are define in Fig. 5.5) which indicates that this mode is very close to a rotation without deformation of the plate around its base articulation. For the second mode ($f = 3650$ Hz), the velocities are almost opposite $v_{M_1} \simeq -v_{M_2}$, which indicates that we are dealing with a bending mode as shown in Fig. 5.5. An average velocity can be computed, assuming two rigid plates pivoted to each other, by $v_b = v_{M_2}/2 + l_1 v_{M_1}/(l_1 + l_2)$. This averaged velocity is also plotted in Fig. 5.7. Assuming a low radiation impedance of the tube and therefore zero sound pressure on the outside of the plate, this average velocity relative to the sound pressure on the plate is the inverse of the impedance of the plate defined by Eq. 5.8: $Z_b = p_i/(\rho_0 c_0 v_b)$

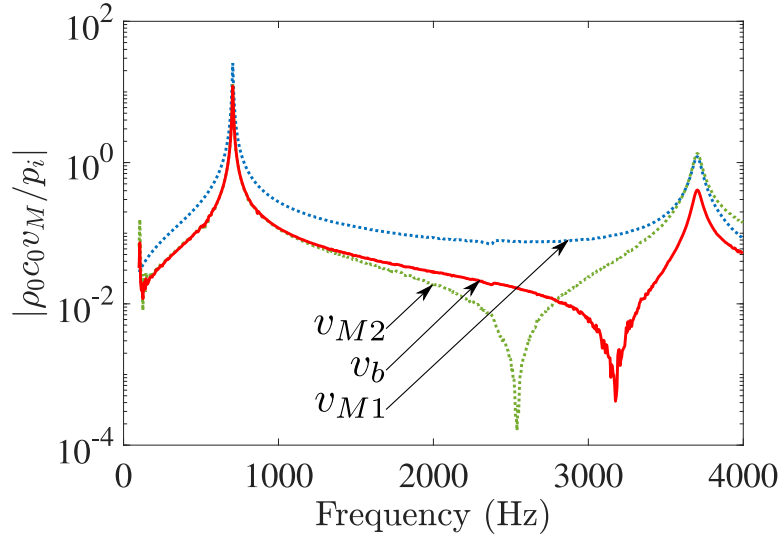


Figure 5.7 – Dimensionless ratio between the velocities v_{M_1} and v_{M_2} and the pressure on the plate p_i . v_b is the average velocity along the plate.

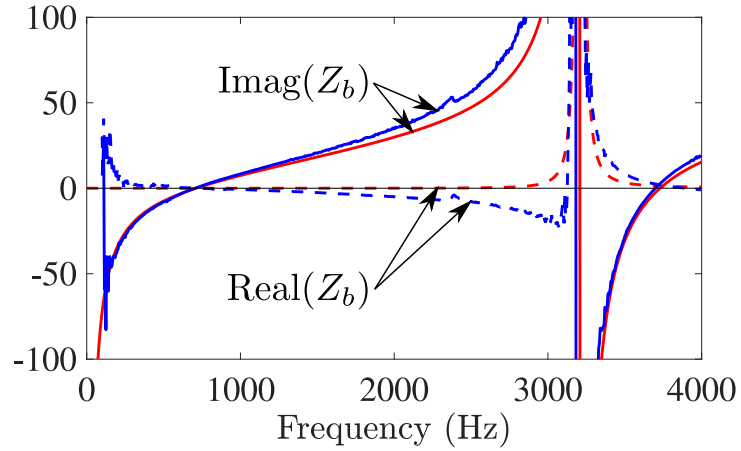


Figure 5.8 – Impedance of the beam Z_b deduced from the laser vibrometer measurements. The blue curves are the measurements and the red ones to the fit given in the text.

These laser vibrometer measurements confirm that the impedance Z_b can be described by the contribution of the first two modes with :

$$\frac{1}{Z_b} = \frac{1}{Z_{b_1}} + \frac{1}{Z_{b_2}}$$

where

$$Z_{b_1} = j A_1 \frac{f}{f_1} \left(1 - \left(\frac{f_1}{f} \right)^2 \right) + \delta_1$$

$$Z_{b_2} = j A_2 \frac{f}{f_2} \left(1 - \left(\frac{f_2}{f} \right)^2 \right) + \delta_2$$

and this vibration measurement allows to experimentally determine some parameters of the model described in section 5.3.

Indeed if some of them are easily computable such as the equivalent mass of the beam for the first mode, others are more difficult to evaluate. From Eq. 5.8, the equivalent mass is computed from $A_1 = k_b e_b = 4\rho_b \omega_b e / (3\rho_0 c_0) = 10.55$. Note that the equivalent thickness of the beam is $e_b = 0.81\text{m}$. It corresponds to the thickness of air that would have to be set in motion to obtain the same effect. This shows the interest of vibrating a solid part when we want to tackle the low frequencies. If we simply consider that the plate is rotating and that the stiffness comes from the deformation of the two arms of width $b = 1\text{mm}$ and length $a = 4\text{ mm}$ at the base of the plate. The resonance frequency is obtained by $\omega_1^2 = 0.5(E/\rho_b)be^2/(Bal^3)$ where E is the Young modulus, B is the width of the plate and $l = l_1 + l_2$ is the length of the plate. Using the dimensions and characteristics of the cut composite plate, the predicted frequency is equal to $f_1 = 1080\text{ Hz}$ while the measured frequency is $f_1 = 710\text{ Hz}$. This difference comes from the crudeness of the model used to predict stiffness. Nevertheless, this model allows us to see the main parameters influencing this resonance frequency and to compare it with that of a cantilever beam of the same dimensions without I-cuts, which is here given by $\omega^2 = 1.02(E/\rho_b)e^2/l^4$ leading to a frequency $f = 2680\text{ Hz}$. The structural damping is more complex to evaluate and is deduced from the vibrometer measurements $\delta_1 = 0.01$.

The values of the three parameters for the second mode are deduced directly from the vibrometer measurements: $\delta_2 = 1.25$, $A_2 = 150$, $f_2 = 3730\text{ Hz}$. The measured impedance Z_b (in blue) and the calculated impedance (in red) are shown in Figure 5.8 which indicates a correct agreement between these two values, especially in the vicinity of resonances where

the imaginary part of Z_b becomes zero.

Acoustic measurements

Using the four microphones described in Fig. 5.6, the reflection coefficient r can be obtained by an over-determined separation of incident and reflected waves by means of a least-squares method. From r , the absorption coefficient $\alpha = 1 - |r|^2$ and the impedance $Z = (1+r)/(1-r)$ can be easily computed. The measured device consists of the composite plate where the cantilever beam with two I-cuts cuts associated with a closed cavity of the same cross-section as the incident tube (diameter 30 mm) and length 30 mm.

To predict the impedance of this device, the Eq. 5.11 is used. In this equation, the beam impedance Z_b is deduced from the vibration measurements described in the previous subsection. The cavity impedance Z_c can be computed from the Eq. 5.10 with $W = 30$ mm. The most tricky part to estimate is the acoustic impedance of the slit Z_s . Indeed, the slit resistance is extremely sensitive to the width of the slit s . If we use the relation $R_s = 12\mu e / (\rho_0 c_0 s^2)$ we see that this resistance is inversely proportional to the square of s . In addition if one relates this impedance to the incident surface $R = S_i / S_s R_s$, where $S_i = l_s s$ and $l_s = 88$ mm the total length of the slits, we see that the resistance R is proportional to s^{-3} . The machining process of these micro-slits results in a slight conicity of the slit which therefore does not have a constant width s . On the height of $e = 500\mu\text{m}$, it is estimated that the width goes from $50\mu\text{m}$ (see the photo under the microscope on Fig. 5.6) at the narrowest to $100\mu\text{m}$ on the other side of the plate. For a constant width $s = 50\mu\text{m}$ the resistance is $R = 16$ while for $s = 100\mu\text{m}$ the resistance is $R = 2$. It is therefore difficult to say more than $2 < R < 16$ and the exact value of R had to be experimentally adjusted.

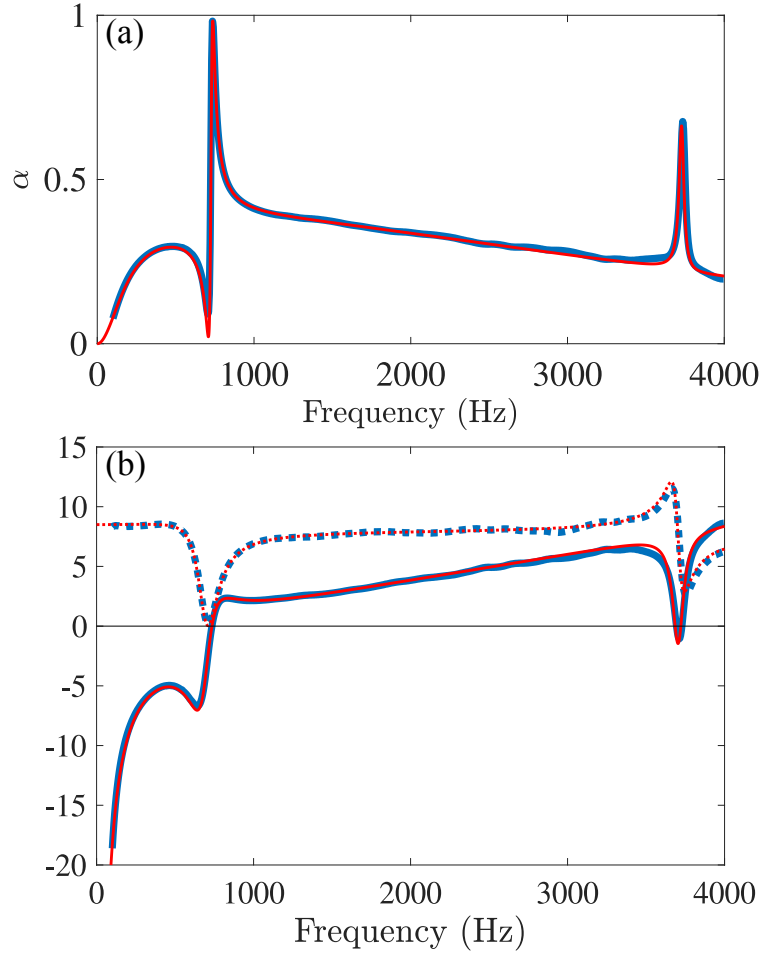


Figure 5.9 – (a) Absorption coefficient and (b) impedance. Comparison between experimental results and model

The absorption coefficient α and impedance Z that were measured are plotted with a wide blue line in Fig. 5.9. What happens on these curves in the vicinity of the first resonance frequency of the beam is very similar to what is shown in Fig. 5.2. In particular we can see that the maximum absorption frequency (735 Hz) is slightly higher than the first resonance frequency of the beam (710 Hz) which corresponds to a very low absorption. We also note that the real part of the impedance (dashed in Fig 5.9b) tends at low frequency towards a constant which is the resistance R . We can therefore estimate the value of the resistance $R = 8.5$.

At this stage, all the parameters that describe the measured device are known and the impedance and absorption coefficient can be calculated (thin red curve on figure 5.9). This suggests that the proposed model takes into account the main effects that occur in such a device and that it is possible to size such a system for specific uses.

5.5.2 Grazing incidence measurements

A second sample, to be placed in the wall of a rectangular duct, was made from the same composite material plate and with exactly the same micro-cutting geometry. This sample is made in a plate of $120 \times 50 \text{ mm}^2$ where 3 rows of 5 beams have been micro-cut, in blue on Fig. 5.1. This plate was glued on a support (in black in Fig. 5.1) with 15 cavities of section $15 \times 22 \text{ mm}^2$ and height $W = 30 \text{ mm}$.

During the measurements, this sample of 15 beams is flush mounted on the wall of a waveguide with a rectangular section. The height of the channel is $H = 40 \text{ mm}$ while the transverse dimension is 50 mm , which means that the sample covers the entire width of the channel. This duct facility has already been introduced in [76] . The acoustic waves are generated by two compression chambers which can be placed either upstream, or downstream, of the test section. A sinusoidal sweep ranging from 200 Hz to 4000 Hz with a step of 5 Hz is used.

The sound pressure in the duct is recorded by two sets of three flush-mounted microphones located upstream (u_i) and downstream (d_i) of the test section, where $i = 1$ indicates the microphone located the closest to the test section. The positions of the microphones are $x_{u_1} - x_{u_2} = x_{d_2} - x_{d_1} = 30 \text{ mm}$, $x_{u_1} - x_{u_3} = x_{d_3} - x_{d_1} = 175 \text{ mm}$, and both u_1 and d_1 are placed 113 mm away from the sample. All the microphones are calibrated relatively to u_1 . At each frequency step of the sine sweep, the acoustic pressure on each microphone is calculated by averaging the pressure value over 400 cycles without flow, and over 1000 cycles with flow.

This allows an overestimated determination of the incident and reflected waves on both sides of the sample. The elements of the scattering matrix of the sample, namely the reflection and transmission coefficients (r^\pm, t^\pm) defined for incident plane waves coming from upstream (r^+, t^+) and downstream (r^-, t^-) of the sample, are computed. To obtain these four coefficients, two different acoustic states are needed. The first one is obtained by placing the compression chambers upstream of the resonators, the second one by placing them downstream. More details about this measurement technique, for the case of a cylindrical duct, can be found in [65].

Once again, this measuring system makes it possible to control the acoustic level of the incident wave. Several levels were tested but no non-linear effects were detected.

To predict the effect of the sample on propagation, two separate actions are required. The first one is to calculate the equivalent impedance of the sample. The second one is to predict the propagation in the duct in the presence of an acoustically treated wall.

The prediction of impedance is relatively easy since the impedances of the beam Z_b and the slits Z_s are identical to the case in normal incidence since it is the same material and geometry. Similarly, the cavity having the same depth W , the cavity impedance Z_c is also unchanged. The only things that change in Eq. 5.11 are the incident sections $S_i = 120 \times 50 / 15 \text{ mm}^2$ and the cavity section $S_c = 15 \times 22 \text{ mm}^2$.

To predict the propagation with an impedance wall, a numerical simulation is carried out. To this end, a multimodal method is used to calculate the linearized two-dimensional lossless problem. This method has already been described in detail elsewhere [68, 69, 70] and therefore only a few points are merely reported.

The linear propagation of small perturbations can be described by the linearized Euler and continuity equations. The multimodal method is used and the perturbations are therefore expressed as a linear combination of acoustic transverse modes. These modes and wave numbers are computed on uniform segments using a finite difference method by discretizing the equations in the transverse y -direction. Here, the modes must be calculated in the rigid

duct and in the lined part wall. The scattering matrix of the sample is found by matching the modes at the discontinuities at each ends of the sample.

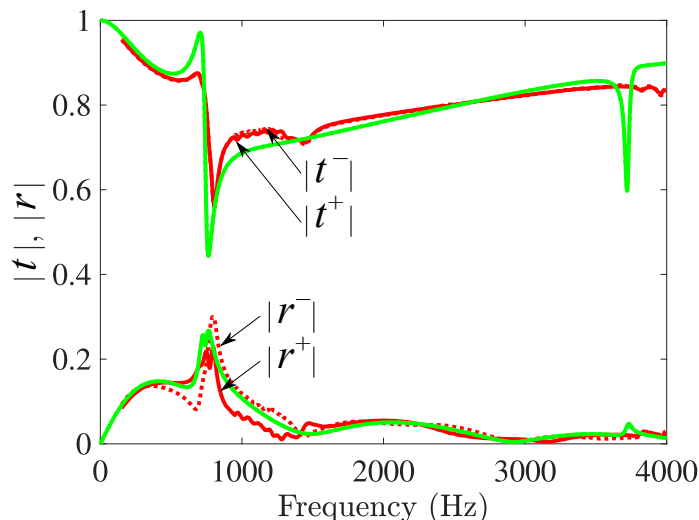


Figure 5.10 – *Transmission and reflection coefficients of the lined sample . Comparison between experimental (red curves) and model (green curves) results*

The comparison between the predict and measured transmission and reflection coefficient are depicted in Fig. 5.10. Due to reciprocity, the measured transmission coefficients in both directions are identical. Conversely, the reflection coefficients t^+ and t^- differ slightly. This seems to indicate an inhomogeneity of the different beams which would not all react in the same way. This may be due to the bonding of the plate to its support, which may not be exactly identical at every location. The comparison between predicted and measured values of transmission and reflection is relatively correct around the first resonance of the plate. It can be noted that the hypothesis that one can substitute a discrete set of cells, of fairly large size, with a distributed and homogeneous impedance can quickly find its limit when the frequency increases. Moreover, the implicit assumption that cells do not acoustically interfere with each other is also very questionable.

A striking effect is the disappearance of the second high-frequency peak (near $f_2 = 3730$ Hz). As $f=4000$ Hz corresponds to the cut-off frequency of the second propagative mode in

the rigid conduit that our setup does not allow to characterize, it was not possible to know if this second peak was rejected at higher frequency or if it simply disappeared. As mentioned above, for these frequencies the length of a cell is of the order of a quarter of the wavelength and the hypothesis of uniformity of impedance is no longer valid.

In spite of its approximations, an impedance homogenization model gives good results at low frequencies and makes it possible to understand the main effects of treatments with vibrating plates and micro slits on the propagation and reflection of a duct having such a material.

5.5.3 Effect of flow

The implementation of acoustic treatment in the wall of a duct allows to study the effect of a flow on its acoustic behavior. For this purpose, the duct installation is connected to a rotating lobe blower that can provide a mean velocity of up to 85 m/s. The flow velocity is measured at the center of the duct downstream of the test section by a Pitot tube connected to a differential pressure sensor. This measurement gives the maximum value of the flow velocity in the duct section. It is then multiplied by 0.8 in order to obtain the value of the average velocity and the Mach number M [64]. The measurements shown in Fig. 5.11 were performed at a Mach number of 0.25.

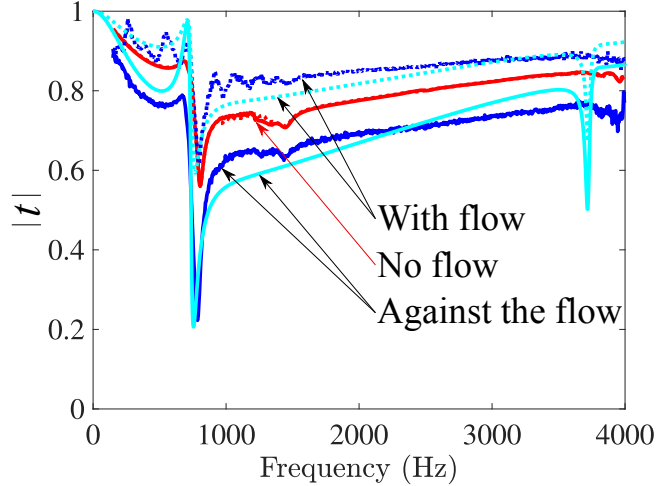


Figure 5.11 – *Transmission coefficient of the lined sample without and with flow ($M=0.25$). Comparison between experimental (blue and red curves, for $M=0$ and 0.25 , respectively) and model (cyan curves, $M=0.25$) results*

The presence of an assumed uniform flow is also fairly easy to take into account in propagation modeling. To do this, it is necessary to add convection terms to the equations used. It is also necessary to modify the boundary condition that applies to the wall with impedance. Here we have used the classical condition of continuity of pressure and normal displacement also called Ingard-Myers condition. Finally, it is necessary to apply a special mode matching between the duct with impedance and the rigid duct that takes into account this Ingard-Myers condition[77, 78, 79].

The fairly good agreement between the experimental results and the model results, shows that the flow does not significantly change the value of the impedance of the material. The effect of the flow is therefore mainly due to convective effects both in the propagation itself and in Ingard-Myers condition.

5.6 Vibrometer Results

As shown above for the normal propagation case, vibrometric analysis have been carried out also for the transversal propagation configuration. All three sets of cantilever beams

described in table 5.1 have been tested. In figure 5.12, the composite beams together with the mounting chassis which is used to lock it in position in the waveguide is shown on the left (each beam outlined with a dashed red line). On the right, the corresponding absolute velocity values around the first resonance frequency is shown for each beam, as retrieved in Matlab. It is possible to appreciate that, at this frequency, the major part of the beams react with a large velocity (i.e. their first natural frequencies are close to each other and to the calculated one). On the other hand, the three first beams on the first line and the first beam on the second line shown a much smaller velocity magnitude ($o(10^{-1})$ smaller). This is due, most probably, to errors in the manufacturing procedure, as it is noticeable how these beams react with a flexural mode whose rigidity is not constant along the transversal dimension.

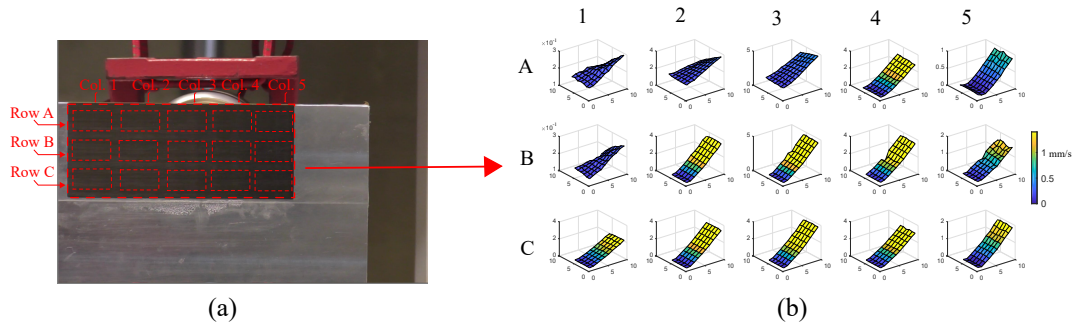


Figure 5.12 – *Vibrating Beam elements (as outlined by the rectangular dashed areas in (a)) vertical displacement around the first natural frequency. It is possible to appreciate how the displacement is not maximal for all the beam, suggesting a difference in the beams assembly.*

In figure 5.13, the velocity transfer function is shown for the same beams, organized in lines: the first, second and third lines are shown in figure 5.13-a,b,c respectively. It is possible to appreciate how these beams have a total different first natural frequency around 1.5 kHz. Furthermore, they don't show any significant reaction around the second natural frequency around 4 kHz, where all the other beams seem to be gathered around (still, it is possible to notice how, at this frequency, it is more difficult to outline one single peak).

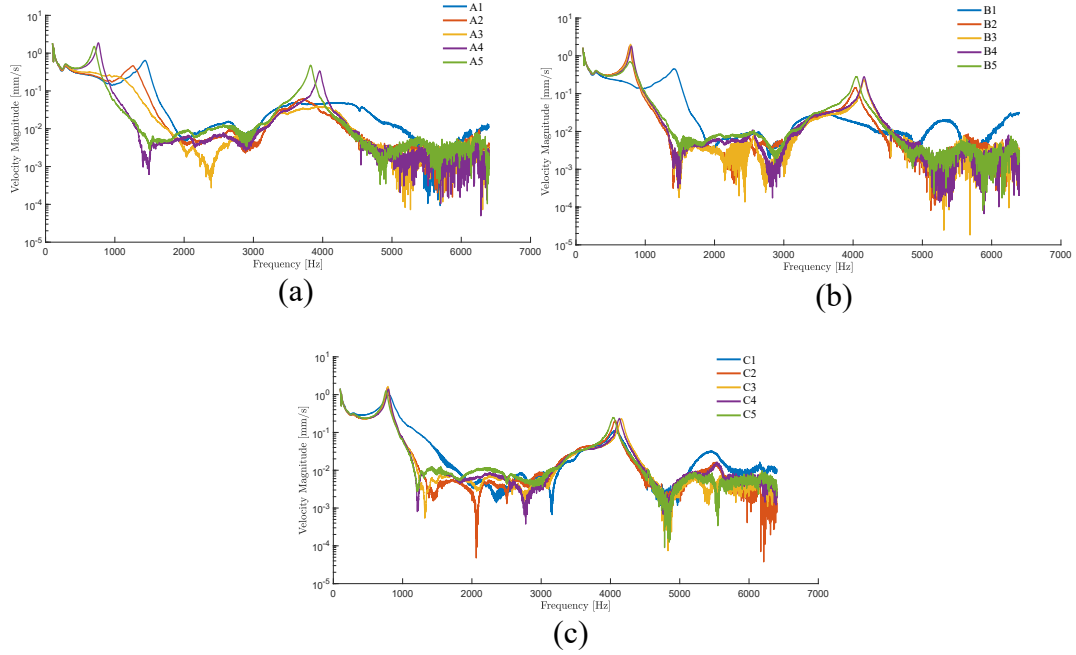
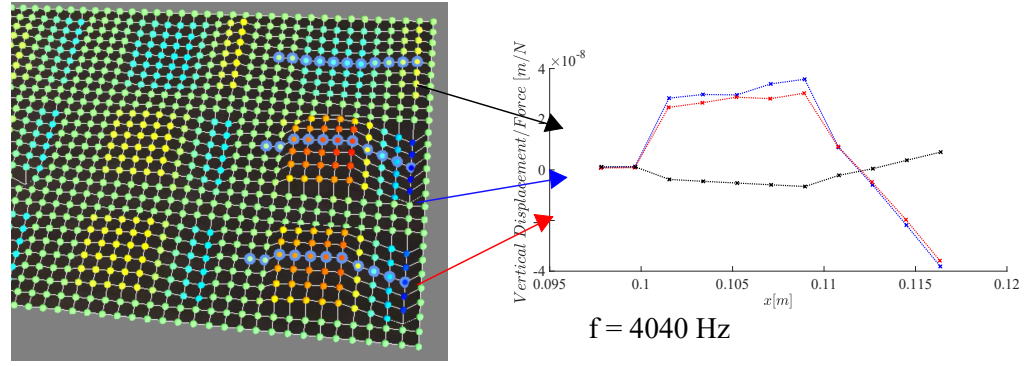
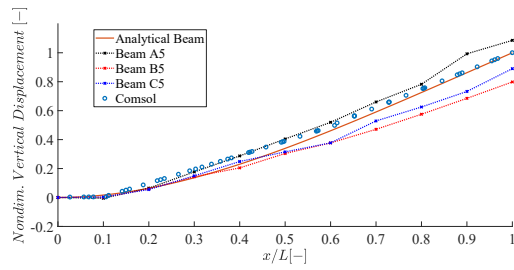


Figure 5.13 – *Velocity magnitude frequency response of the composite vibrating beam elements*

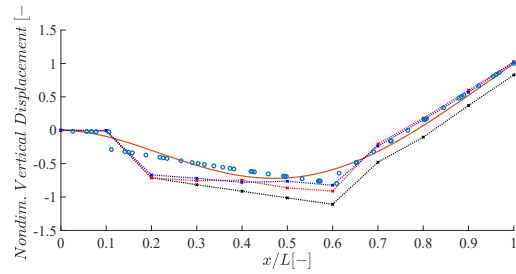
Finally, a comparison between the computed eigemodes for a cantilever beams and the displacements obtained for the first two composite beam eigenmodes is shown in figure 5.14. It is possible to see that while the cantilever model recovers a good agreement in the second half (w.r.t. the "I" cut) of the beam, it underestimates the displacement of the first half of the beam which will result in an overall greater rigidity of the structure.



(a)



(b)



(c)

Figure 5.14 – Global (left) and extrapolated (right) displacement transfer functions for three sample beams (A5, B5, C5) from the double "I" composite vibrating beam elements (a). Comparison of a cantilever beam analytical (solid lines) and COMSOL produced (blue circles) eigenmodes with the nondimensionalised displacement of the same sample beams (A5, B5, C5) for the first (b) and second (c) eigenmodes

Chapter Six

Conclusions

In this thesis, the nature of the aero-acoustic interaction has been investigated for different novel materials and systems configurations. This has been done by the means of an experimental, a numerical and simple theoretical approaches. Aside from Chapter 2, where the experimental setup and techniques adopted are described, three main chapters compose this manuscript. In each, an aeroacoustic problem has been investigated.

In Chapter 3, the acoustic propagation along a corrugated plate inside a square waveguide has been investigated, with and without a grazing flow present. Without flow, the acoustic propagation along the corrugated plate is almost unaffected by the corrugations and therefore similar to the one of a rigid tube, with a slightly lower transmission coefficient due to enhanced visco-thermal losses. When the flow is present, the behaviour changes drastically. The transmission along and against the flow direction are not identical anymore. This is due to the loss of reciprocity due to convection effects, but it is also possible to notice oscillations of the transmission curves around the no-flow values. Therefore, it is possible to identify "gain" ("loss") areas, where transmission is higher (resp., lower) than the no flow case. At four of these characteristic frequencies, Laser Doppler Velocimetry (LDV) measurements have then been carried out. This technique allows us to investigate inside a single corrugation cavity and resolve the main fluid-dynamic and acoustic quantities. What is pos-

sible to see is that coherent vorticity structures show a rather complex distribution when compared to deep cavity configurations, which makes it difficult to isolate completely the acoustic sound production and absorption zones. These structures depend on the frequency and the longitudinal position along the cavity, which explain the gain/loss mechanism which is seen in the transmission curves.

In chapter 4, an investigation about the shielding of metamaterials from flow has been carried out. This investigation has been inspired by the latest research about metamaterials, where new ways to manipulate sound waves are investigated. Furthermore, in the aeronautics field, these solutions have to deal with the presence of an external flow which has a strong influence, especially when these materials are porous or, like in cloaking devices, they have to be shielded from flow but being transparent to acoustic waves. Therefore, a "magic" layer is often introduced so to allow acoustics to pass through while suppressing flow effects. As a practical realization of such a layer, a kevlar sheet is often suggested based on its application in wind tunnels. However, we show that, for the metamaterial we chose, the effect of flow is clearly represented by a loud whistling around its resonance frequency. If we put a kevlar layer covering such metamaterial, flow effects are in fact reduced, but the layer is not acoustically neutral: the whistling doesn't appear anymore due to an introduced acoustic resistance and the behaviour of the metamaterial is completely altered. This proves that a kevlar layer cannot be considered to be an acoustically neutral layer which was advertised.

In chapter 5, the behaviour of vibrating beams associated with micro-slits has been investigated. The investigated beams are obtained by $50 \mu m$ laser cuts cuts from a thin composite plate. Also, two "I" cuts have been realized orthogonally to the beam longitudinal direction so to make the fixation less rigid (the first cut) and to induce a bi-articulated behaviour (second cut) with two degrees of freedom and a low stiffness. A simple analytical model is proposed to predict the behaviour of the blade. Then, a parametric study is

performed in order to design experimental samples. An experimental campaign was carried out to obtain comparison with this model: first experiments were conducted in an impedance tube, where both the acoustic in the duct and the vibration of the beam are measured. The closeness of the experimental and the analytical results indicates that the right physical phenomena have been identified. Finally, a last set of experiments performed in a grazing flow facility gives hint about the possible application of such acoustic treatments to aircraft noise reduction.

Future works will be focused on better understanding the difference between the behaviours of these metamaterials, namely the way the hydrodynamic interaction works inside the shear layer above a corrugated plate or a vibrating beam. This better understanding should allow the development of new beams or better metamaterials which would be able to exploit the aero-acoustic interaction in a favourable way and improve their subwavelength performances.

APPENDIX

Appendix One

Technical Demonstrator

As foreseen by the ITN H2020 SmartAnswer Training Programme, a technical demonstrator was planned and developed by the Earl Stage Researchers (ESR). The demonstrator's objective is to immediately show all the areas of research where the project has focused and its relative outcomes. Therefore, it was decided for the demonstrator to be a wind tunnel inside where different airfoils could be put. These airfoils could interact with the vortex shed by a rod put a little upstream: the effects of aeroacoustic would create a large band noise which would propagate towards the downstream exit of the wind tunnel. After the airfoils, three different systems of noise reduction devices were conceived to work alternatively: a passive liner, an active liner and a metamaterial system. These would concentrate on absorbing the sound emitted at different bands inside the aforementioned aeroacoustic spectrum.

The main area of intervention regarding this thesis was the development of passive liners: these, were to be thinkered in order to reduce a broadband noise in the $1 - 3 \text{ Hz}$ spectrum. The main and most proficient response to the need of acoustic passive liner have been the Single (and Double) Degree of Freedom perforated plates. These are perforated plates with different amounts of permeability (i.e. percentage of open perforated area) backed up by a perpendicular, partitioned, layer of cells. Usually, these cells are formed by honeycomb sheet, where each cell is divided by an impervious wall. Also, sometimes between the plate and the backing up cavity a wiremesh or an equivalent resistive material is put in order to

tune the impedance to the ambient conditions.

Regarding this kind of passive liners, one widely used reference model is the one proposed by Guess [1]. This model takes into account the effects of the plate and the underlying cavities through four parameters: the permeability σ , the thickness of the plate t , the diameter of the perforated holes d and the depth of the cavities. Furthermore, the effect of flow and the relative nonlinear effects are taken into account by the means of the Mach number $M = u/c$ and a correcting factor $t' = t/d$. Then, after several computations, Guess summarizes the total impedance real and imaginary part of such a liner, respectively, as follows:

$$\begin{aligned} \theta &= \frac{\sqrt{8\nu\omega}}{\sigma c} \left(1 + \frac{t}{d}\right) + \frac{\pi}{2\sigma} \left(\frac{d}{\lambda}\right)^2 + \frac{(1 - \sigma^2)}{\sigma} \left(\frac{|u_0|}{c} + sM\right) \\ \chi &= \frac{\omega(t + \delta)}{\sigma c} + \frac{\sqrt{8\nu\omega}}{\sigma c} \left(1 + \frac{t}{d}\right) - \cot \frac{\omega H}{c} \end{aligned} \quad (\text{A.1})$$

where ω , c , λ are respectively, the angular frequency, the sound speed and the acoustic wavelength. The third term in the above real part impedance equation represents the influence of large sound amplitude and free stream flow in nonlinearities of the liner. The term ν is the cinematic viscosity and s is a correlating factor which in our case is $s = 0.3$. Finally, the term δ is a correction end for the orifice diameter, which reads

$$\delta = 8/3 \frac{d(1 - 0.7\sqrt{\sigma})}{(1 + 305M^3)} \frac{1 + 5 * 10^3 M^2}{1 + 10^4 M^2} \quad (\text{A.2})$$

Then, in order to carry out the design of the passive element inside the demonstrator, two steps were required: deriving the optimal impedance relative to the geometrical and ambient conditions followed up by the matching of this value with the one obtained by the liner model. A summary of the process is shown as a chart in Figure A.1

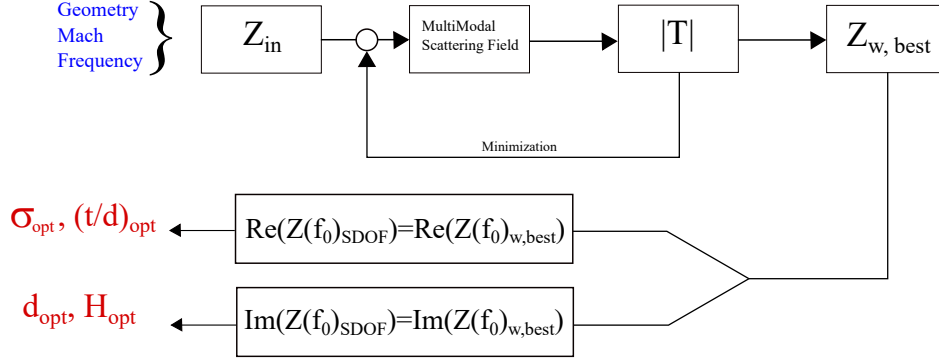


Figure A.1 – *Finding of the best wall impedance and optimal SDOF impedance match*

Regarding the first process step, a multimodal method was used in order to retrieve the scattering matrix before, after and along the treated wall. Defining the number of modes which would model the pressure field along the lined section, it is possible to retrieve this once an impedance value is defined in input. As the scattering matrix is then known, the transmission, reflection and absorption coefficients can then be obtained. In order to obtain the optimal impedance, such process can be looped until a cost function is minimized (e.g. the transmission coefficient at a few desired frequency points) by starting with a well first guess impedance value like Cremer's impedance. Once the optimal impedance value is obtained, we can try to match it by the above mentioned Guess model at a desired frequency. In order to do so, we first match the real part rewritten in a simplified fashion as follows:

$$\theta = \frac{\sqrt{8\nu\omega}}{\sigma c} \left(1 + \frac{t}{d}\right) + \frac{(1 - \sigma^2)}{\sigma} (sM) \quad (\text{A.3})$$

because the low sound level introduces only negligible nonlinearities and the term $\frac{\pi}{2\sigma} \left(\frac{d}{\lambda}\right)^2 \ll \frac{\sqrt{8\nu\omega}}{\sigma c} \left(1 + \frac{t}{d}\right)$ so that we can exclude it in the shooting guess and update it afterwards. From the matching of the real part we retrieve then the optimal σ value and t/d ratio. Then, once updated the real and imaginary part with these values, we can match the imaginary part of the impedance by varying the thickness H and hole diameter d obtaining the optimal

values for these parameters. At the end of the process we are able to match the impedance of our SDOF liner at the desired frequency. In Figure A.2, the real and imaginary part of the impedance are shown: in blue, the optimized best wind tunnel impedance (which is very close to the Cremer value) while in red the SDOF one.

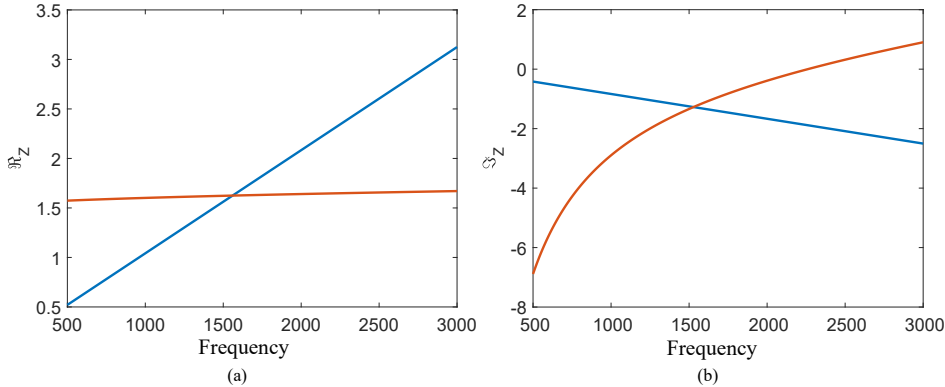


Figure A.2 – *Real part (a) and Imaginary part (b) of the best wall impedance (blue) and SDOF optimized (red) impedance*

Bibliography

- [1] A. W. Guess. “Calculation of perforated plate liner parameters from specified acoustic resistance and reactance”. In: *Journal of Sound and Vibration* 40.1 (1975), pp. 119–137. ISSN: 10958568. DOI: [10.1016/S0022-460X\(75\)80234-3](https://doi.org/10.1016/S0022-460X(75)80234-3).
- [2] D. Li, D. Chang, and B. Liu. “Enhancing the low frequency sound absorption of a perforated panel by parallel-arranged extended tubes”. In: *Applied Acoustics* 102 (2016), pp. 126–132. ISSN: 1872910X. DOI: [10.1016/j.apacoust.2015.10.001](https://doi.org/10.1016/j.apacoust.2015.10.001).
- [3] Frank Simon. “Long Elastic Open Neck Acoustic Resonator for low frequency absorption”. In: *Journal of Sound and Vibration* 421 (2018), pp. 1–16. DOI: [10.1016/j.jsv.2018.01.044](https://doi.org/10.1016/j.jsv.2018.01.044). URL: <https://hal.archives-ouvertes.fr/hal-01870188>.
- [4] J. P. Groby et al. “The use of slow waves to design simple sound absorbing materials”. In: *Journal of Applied Physics* 117.12 (2015), pp. 1–9. ISSN: 10897550. DOI: [10.1063/1.4915115](https://doi.org/10.1063/1.4915115).
- [5] U. Ackermann and H. Fuchs. “Technical Note: Noise Reduction in an Exhaust Stack of a Papermill”. In: *Noise Control Engineering Journal - NOISE CONTR ENG J* 33 (Sept. 1989). DOI: [10.3397/1.2827743](https://doi.org/10.3397/1.2827743).
- [6] W. Frommhold, H.V. Fuchs, and S. Sheng. *Acoustic Performance of Membrane Absorbers*. 1994. DOI: [10.1006/jsvi.1994.1091](https://doi.org/10.1006/jsvi.1994.1091).
- [7] G. Ma et al. “Acoustic metasurface with hybrid resonances”. In: *Nature Materials* 13.9 (2014), pp. 873–878. ISSN: 14764660. DOI: [10.1038/nmat3994](https://doi.org/10.1038/nmat3994).

- [8] H. Lissek, R. Boulandet, and R. Fleury. “Electroacoustic absorbers: Bridging the gap between shunt loudspeakers and active sound absorption”. In: *The Journal of the Acoustical Society of America* 129.5 (2011), pp. 2968–2978. DOI: [10.1121/1.3569707](https://doi.org/10.1121/1.3569707).
- [9] M. Galland, B. Mazeaud, and N. Sellen. “Hybrid passive/active absorbers for flow ducts”. In: *Applied Acoustics* 66 (June 2005), pp. 691–708. DOI: [10.1016/j.apacoust.2004.09.007](https://doi.org/10.1016/j.apacoust.2004.09.007).
- [10] R. Boulandet et al. “Duct modes damping through an adjustable electroacoustic liner under grazing incidence”. In: *Journal of Sound and Vibration* 426 (2018), pp. 19–33. DOI: [10.1016/j.jsv.2018.04.009](https://doi.org/10.1016/j.jsv.2018.04.009).
- [11] Y. Aurégan and M. Leroux. “Experimental evidence of an instability over an impedance wall in a duct with flow”. In: *Journal of Sound and Vibration* 317.3-5 (2008), pp. 432–439. ISSN: 0022460X. DOI: [10.1016/j.jsv.2008.04.020](https://doi.org/10.1016/j.jsv.2008.04.020).
- [12] Y. Aurégan, M. Farooqui, and J. Groby. “Low frequency sound attenuation in a flow duct using a thin slow sound material”. In: *The Journal of the Acoustical Society of America* 139.5 (2016), EL149–EL153. ISSN: 0001-4966. DOI: [10.1121/1.4951028](https://doi.org/10.1121/1.4951028).
- [13] E. J. Brambley. “Well-Posed Boundary Condition for Acoustic Liners in Straight Ducts with Flow”. In: *AIAA Journal* 49.6 (2011), pp. 1272–1282. ISSN: 0001-1452. DOI: [10.2514/1.J050723](https://doi.org/10.2514/1.J050723).
- [14] J. M. Roche. “Simulation numérique des propriétés acoustiques de cavités résonantes en présence d’écoulement”. PhD thesis. Université du Maine, Le Mans, 2011.
- [15] G. Palma et al. “Acoustic metamaterials in aeronautics”. In: *Applied Sciences (Switzerland)* 8.6 (2018), pp. 1–18. ISSN: 20763417. DOI: [10.3390/app8060971](https://doi.org/10.3390/app8060971).
- [16] H. Chen and C. T. Chan. “Acoustic cloaking in three dimensions using acoustic metamaterials”. In: *Applied Physics Letters* 91.18 (2007), pp. 1–4. ISSN: 00036951. DOI: [10.1063/1.2803315](https://doi.org/10.1063/1.2803315).

- [17] S.P.C. Belfroid, R.J. Swindell, and N. Kitney. “Flow-Induced Pulsations due to Flexible Risers”. In: *Proceedings of Offshore Technology Conference*. 2009.
- [18] M. Åbom. “Measurement of the scattering-matrix of acoustical two-ports”. In: *Mechanical systems and signal processing* 5.2 (1991), pp. 89–104.
- [19] H. Lin, D. Hsu, and J. Su. “Particle Size Distribution of Aromatic Incense Burning Products”. In: *International Journal of Environmental Science and Development* 6.11 (2015), pp. 857–860. ISSN: 20100264. DOI: [10.7763/IJESD.2015.V6.712](https://doi.org/10.7763/IJESD.2015.V6.712).
- [20] M. Hamdi et al. “Comparison of different tracers for PIV measurements in EHD air-flow”. In: *Experiments in Fluids* 55.4 (2014). ISSN: 07234864. DOI: [10.1007/s00348-014-1702-z](https://doi.org/10.1007/s00348-014-1702-z).
- [21] A. Melling. *Tracer Particles and Seeding for Particle Image Velocimetry*. Meas. Sci. Technol pp. 1406-1416, 1997.
- [22] A.T. Hjelmfel and L.F. Mockros. “Motion of Discrete Particles in a Turbulent Fluid”. In: *Applied Scientific Research* 16.1 (1966), pp. 149–161.
- [23] D. C. Rife and R. R. Boorstyn. “Single-Tone Parameter Estimation from”. In: *Information Theory, IEEE Transactions on* 20.5 (1974), pp. 591–598. ISSN: 15579654. DOI: [10.1109/TIT.1974.1055282](https://doi.org/10.1109/TIT.1974.1055282).
- [24] Jean-Christophe Valière. *Acoustic Particle Velocity Measurements Using Lasers: Principles, Signal Processing and Applications*. John Wiley & Sons, 2014.
- [25] F. S. Crawford. “Singing Corrugated Pipes”. In: *The Journal of the Acoustical Society of America* 58.S1 (1975), S2. ISSN: 00029505. DOI: [10.1119/1.1987673](https://doi.org/10.1119/1.1987673).
- [26] D. Rockwell and E. Naudascher. “Review - Self-Sustaining Oscillations of Flow Past Cavities”. In: *Journal of Fluids Engineering* 100.June (1978), p. 14. ISSN: 00982202. DOI: [10.1115/1.3448624](https://doi.org/10.1115/1.3448624).

- [27] Y. Nakamura and N. Fukamachi. “Sound generation in corrugated tubes”. In: *Fluid Dynamics Research* 7.5 (1991), pp. 255–261. ISSN: 0169-5983. DOI: [10.1016/0169-5983\(91\)90018-E](https://doi.org/10.1016/0169-5983(91)90018-E).
- [28] V. F. Kopiev, M. A. Mironov, and M. A. Yakovets. “Flow noise in a corrugated pipe in terms of the theory of instability waves”. In: *Acoustical Physics* 61.5 (2015), pp. 499–503. ISSN: 10637710. DOI: [10.1134/S1063771015050115](https://doi.org/10.1134/S1063771015050115).
- [29] “Admittance of a groove on a rigid surface under a grazing flow”. In: *Acoustical Physics* 49.1 (2003), pp. 75–80. ISSN: 10637710. DOI: [10.1134/1.1537391](https://doi.org/10.1134/1.1537391).
- [30] G. Nakiboğlu et al. “On the whistling of corrugated pipes: effect of pipe length and flow profile”. In: *Journal of Fluid Mechanics* 672 (2011), pp. 78–108.
- [31] E. Salt et al. “Aeroacoustic sources generated by flow–sound interaction in a T-junction”. In: *Journal of Fluids and Structures* 51 (2014), pp. 116–131. ISSN: 0889-9746. DOI: [10.1016/j.jfluidstructs.2014.08.005](https://doi.org/10.1016/j.jfluidstructs.2014.08.005).
- [32] D. Tonon et al. “Whistling of a pipe system with multiple side branches: Comparison with corrugated pipes”. In: *Journal of Sound and Vibration* 329.8 (2010), pp. 1007–1024. ISSN: 0022-460X. DOI: <https://doi.org/10.1016/j.jsv.2009.10.020>.
- [33] A. A. Shaaban and S. Ziada. “Fully developed building unit cavity source for long multiple shallow cavity configurations”. In: *Physics of Fluids* 30.8 (2018). ISSN: 10897666. DOI: [10.1063/1.5041751](https://doi.org/10.1063/1.5041751).
- [34] M.S. Howe. “Contributions to the theory of aerodynamic sound, with application to excess jet noise and the theory of the flute”. In: *Journal of Fluid Mechanics* 71.04 (1975), pp. 625–673.
- [35] J. C. Bruggeman et al. “Self-sustained aero-acoustic pulsations in gas transport systems: Experimental study of the influence of closed side branches”. In: *Journal of*

- Sound and Vibration* 150.3 (1991), pp. 371–393. ISSN: 10958568. DOI: [10.1016/0022-460X\(91\)90893-O](https://doi.org/10.1016/0022-460X(91)90893-O).
- [36] P.A. Nelson, N.A. Halliwell, and P.E. Doak. “Fluid dynamics of a flow excited resonance, Part II: Flow acoustic interaction”. In: *Journal of sound and vibration* 91.3 (1983), pp. 375–402.
- [37] J.C. Bruggeman et al. “Flow induced pulsations in gas transport systems: analysis of the influence of closed side branches”. In: *Journal of Fluids Engineering: Transactions of the ASME* 111.4 (1989), pp. 484–491.
- [38] J. W. Elliott. “Corrugated Pipe Flow”. In: *Lecture Notes on the Mathematics of Acoustics*, pp. 207–222.
- [39] J. Bruggeman. “Flow induced pulsations in pipe systems”. In: *Ph.D. Thesis Technische Hogeschool, Eindhoven (Netherlands)*. (1987). DOI: [10.6100/IR264848](https://doi.org/10.6100/IR264848).
- [40] Joachim Golliard, Yves Aurégan, and Thomas Humbert. “Experimental study of plane wave propagation in a corrugated pipe: Linear regime of acoustic-flow interaction”. In: *Journal of Sound and Vibration* 472 (2020), p. 115158. ISSN: 0022-460X. DOI: <https://doi.org/10.1016/j.jsv.2019.115158>.
- [41] A. Michalke. “On spatially growing disturbances in an inviscid shear layer”. In: *Journal of Fluid Mechanics* 23.3 (1965), 521–544. DOI: [10.1017/S0022112065001520](https://doi.org/10.1017/S0022112065001520).
- [42] M. S. Howe. *Interaction of sound with solid structures*. 2010, pp. 317–430. ISBN: 9780511662898. DOI: [10.1017/cbo9780511662898.006](https://doi.org/10.1017/cbo9780511662898.006).
- [43] D’Elia Massimo. *Dataset for H2020 Smartanswer Corrugations Experiment*. Mar. 2021. DOI: [10.5281/zenodo.5702563](https://doi.org/10.5281/zenodo.5702563). URL: <https://doi.org/10.5281/zenodo.5702563>.
- [44] T. V. Karman. “Mechanical similitude and turbulence”. In: 1931.
- [45] Hermann Schlichting and Klaus Gersten. *Boundary-Layer Theory*. Jan. 2017. ISBN: 978-3-662-52917-1. DOI: [10.1007/978-3-662-52919-5](https://doi.org/10.1007/978-3-662-52919-5).

- [46] G. Kooijman, A. Hirschberg, and J. Golliard. “Acoustical response of orifices under grazing flow: Effect of boundary layer profile and edge geometry”. In: *Journal of Sound and Vibration* 315.4-5 (2008), pp. 849–874.
- [47] C.L. Morfey. “Acoustic energy in non-uniform flows”. In: *Journal of Sound and Vibration* 14.2 (1971), pp. 159–170.
- [48] S. A. Elder. “The mechanism of sound production in organ pipes and cavity resonators”. In: *Journal of the Acoustical Society of Japan (E)* 13.1 (1992), pp. 11–23.
- [49] M. S. Howe. *Acoustics of fluid-structure interactions*. Cambridge university press, 1998.
- [50] M. S. Howe. “Mechanism of sound generation by low Mach number flow over a wall cavity”. In: *Journal of Sound and Vibration* 273.1-2 (2004), pp. 103–123. ISSN: 0022460X. DOI: [10.1016/S0022-460X\(03\)00644-8](https://doi.org/10.1016/S0022-460X(03)00644-8).
- [51] G. Ma and P. Sheng. “Acoustic metamaterials: From local resonances to broad horizons”. In: *Science advances* 2.2 (2016), e1501595.
- [52] S. A. Cummer, J. Christensen, and A. Alù. “Controlling sound with acoustic metamaterials”. In: *Nature Reviews Materials* 1.3 (2016), p. 16001.
- [53] G. Palma et al. “Acoustic metamaterials in aeronautics”. In: *Applied Sciences* 8.6 (2018), p. 971.
- [54] T. Elnady et al. “Quenching of acoustic bandgaps by flow noise”. In: *Applied Physics Letters* 94.13 (2009), p. 134104.
- [55] Y. Aurégan, M. Farooqui, and J. Groby. “Low frequency sound attenuation in a flow duct using a thin slow sound material”. In: *The Journal of the Acoustical Society of America* 139.5 (2016), EL149–EL153.
- [56] X. Huang, S. Zhong, and O. Stalnov. “Analysis of scattering from an acoustic cloak in a moving fluid”. In: *The Journal of the Acoustical Society of America* 135.5 (2014), pp. 2571–2580.

- [57] U. Iemma and G. Palma. “Convective correction of metafluid devices based on Taylor transformation”. In: *Journal of Sound and Vibration* 443 (2019), pp. 238–252.
- [58] Y. He, S. Zhong, and X. Huang. “Extensions to the acoustic scattering analysis for cloaks in non-uniform mean flows”. In: *The Journal of the Acoustical Society of America* 146.1 (2019), pp. 41–49.
- [59] Z. Ma, O. Stalnov, and X. Huang. “Design method for an acoustic cloak in flows by topology optimization”. In: *Acta Mechanica Sinica* 35.5 (2019), pp. 964–971.
- [60] W. J. Devenport et al. “The Kevlar-walled anechoic wind tunnel”. In: *Journal of Sound and Vibration* 332.17 (2013), pp. 3971–3991.
- [61] U. Ingard. *Notes on Acoustics*. Infinity Science Press LLC, 2008.
- [62] N. Sugimoto and T. Horioka. “Dispersion characteristics of sound waves in a tunnel with an array of Helmholtz resonators”. In: *The Journal of the Acoustical Society of America* 97.3 (1995), pp. 1446–1459.
- [63] C. Cai and C. M. Mak. “Noise control zone for a periodic ducted Helmholtz resonator system”. In: *The Journal of the Acoustical Society of America* 140.6 (2016), EL471–EL477.
- [64] H. Schlichting. *Boundary layer theory*. 7th. McGraw-Hill, New York, 1979.
- [65] Y. Aurégan, M. Leroux, and V. Pagneux. “Measurement of liner impedance with flow by an inverse method”. In: *10th AIAA/CEAS Aeroacoustics Conference*. 2004, p. 2838.
- [66] S. Dequand et al. “Helmholtz-like resonator self-sustained oscillations, part 1: Acoustical measurements and analytical models”. In: *AIAA journal* 41.3 (2003), pp. 408–415.
- [67] J. Kennedy. Trinity College, Dublin, Personal communication. 2019.

- [68] X. Dai and Y. Aurégan. “Acoustic of a perforated liner with grazing flow: Floquet-Bloch periodical approach versus impedance continuous approach”. In: *The Journal of the Acoustical Society of America* 140.3 (2016), pp. 2047–2055. ISSN: 0001-4966. DOI: [10.1121/1.4962490](https://doi.org/10.1121/1.4962490).
- [69] X. Dai and Y. Aurégan. “Flexural instability and sound amplification of a membrane-cavity configuration in shear flow”. In: *The Journal of the Acoustical Society of America* 142.4 (2017), pp. 1934–1942.
- [70] X. Dai and Y. Aurégan. “A cavity-by-cavity description of the aeroacoustic instability over a liner with a grazing flow”. In: *Journal of Fluid Mechanics* 852 (2018), pp. 126–145.
- [71] F. Langfeldt et al. “Perforated membrane-type acoustic metamaterials”. In: *Physics Letters, Section A: General, Atomic and Solid State Physics* 381.16 (2017), pp. 1457–1462. ISSN: 03759601. DOI: [10.1016/j.physleta.2017.02.036](https://doi.org/10.1016/j.physleta.2017.02.036).
- [72] Y. H. Chiu, L. Cheng, and L. Huang. “Drum-like silencers using magnetic forces in a pressurized cavity”. In: *Journal of Sound and Vibration* 297.3-5 (2006), pp. 895–915. ISSN: 10958568. DOI: [10.1016/j.jsv.2006.05.006](https://doi.org/10.1016/j.jsv.2006.05.006).
- [73] M. Farooqui and Y. Aurégan. “Compact beam liners for low frequency noise”. In: June (2018), pp. 25–29. DOI: [10.2514/6.2018-4101](https://doi.org/10.2514/6.2018-4101).
- [74] F. Li, K. Kishimoto, and Y. Wang. “Vibration control of beams with active constrained layer damping”. In: *Smart Mater. Struct.* 17 (2008). DOI: [10.1088/0964-1726/17/6/065036](https://doi.org/10.1088/0964-1726/17/6/065036).
- [75] Yves Aurégan and Maaz Farooqui. “In-parallel resonators to increase the absorption of subwavelength acoustic absorbers in the mid-frequency range”. In: *Scientific reports* 9.1 (2019), pp. 1–6.

- [76] M. E. D’Elia et al. “Optical Measurements of the Linear Sound-Flow Interaction above a Corrugated Plate”. In: *25th AIAA/CEAS Aeroacoustics Conference*. 2019, p. 2716.
- [77] U. Ingard. “Influence of fluid motion past a plane boundary on sound reflection, absorption, and transmission”. In: *The Journal of the Acoustical Society of America* 31.7 (1959), pp. 1035–1036.
- [78] M.K. Myers. “On the acoustic boundary condition in the presence of flow”. In: *Journal of Sound and Vibration* 71.3 (1980), pp. 429–434.
- [79] Y. Renou and Y. Aurégan. “Failure of the Ingard–Myers boundary condition for a lined duct: An experimental investigation”. In: *The Journal of the Acoustical Society of America* 130.1 (2011), pp. 52–60.